LBL-38341
UC-410

Lawrence Berkeley Laboratory
UNIVERSITY OF CALIFORNIA

Materials Sciences Division

Studies of Thin Films and Surfaces with Optical Harmonic Generation and Electron Spectroscopy

D.E. Wilk
(Ph.D. Thesis)

January 1996

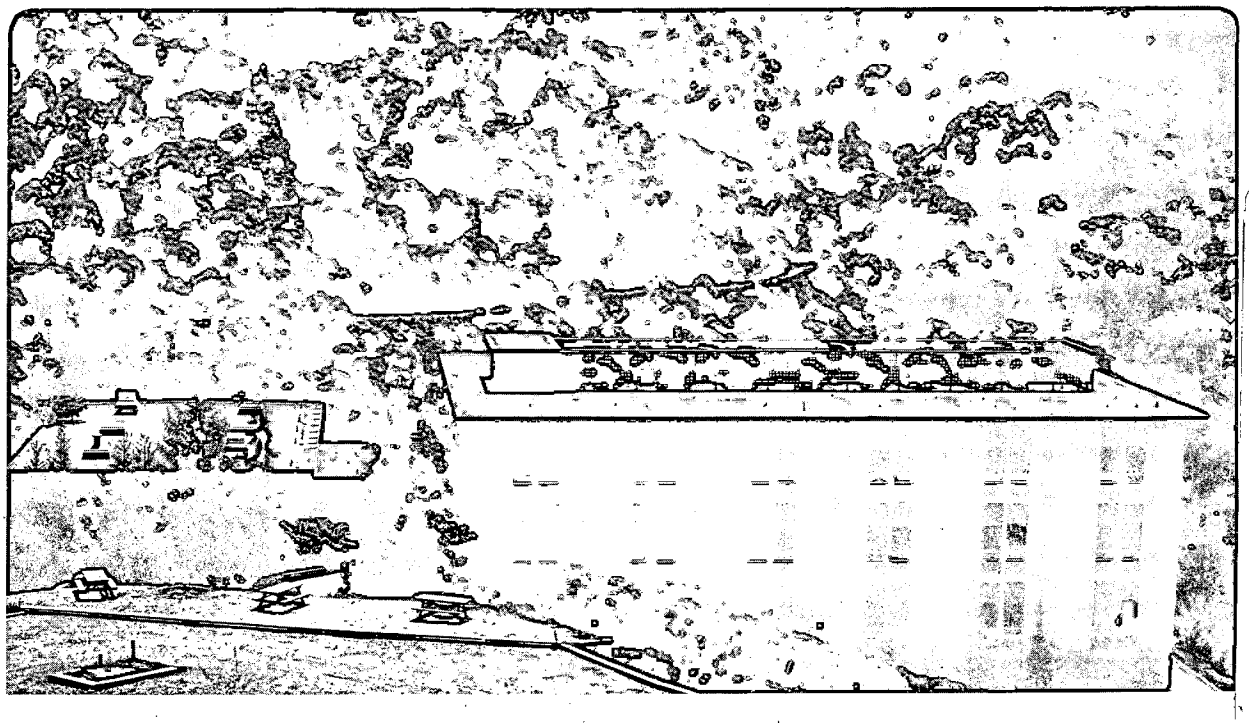

Prepared for the U.S. Department of Energy under Contract Number DE-AC03-76SF00098

DISCLAIMER

LBL-38341
UC-410

Studies of Thin Films and Surfaces with Optical Harmonic Generation and Electron Spectroscopy

DIETER EMRE WILK
Ph.D. Thesis

Department of Physics
University of California

and

Materials Sciences Division
Lawrence Berkeley National Laboratory
University of California
Berkeley, CA 94720

January 1996

This work was supported by the Director, Office of Energy Research, Office of Basic Energy Sciences, Materials Sciences Division, of the U.S. Department of Energy under Contract No. DE-AC03-76SF00098.

Studies of Thin Films and Surfaces with Optical Harmonic Generation and Electron Spectroscopy

by

Dieter Emre Wilk

B. S. (University of California, Los Angeles) 1987

A dissertation submitted in partial satisfaction of the
requirements for the degree of
Doctor of Philosophy
in
Physics
in the
GRADUATE DIVISION
of the

UNIVERSITY OF CALIFORNIA, BERKELEY

Committee in charge:
Professor Y. R. Shen, Chair
Professor Peter Yu
Professor Gabor Somorjai

January 1996

Abstract

Studies of Thin Films and Surfaces with Optical Harmonic Generation and Electron Spectroscopy

by

Dieter Emre Wilk

Doctor of Philosophy in Physics

University of California, Berkeley

Professor Y. R. Shen, Chair

Optical second harmonic generation (SHG) and sum frequency generation (SFG) have complemented the standard Ultra-High Vacuum (UHV) electron spectroscopy for the study of interfaces and thin films. These optical techniques have provided valuable information on systems such as insulating surfaces, which pose a problem for electron spectroscopy. Additionally, because of the longer penetration depth of photons compared to electrons, SHG and SFG are ideal for probing interfaces sandwiched in multilayer structures. In this thesis, SHG and SFG are used to study C_{60} thin solid films and electron spectroscopy is used to study the organic overlayers on Pt(111).

In applying SHG and SFG to thin films, it is important to distinguish the bulk and surface contributions. We present

a complete theoretical description of second-harmonic generation from a thin-film system in terms of surface and bulk contributions as well as local and nonlocal contributions to the optical nonlinearities. In addition, we describe the possible use of tunable SFG to probe and discriminate between Electric Quadrupole(EQ) and Magnetic Dipole(MD) dipole transitions of C_{60}. A simple microscopic model is used to estimate the resonant enhancement of the SF response by the C_{60} EQ and MD transitions.

In situ SHG measurements are performed using 1.064 μm wavelength laser pulses on C_{60} films during film growth under UHV conditions. The results can be well described in terms of only nonlocal contributions to both surface and bulk nonlinear susceptibilities. The microscopic origin of the SHG response is discussed in terms of EQ and ED transitions of C_{60}.

Experiments planned to further study C_{60} films utilizing second-order nonlinear spectroscopy are discussed. First, some background on the temperature-tuned optical parametric oscillator (OPO) is given. Next, a detailed description of the design and setup of the tunable SFG experiments to probe the HOMO-LUMO EQ and MD transitions is presented. We find that these transitions are observable with SFG spectroscopy with a Signal to Background ratio of at least 10.

The adsorption and thermal decomposition of ortho- and para-xylene on Pt(111) is studied using high resolution electron

energy loss spectroscopy (HREELS), low energy electron diffraction (LEED), auger electron spectroscopy(AES), and thermal desorption spectroscopy (TDS). We have observed preferential decomposition of the methyl groups which leads to distinct decomposition pathways for ortho- and para-xylene on Pt(111).

Table of Contents

I. Introduction and Background

A) Second Harmonic and Sum Frequency Generation From Surfaces and Thin Films

In the last 20 years, much progress has been made in the study of surfaces and interfaces. A wide variety of experimental techniques developed has made this possible[1,2]. Massive particles, such as electrons and atoms, have been used to develop very useful tools for probing surfaces and interfaces due to the strong interaction of these particles with surfaces. Information such as chemical composition and structure can be easily obtained using Auger Electron Spectroscopy (AES), Low Energy Electron Spectroscopy (LEED) and High Resolution Electron Energy Loss Spectroscopy (HREELS) [3]. However, techniques involving massive particles are limited to the Ultra-High Vacuum (UHV) environment, allowing only the study of vacuum-solid surfaces. In addition, charging effects preclude the use of electron spectroscopies on insulating surfaces. Surface sensitive optical techniques, such as Infrared Absorption Reflection Spectroscopy(IRAS) and Second Harmonic Generation (SHG) can probe any interface accessible by light. This opens up the possibility of studying liquid-gas [4], liquid-solid[5], and liquid-liquid interfaces[6]

interfaces. Furthermore, the use of pulsed lasers allows one to do time resolved experiments.

Optical Second Harmonic and Sum Frequency Generation have been developed into especially powerful tools for probing surfaces and interfaces[7]. This is due to their submonolayer sensitivity and surface sensitivity when the bulk medium is centrosymmetric, since the second order nonlinear processes are forbidden in a bulk with inversion symmetry. Second Harmonic Generation has been used to probe surface symmetry changes due to surface reconstruction[8], orientation of liquid crystal molecules on polyimide-coated substrates[9,10], the adsorption kinetics of gas molecules on solid surfaces[11], and many others [Review article references]. Sum Frequency Generation has been used to obtain the orientation and conformation of long chain molecules on substrates[9], the structure of surface water layers at various water interfaces[12], the identification of reaction intermediates of hydrocarbons on Pt(111)[13], and others.

More recently, Second Harmonic Generation has also been used to study optical properties of thin films[14-16], which have become increasingly important in the microelectronics industry. Information on semiconductor-insulator interface states[17] and diffusion of Cu into polyimide thin films, for example, can be deduced from such studies[18]. Because of reflections from SHG at interfaces that leads to

interference in the signal, SHG from thin films appears more complicated in general. However, the in-situ monitoring capabilities of SHG during film growth can separate the nonlinear responses of the two interfaces and the bulk[19]. In addition, elegant methods for analyzing SHG and THG from multilayers have been developed[20]. These results show that SHG and SFG can be useful tools for analyzing multilayer thin film structures.

B) Nonlinear Optical Properties of C_{60}

Since the discovery of a method for producing C_{60} in macroscopic quantities[21], intense investigation has revealed a number of its fascinating chemical and physical properties. For example, C_{60} films doped with alkali metal exhibit superconductivity, with T_C as high as 30K[22]. Strong optical non-linearities resulting from delocalized π electrons can be expected for C_{60}. Measurements of second [23-26] and third-order [23,26-32] nonlinearities of C_{60} in films and in solution that are comparable to the values found in conjugated hydrocarbons have actually been reported. Furthermore, researchers have also found that C_{60} behaves as a radical sponge such that a wide variety of chemical constituents can be added to the outside or inside of the cage, offering exciting possibilities for fabricating novel materials. Second-order nonlinearities of C_{60} are forbidden by symmetry under the electric dipole approximation. The extended electron delocalization on C_{60}

however suggests that asymmetrization of the molecule with addition of appropriate chemical constituents on the cage via conjugate bonds could lead to a large second-order molecular polarizability. In this respect, it is important to know how the unmodified C_{60} behaves as a second-order nonlinear optical medium. Because of electron delocalization and the fair size of the cage, one can still expect a rather strong second-order nonlinearity for C_{60} from the electric quadrupole and magnetic dipole contributions. In this manuscript, we will study the theory and experiments involving Second-Harmonic and Sum-Frequency Generation on solid C_{60} thin films.

C) Electron Spectroscopy on Transition Metal Surfaces

While the use of lasers for nonlinear optical experiments provides some advantages over the older electron spectroscopies, there are still advantages in using electron spectroscopy. First, electron gun operation and maintenance is much simpler than a laser[2]. Also, the electron beam is more easily tunable over a wider range of energies than most lasers, even though the energy resolution is inherently poorer. In this sense, these techniques complement the optical techniques and can lead to more complete information on composition and structure of surfaces and interfaces. We have used electron spectroscopic techniques under Ultra-High Vacuum (UHV) techniques to probe the composition and structure of hydrocarbons on transition metal surfaces.

Understanding the adsorption of hydrocarbons on transition metal surfaces and any decomposition they may undergo as a function of temperature is an important problem in surface science. Determining the adsorbate structure and thermal decomposition fragments of a hydrocarbon on a metal surface can give insight into chemisorption and catalytic processes of organic molecules and can lead to a better understanding of the molecule-surface interaction, which also provides the microscopic basis for adhesion and lubrication. Therefore, we study the adsorption and thermal decomposition of di-substituted benzene on Pt(111).

Scope

In Chapters 2-5, we investigate the nonlinear optical properties from solid C_{60} films. We use SHG and SFG to investigate the low energy ED forbidden electronic excitations of the C_{60} molecule. In chapter 6 we apply Thermal Desorption Spectroscopy (TDS) and High Resolution Electron Energy Loss Spectroscopy (HREELS) to study the adsorption and thermal decomposition of both Ortho- and Para- Xylene on the Pt(111) surface.

References

1. M. Prutton, Surface Physics, Oxford University Press, Oxford, 1983.

2. G. Somorjai, Chemistry in Two Dimensions: Surfaces, University Press, Ithaca, New York, 1981.

3. A. Zangwill, Physics at Surfaces, Cambridge University Press, Cambridge, 1988.

4. T. Rasing, Y. R. Shen, M. W. Kim and S. Grubb, Phys. Rev. Lett. **55**, 2903 (1985).

5. C. K. Chen, Phys. Rev. Lett. **46**, 1010(1981).

6. T. Rasing, J. Huang, A. Lewis and Y. R. Shen, Phys. Rev. Lett. A **40**, 1684(1989).

7. Y. R. Shen, Ann. Rev. Mater. Sci, **16**, 69(1986).

8. G. Richmond. Surf. Sci. (1991).

9. M. B. Feller, W. Chen, Y. R. Shen, Phys. Rev. A **43**, 6778(1991).

10. W. Chen, M. B. Feller, Y. R. Shen, Phys. Rev. Lett. **63** 2665(1989).

11. X. D. Zhu, PhD Thesis, University of California, Berkeley, 1990.

12. V. Vogel, C. S. Mullin, M.W. Kim and Y. R. Shen, J. Chem. Phys. **95**, vol.6, 4620(1991).

13. P. Cremer, Colin Stanners, J. W. Niemantsverdriet, Y. R. Shen, and G. A. Somorjai, in press.

14. N. Bloembergen and P.S. Pershan, Phys. Rev. **128**, 606 (1962).

15. B. U. Felderhof and G. Marowsky, Applied Physics B **44**, 11 (1987).

16. M. S. Yegeneh, J. Qi, P. Culver, and A. G. Yodh, Physical Review B **46**, 1603 (1992).

17. T. Stehlin, M. Feller, P. Guyot-Sionnest, Y. R. Shen, Opt. Lett. **13**, 389(1988).

18. J. Zhang, Y. R. Shen, D. S.Soane, S. C. Freilich, App. Phys. Lett., **59**, 11, 1305(1991).

19. D. Wilk, D. Johannsmann, C. Stanners, Y. R. Shen, Phys. Rev. B, **51**, 13, 10057(1995).

20. D. S. Bethune, J. Opt. Soc. America b **6**, 910 (1989).

21. W. Kraetschmer, L.D. Lamb, K. Fostiropoulos, and D.R. Huffman, Nature **347**, 354 (1990).

22. M. J. Rosseindky, et. al. Phys. Rev. Lett. **66**, 2830 (1991).

K. Holczer, et. al. Science **252**, 1154 (1991).

23. H. Hoshi, N. Nakamura, Y. Maruyama, T.Nakagawa, S.Suzuki, H. Shiromaru, Y. Achiba, Jpn. J. Appl. Physics, Part 2 - Letters **30**, : L1397 (1991).

24. X. K. Wang, T. G. Zhang, W. P. Lin, S. Z. Liu, G. K. Wong, M. M. Kappes, R. P. H. Chang, and J. B. Ketterson, Appl. Phys. Lett. **60**, (7), 810 (1992).

25. B. Koopmans, A. M. Janner, H. T. Jonkman, G. A. Sawatzky, and F. van der Woude, Phys. Rev. Lett. **71** ,3569 (1993).

26. F. Kajzar, C. Taliani, R. Zamboni, S. Rossine, R. Danieli, Synthetic Metals **54**, 21 (1993).

27. W. J. Blau, H. J. Byrne, D. J. Cardin, Phys. Rev. Lett., **67**, 1423 (1991).

28. Z. H. Kafafi, J. R. Lindle, R. G. S. Pong, F. J. Bartoli, L. J. Ling, J. Milliken, Chem. Phys. Lett., **188**, 492 (1992).

29. J. S. Meth, H. Vanherzeele, Y. Wang, Chem. Phys. Lett. **197**, 26 (1992).

30. M. J. Rosker, H. d. Marcy, T. Y. Chang, J. T. Khoury, K. Hansen, R. L. Whetten, Chem. Phys. Lett. **196**, 427 (1992).

31. F. Henari, J. Callaghan, H. Stiel, W. Blau, D. J. Cardin, Chem. Phys. Lett. **199**, 144 (1992).

32. G. B. Talaptra, N. Manickam, M. Samoc, M. E. Orczyk, S. P. Karna, P. N. Prasad, J. Phys. Chem. **96**, 5266 (1992).

II. Bulk and Interface Second Harmonic Generation

Introduction

Since the first experimental realization of optical second harmonic and sum frequency generation, the relative role of bulk and surface contributions has been considered by many authors[1-6]. The second harmonic or sum frequency signal from an interface can be split into two contributions, one coming from the surface states and the other from the bulk. If the bulk is not centrosymmetric then the bulk response will dominate in most cases. However, early studies show that if the bulk medium is centrosymmetric then the bulk electric quadrupole and magnetic dipole response can still be significant due to the sharp discontinuity of the electric field across the interface[2]. More recent studies have shown, however, that there are many cases where the surface layer of molecules can dominate the SH signal[6]. In addition the surface states on semiconductors and some metals are easily observed with second harmonic generation[7,8]. The problem of bulk vs. surface contributions was discussed in detail by P. G. Sionnest [4] and then refined by Sipe[5]. Out of these investigations arose two major results. The surface contribution to SHG from a centrosymmetric medium can be split into two parts,

one due to the discontinuity in the linear index of refraction across the interface, and a structural discontinuity in the bulk electric quadrupole susceptibility across the interface[1]. In addition, there is no method to achieve complete separation of bulk and surface response without a microscopic model[4].

The study of Second-Harmonic generation from thin films are more complicated due to contributions from two non equivalent interfaces as well as the bulk. In general one must also take into account the multiple reflections at both boundaries of the film and therefore interference effects at both the fundamental and SH frequencies need to be considered. In the following section we outline the method for determining the SH response from a thin film. We use the notation of Y. R. Shen [1] rather than that of Sipe [5] to describe the overall measured SH intensity from a homogeneous centrosymmetric thin film.

Second-harmonic Generation from a Homogeneous Thin Film

A) Second harmonic generation from a thin film

We consider the case of an isotropic film of thickness d deposited on a substrate whose optical nonlinearity is

negligible. As described in Fig. 1, the film is sandwiched between vacuum at z >d and the substrate at z < 0. The laser beam is incident from the substrate side with an incidence angle θ_ω and the corresponding field at a position z inside the film is

$$\vec{E}(\omega,z) = \vec{L}(\omega,z) \bullet \vec{E}_I(\omega) \cdot e^{i(k_x(\omega)x - \omega t)} \qquad [1]$$

where $\vec{L}(\omega,z)$ is a diagonal tensor defined by [9]

$$L_{xx}(\omega,z) = t_1^p \left[\exp(ik_{fz}z) - r_{fv}^p \exp(ik_{fz}(2d-z))\right] \frac{\cos(\theta_f)}{\cos(\theta_\omega)}$$

$$L_{yy}(\omega,z) = t_1^s \left[\exp(ik_{fz}z) + r_{fv}^s \exp(ik_{fz}(2d-z))\right]$$

$$L_{zz}(\omega,z) = t_1^p \left[\exp(ik_{fz}z) + r_{fv}^p \exp(ik_{fz}(2d-z))\right] \frac{\varepsilon_q^{1/2}}{\varepsilon_f^{1/2}}$$

$$\text{with} \quad t_1^h = \frac{t_{qf}^h}{\left[1 - r_{fq}^h r_{fv}^h \exp(i2k_{fz}d)\right]} \ , \qquad [2]$$

Here, t_{mn}^h and r_{mn}^h refer to field transmission and reflection coefficients of the h-polarized beam at the interface between media m and n; the sub indices q, f, and v refer to the fused quartz substrate, the film, and the vacuum,

respectively. Physically, $\tilde{L}$ behaves like a macroscopic local field factor relating the field inside the film, $\bar{E}(\omega,z)$, and the incoming field $\bar{E}_I(\omega)e^{i(k_x(\omega)x - \omega t)}$. The field $\bar{E}(\omega,z)$ can induce a nonlinear polarization in the film at z described by:

$$\bar{P}^{(2)}(2\omega,z) = \tilde{\chi}^{(2)}:\bar{E}(\omega,z)\,\bar{E}(\omega,z) \qquad [3]$$

The nonlinear susceptibility $\tilde{\chi}^{(2)}$, in Eq. [3] is in general nonlocal as we shall discuss more clearly later.

We first focus on the radiation generated by $\bar{P}^{(2)}(2\omega,z)$. It is known that the field of radiation from a polarization sheet $\bar{p}dz'\exp(i\bar{k}\cdot\bar{r}' - i\Omega t)$ immersed in an infinite index-matched medium of dielectric constant ε_q is given by[6]

$$E_{po}(\Omega,\bar{r};\bar{r}') = \frac{i2\pi k_q(\Omega)}{\varepsilon_q(\Omega)k_{qz}(\Omega)}\left(k_{qz}p_x + k_x p_z\right)dz'\exp[i\bar{k}\cdot(\bar{r} - \bar{r}') - i\Omega t]$$

$$E_{so}(\Omega,\bar{r};\bar{r}') = \frac{i2\pi k_q^2(\Omega)}{\varepsilon_q(\Omega)k_{qz}(\Omega)}p_y dz'\exp[i\bar{k}\cdot(\bar{r} - \bar{r}') - i\Omega t], \qquad [4]$$

where the sub indices p and s refer to the p and s polarizations, respectively. If instead the polarization sheet is now embedded in the film described in Fig. 1, then it can be easily shown that the radiated field into the substrate is

$$\vec{E}_q(\Omega,\vec{r}\,;\vec{r}\,') = \vec{E}_o(\Omega,\vec{r}\,;\vec{r}\,')\cdot\vec{L}(\Omega,z') \qquad [5]$$

with $\vec{L}$ expressed in Eq. (2), and the field radiated into the vacuum is

$$\vec{E}_v(\Omega,\vec{r}\,;\vec{r}\,') = \vec{E}_o(\Omega,\vec{r}\,;\vec{r}\,')\cdot\vec{L}'(\Omega,z') \qquad (6)$$

where $\vec{L}'$ is the local field factor relating the field in the vacuum to the field in the film, and can be obtained from the expression of $\vec{L}$ in Eq. (2) by interchanging the sub indices q and v and replacing the terms $\exp[ik_{fz}z]$ and $\exp[ik_{fz}(2d-z)]$ in the numerators by $\exp[ik_{fz}(d - z)]$ and $\exp[ik_{fz}(d + z)]$, respectively.

The above discussion allows us to write down explicitly the total SH field generated by $\vec{P}^{(2)}(2\omega,z)$ in the bulk of the film:

$$E_p^B(2\omega) = i\left(\frac{4\pi\omega}{\varepsilon_q^{1/2}(2\omega)c}\right)\int_0^d dz'\left\{\begin{bmatrix} L_{xx}(2\omega,z')\chi^{(2)}_{xjk} + \dfrac{k_x(2\omega)}{k_{qz}(2\omega)}L_{zz}(2\omega,z')\chi^{(2)}_{zjk} \end{bmatrix}\right\} E_{Ij}(\omega)E_{Ik}(\omega)$$
$$L_{jj}(\omega,z')L_{kk}(\omega,z')$$

[7]

$$E_s^B(2\omega) = i\left(\frac{2\pi k_q^2(2\omega)}{k_{qz}(2\omega)\varepsilon_q(2\omega)}\right)\int_0^d dz'\left[L_{yy}(2\omega,z')\chi^{(2)}_{yjk}L_{jj}(\omega,z')L_{kk}(\omega,z')\right]E_{Ij}(\omega)E_{Ik}(\omega)$$

(7)

for the SH radiation field in the substrate. For the SH field in the vacuum, we simply replace $\tilde{L}$ by $\tilde{L}'$ and the sub index q by v. However, the interfaces of quartz/film and film/vacuum may also contribute to SHG. Let the surface nonlinear polarizations of the two interfaces be

$$\bar{P}(2\omega, q/f) = \tilde{\chi}_s^{(2)}(q/f):\left[\tilde{L}(\omega,z=0)\cdot\bar{E}_I(\omega)\right]\left[\tilde{L}(\omega,z=0)\cdot\bar{E}_I(\omega)\right]$$

$$\bar{P}(2\omega, f/v) = \tilde{\chi}_s^{(2)}(f/v):\left[\tilde{L}(\omega,z=d)\cdot\bar{E}_I(\omega)\right]\left[\tilde{L}(\omega,z=d)\cdot\bar{E}_I(\omega)\right]$$

(8)

Note that here we have chosen the convention in which the interface is defined to be just inside the film. To switch to the more common convention (6), in which the interface is placed outside the film, one should replace $\chi^{(2)}{}_{s,zzz}$,

$\chi^{(2)}_{s,,zyy}$, and $\chi^{(2)}_{s,yzy}$, with $\chi^{(2)}_{s,zzz}(\varepsilon_n(2\omega)\varepsilon_n(\omega)^2)/(\varepsilon_f(2\omega)\varepsilon_f(\omega)^2)$, $\chi^{(2)}_{s,,zyy}\varepsilon_n(2\omega)/\varepsilon_f(2\omega)$, and $\chi^{(2)}_{s,yzy}\varepsilon_n(\omega)/\varepsilon_f(\omega)$, respectively, where the f (n) sub index refers to the film (vacuum or quartz) medium. The SH fields generated by them can again be written down immediately. The expressions are essentially the same as those in Eqn. (7) with $\tilde{L}(z)$ taken at z=0 and z=d and $\int_0^d \vec{\chi}^{(2)}dz'$ replaced by $\vec{\chi}^{(2)}_s$.

The total SH field generated by the nonlinear film is then given by

$$\tilde{E}(2\omega) = \tilde{E}^B(2\omega) + \tilde{E}(2\omega, q/f) + \tilde{E}(2\omega, f/v) \qquad (9)$$

With some manipulation, the total SH output into the substrate in terms of photons per pulse can be expressed in the simple form [6]

$$S(2\omega) = \left[\frac{32\pi^3\omega}{\hbar c^3 \varepsilon_q^{1/2}(2\omega)\varepsilon_q(\omega)}\right] \sec^2\theta_{2\omega} \left|\chi^{(2)}_{eff}\right|^2 I^2(\omega) AT \qquad (10)$$

where

$$\chi^{(2)}_{eff} = \hat{e}(2\omega)\cdot\tilde{L}(2\omega, z=0) : \vec{\chi}^{(2)}_s(q/f) : \tilde{L}(\omega, z=0)\cdot\hat{e}(\omega)\tilde{L}(\omega, z=0)\cdot\hat{e}(\omega)$$

$$+ \hat{e}(2\omega)\cdot\tilde{L}(2\omega, z=d) : \vec{\chi}^{(2)}_s(f/v) : \tilde{L}(\omega, z=d)\cdot\hat{e}(\omega)\tilde{L}(\omega, z=d)\cdot\hat{e}(\omega)$$

$$+\int_0^d \hat{e}(2\omega)\cdot\vec{L}(2\omega,z'):\vec{\chi}_B^{(2)}:\vec{L}(\omega,z')\cdot\hat{e}(\omega)\vec{L}(\omega,z')\cdot\hat{e}(\omega)dz' \quad , \qquad (11)$$

$\theta_{2\omega}$ is the exit angle, A the beam cross-section, T the pulse width, and $\hat{e}(\Omega)$ the unit vector of the field at Ω. In practice, the substrate has a finite thickness. The incoming fundamental beam from the substrate side will suffer a reflection loss at the vacuum/substrate interface, and so will the SH output reflected out of the substrate side. These losses must also be taken into account in calculating the SH signal .

Because of the phase factors in $\vec{L}$, the bulk term in $\chi_{eff}^{(2)}$ in Eq. (11) is expected to exhibit a composite interference pattern as the film thickness d varies. Furthermore, the two surface terms and the bulk term in $\chi_{eff}^{(2)}$ can have relative phase differences and their interference also changes with d. Fitting the measurement of $S(2\omega)$ versus d with Eq. (10) may allow us to determine separately the bulk and surface susceptibilities to some extent as we shall see for the case of isotropic films below.

B) Nonlinear Optical Susceptibilities of a Centrosymmetric Homogeneous Thin Film

We consider here an isotropic film. At a surface of such a film, symmetry requires that the only non vanishing elements

of $\tilde{\chi}_s^{(2)}$ are $\chi^{(2)}{}_{s,zzz}$, $\chi^{(2)}{}_{s,zxx} = \chi^{(2)}{}_{s,zyy}$, and $\chi^{(2)}{}_{s,xzx} = \chi^{(2)}{}_{s,yzy}$. Thus there are altogether six non vanishing independent elements describing $\tilde{\chi}_s^{(2)}$ for the two interfaces of the film. For the bulk, the effective nonlinear polarization can generally be written as [see, e. g. Ref. 10]

$$\bar{P}^{(2)}(2\omega) = \bar{P}_d^{(2)}(2\omega) - \nabla\cdot\tilde{Q}^{(2)}(2\omega) + \frac{c}{i2\omega}\nabla\times\bar{M}^{(2)}(2\omega) + \cdots \qquad (12)$$

where $\bar{P}_d^{(2)}, \tilde{Q}^{(2)}$, and $\bar{M}^{(2)}$ denote second-order electric dipole polarization, electric quadrupole polarization, and dipole magnetization, respectively. To the order linear in spatial gradient in $\bar{P}^{(2)}(2\omega)$, we have

$$\begin{aligned} \bar{P}_d^{(2)} &= \tilde{\chi}^D : \bar{E}(\omega)\bar{E}(\omega) + \tilde{\chi}^P : \bar{E}(\omega)\nabla\bar{E}(\omega) \\ \tilde{Q}^{(2)} &= \tilde{\chi}^Q : \bar{E}(\omega)\bar{E}(\omega) \\ \bar{M}^{(2)} &= \tilde{\chi}^M : \bar{E}(\omega)\bar{E}(\omega) \end{aligned} \qquad (13)$$

While $\tilde{\chi}^D$ describes a local response, $\tilde{\chi}^P$, $\tilde{\chi}^Q$, and $\tilde{\chi}^M$ are nonlocal. In an isotropic medium, symmetry arguments show that $\tilde{\chi}^D = 0$ and the non vanishing elements of $\tilde{\chi}^P$ are $\chi^P{}_{iiii} = \chi_1{}^P$, $\chi^P{}_{iijj} = \chi_2{}^P$, $\chi^P{}_{ijij} = \chi_3{}^P$, and $\chi^P{}_{ijji} = \chi_4{}^P$ with $\chi_1{}^P = \chi_2{}^P + \chi_3{}^P + \chi_4{}^P$. These symmetry relations for $\tilde{\chi}^Q$ are also true, but we have, in addition, $\chi_3{}^Q = \chi_4{}^Q$. Also, if

there is inversion symmetry in both space and time, then $\tilde{\chi}^M$ is proportional to the antisymmetric tensor of the third rank and therefore $\tilde{M}(2\omega)=0$ [8]. Using these relations and substituting Eq. (13) into Eq. (12), we can find $\tilde{P}^{(2)}(2\omega)$ in the form [1]

$$\tilde{P}_i^{(2)}(2\omega) = \delta'\left[\tilde{E}(\omega)\cdot\nabla\right]E_i(\omega) + \beta E_i(\omega)\left[\nabla\cdot\tilde{E}(\omega)\right] + \gamma\nabla_i\left[\tilde{E}(\omega)\cdot\tilde{E}(\omega)\right] - \nabla_j\chi^Q_{ijkl}E_k(\omega)E_l(\omega) \tag{14}$$

with $\delta' = (\delta-\beta-2\gamma) = 2\left(\chi_4^P - \chi_3^Q\right)$

$$\delta = \chi_1^P - \chi_1^Q$$

$$\beta = 2\left(\chi_2^P - \chi_3^Q\right)$$

$$\gamma = \chi_3^P - \chi_2^Q \tag{15}$$

Since $\nabla\cdot\tilde{E} = 0$ in a homogeneous, isotropic dielectric, the β term in $P_i^{(2)}(2\omega)$ never contributes to SHG in an isotropic bulk. The $\nabla_j\chi^Q_{ijkl}$ term also vanishes in a homogeneous bulk. the medium. Finally, it has been shown repeatedly that the bulk contribution to SHG from the γ term is indistinguishable from the surface contribution due to the $\chi^{(2)}{}_{s,zzz}$ and $\chi^{(2)}{}_{s,zyy}$ terms [5]. In our case, it can be properly taken into account if we simply replace $\chi^{(2)}{}_{s,zzz}(q/f)$, $\chi^{(2)}{}_{s,zyy}(q/f)$, $\chi^{(2)}{}_{s,zzz}(f/v)$, and $\chi^{(2)}{}_{s,zyy}(f/v)$ by

$\chi^{(2)}_{s,zzz}(q/f) - \gamma$, $\chi^{(2)}_{s,zyy}(q/f) - \gamma$, $\chi^{(2)}_{s,zzz}(f/v) + \gamma$, $\chi^{(2)}_{s,zyy}(f/v) + \gamma$, respectively. In this respect the δ' term in Eq. (15) is the only bulk term that contributes independently to SHG. Therefore, to characterize SHG from an isotropic film, we have altogether 7 independent susceptibility elements;

$\chi^{(2)}_{s,zzz}(f/v) + \gamma$, $\chi^{(2)}_{s,zzz}(q/f) - \gamma$,

$\chi^{(2)}_{s,zyy}(f/v) + \gamma$, $\chi^{(2)}_{s,zyy}(q/f) - \gamma$,

$\chi^{(2)}_{s,yzy}(f/v)$, $\chi^{(2)}_{s,yzy}(q/f)$,

and δ'.

We now consider how in some cases, surface nonlinearities $\tilde{\chi}^S$ can be connected with the bulk nonlinearities $\tilde{\chi}^P$ and $\tilde{\chi}^Q$. By definition, the surface nonlinear polarization $\tilde{P}^{(2)}_s(2\omega)$ is related to the spatially varying bulk nonlinear polarization $\tilde{P}^{(2)}(z,2\omega)$ across the interface by [1]

$$P^{(2)}_{s,i} = \int_I s_i(z,2\omega) P^{(2)}_i(z,2\omega)\, dz, \qquad (16)$$

where the integration is across the interface I, and $\bar{s}(z,\Omega)$ is defined as

$$s_i(z,\Omega) = \begin{cases} 1 & i = x,y \\ \dfrac{E_i(z,\Omega)\varepsilon_f(\Omega)}{D_i(z,\Omega)} & i = z \end{cases} \qquad (17)$$

We expect that $\vec{P}^{(2)}(z,2\omega)$ can still have the expression described in Eqs. (12) and (13), but with $\vec{\chi}^D$, $\vec{\chi}^P$, and $\vec{\chi}^Q$ being spatially dependent. With

$$\vec{P}_s^{(2)}(2\omega) = \vec{\chi}^s : \vec{E}(\omega)\vec{E}(\omega) \qquad (18)$$

we can then formally express χ^s_{ijk} as[1]

$$\chi^s_{ijk} = \int s_i(z,2\omega)\cdot\left\{\chi^P_{ijzk}(z)\cdot s_j(z,\omega)\cdot\nabla_z s_k(z,\omega) - \nabla_z\left[\chi^Q_{izjk}(z)\cdot s_j(z,\omega)\cdot s_k(z,\omega)\right]\right\}dz \qquad (19)$$

In order to perform the integral in Eq. (19), we must know the functional forms of $s_Z(z.\omega)$, $s_Z(z,2\omega)$, $\chi^D(z)$, $\chi^P(z)$, and $\chi^Q(z)$. We assume here the simple case of $\chi^D(z) = 0$. This is expected to be a good approximation for C_{60} films. Knowing that C_{60} molecules are weakly interacting, we also assume that both linear and nonlinear responses of a C_{60} film are directly proportional to the local density of C_{60} molecules. Let $\rho(z)$ be the normalized molecular density varying with z across an interface (ρ=1 inside the film and

ρ=0 outside the film). Neglecting the microscopic local field effects across the interface, we then have

$$\chi^{P}(z) = \chi^{P} \cdot \rho(z)$$

$$\chi^{Q}(z) = \chi^{Q} \cdot \rho(z)$$

$$s_z(z,\Omega) = \frac{\varepsilon_f(\Omega)}{\varepsilon_n(\Omega) + (\varepsilon_f(\Omega) - \varepsilon_n(\Omega))\rho(z)} \qquad \Omega = \omega,\ 2\omega$$

(20)

where ε_f and ε_n are dielectric constants of the bulk C_{60} film and medium n, respectively. Neglecting the dispersion in $s_z(z,\Omega)$, we can explicitly evaluate the integral of Eq. (19) and find, for an isotropic C_{60} film sandwiched between a fused quartz substrate and vacuum,

$$\chi_{s,zzz}(q/f) - \gamma = r_1(q/f)\,(\chi_1^{P} + \chi_1^{Q}) - \chi_1^{Q} - \gamma$$

$$\chi_{s,zzz}(f/v) + \gamma = r_1(f/v)\,(\chi_1^{P} + \chi_1^{Q}) + \chi_1^{Q} + \gamma$$

$$\chi_{s,zyy}(q/f) - \gamma = r_2(q/f)\,\chi_2^{Q} - \chi_2^{Q} - \gamma$$

$$\chi_{s,zyy}(f/v) + \gamma = r_2(f/v)\,\chi_2^{Q} + \chi_2^{Q} + \gamma$$

$$\chi_{s,yzy}(q/f) = r_2(q/f)\,\chi_2^{P} - \chi_3^{Q}$$

$$\chi_{s,yzy}(f/v) = r_2(f/v)\,\chi_2^{P} + \chi_3^{Q}$$

$$\delta' = 2\,(\chi_4^{P} - \chi_3^{Q}), \qquad (21)$$

$$\gamma = \chi_3^{P} - \chi_2^{Q}$$

where

$$r_1(q/f) = \frac{\varepsilon_f^3(\omega)}{\varepsilon_f(\omega) - \varepsilon_q(\omega)}\left[\frac{1}{2}\left(\frac{1}{\varepsilon_f^2(\omega)} - \frac{1}{\varepsilon_q^2(\omega)}\right) - \frac{\varepsilon_q(\omega)}{3}\left(\frac{1}{\varepsilon_f^3(\omega)} - \frac{1}{\varepsilon_q^3(\omega)}\right)\right]$$

$$r_2(q/f) = \frac{\varepsilon_f(\omega)}{\varepsilon_f(\omega) - \varepsilon_q(\omega)}\left[\ln\left(\frac{\varepsilon_q(\omega)}{\varepsilon_f(\omega)}\right) + 1 - \frac{\varepsilon_q(\omega)}{\varepsilon_f(\omega)}\right].$$

The corresponding factors $r_1(f/v)$, $r_2(f/v)$ for the film-vacuum interface are obtained by replacing $\varepsilon_q(\omega)$ with $\varepsilon_f(\omega)$ and $\varepsilon_f(\omega)$ with $\varepsilon_v(\omega)$ in the above expressions. We have also included the inseparable bulk term γ and separable bulk term δ' in Eq. 21 for completeness. Note that the effective surface susceptibilities are independent of the density profile and are related to the five bulk susceptibilities through the bulk linear dielectric constants of the media on both sides of the interface. The number of independent bulk susceptibilities can be further reduced by symmetry arguments if the SH signal is dominated by electric quadrupole (EQ) or magnetic dipole (MD) transitions. If the SH signal is dominated by EQ transitions at the SH frequency 2ω, then $\tilde{\chi}^P << \tilde{\chi}^Q$. In this case, the SH response is

adequately described by only χ_2^Q and χ_3^Q. However, if EQ transitions at the fundamental frequency ω dominate, then the additional relation $\chi_3^P = \chi_4^P$ holds. Also, $\tilde{\chi}^Q << \tilde{\chi}^P$ and only χ_2^P and χ_3^P contribute to the SH signal. If the SH signal is dominated by MD transitions at ω, then we have the relations $\chi_3^P = -\chi_4^P$ and $\chi_2^P = 0$. Additionally, $\tilde{\chi}^Q << \tilde{\chi}^P$ and therefore the SH process can be described by only χ_3^P. In this last case, the surface susceptibilities are zero, as seen from Eq. 21. Resonant enhancement of the SH signal by a MD transition at 2ω is not possible because $\tilde{M}(2\omega)=0$. In the general case, the set of 6 surface and 1 bulk nonlinear susceptibilities reduce to a set of five bulk susceptibilities, χ_2^Q, χ_3^Q, χ_2^P, χ_3^P, and χ_4^P, which describe the nonlinear optical response of a C_{60} film.

Conclusion

We have shown explicitly that the bulk electric quadrupole and magnetic dipole and surface contributions to SHG from a thin film system can be expressed in terms of an "effective" surface susceptibility including the effect of the input and output macroscopic local field factors, which reflect the changes of the input and output fields due to multiple reflections at the two interfaces of the thin film. It should be noted that in general the bulk and surface contributions are inseparable. However, for certain systems, there is sound physical reasoning for neglecting

bulk or surface contributions. Also, if one makes assumptions about the microscopic responses of the system, one may achieve separation of surface and bulk contributions, as has been shown in the previous paragraph. In the case where we assume that the interaction with the environment is weak, we can express the surface susceptibilities in terms of the bulk electric quadrupole and magnetic dipole susceptibilities.

References

1. P. Guyot-Sionnest, and Y.R. Shen, Phys. Rev. B **38**, 7985 (1988)

2. N. Bloembergen and P.S. Pershan, Phys. Rev. **128**, 606 (1962).

3. M. S. Yegeneh, J. Qi, P. Culver, and A. G. Yodh, Physical Review B **46**, 1603 (1992).

4. B. Koopmans, A. Anema, H.T. Jonkman, G.A. Sawatzky, and F. van der Woude, Phys. Rev. B **48**, 2759 (1993).

5. J. Sipe, V. Mizrahi, G. Stegeman, Phys. Rev. B **35**, 9091 (1987).

6. Y. R. Shen, Annu. Rev. Phys. Chem. **40**, 327 (1989).

7. H. W. K. Tom, and G. D. Aumiller, Phys. Rev. B **33**, 8818 (1986).

8. T. F. Heinz, M. M. T. Loy, and W. A. Thompson, Phys. Rev. Lett **54** 63(1985).

9. D. E. Wilk, D. Johannsmann, C. Stanners, and Y. R. Shen, Phys. Rev. B, Vol. 51, No. 15, 10057(1995).

10. Pershan, P. S., Phys. Rev. **130**, 919 (1963).

Figure Captions

Fig. (1)

Schematic of SHG from a C_{60} film. $\hat{e}$ and $\bar{k}$ denote polarization and wave vector of a light wave.

Tables

Table 1

Nonlinear Susceptibilities Probed for Various Polarization Combinations from a Thin Film

Nonlinear Susceptibility	s_{in} / p_{out}	$mixed_{in}$ / s_{out}	p_{in} / p_{out}	$mixed_{in}$ / p_{out}
$\chi_{s,zyy}(q/f)-\gamma$ $\chi_{s,zyy}(f/v)+\gamma$	•		•	•
$\chi_{s,zzz}(q/f)-\gamma$ $\chi_{s,zzz}(f/v)+\gamma$			•	•
$\chi_{s,yzy}(q/f)$ $\chi_{s,yzy}(f/v)$		•	•	•
δ'		•	•	•

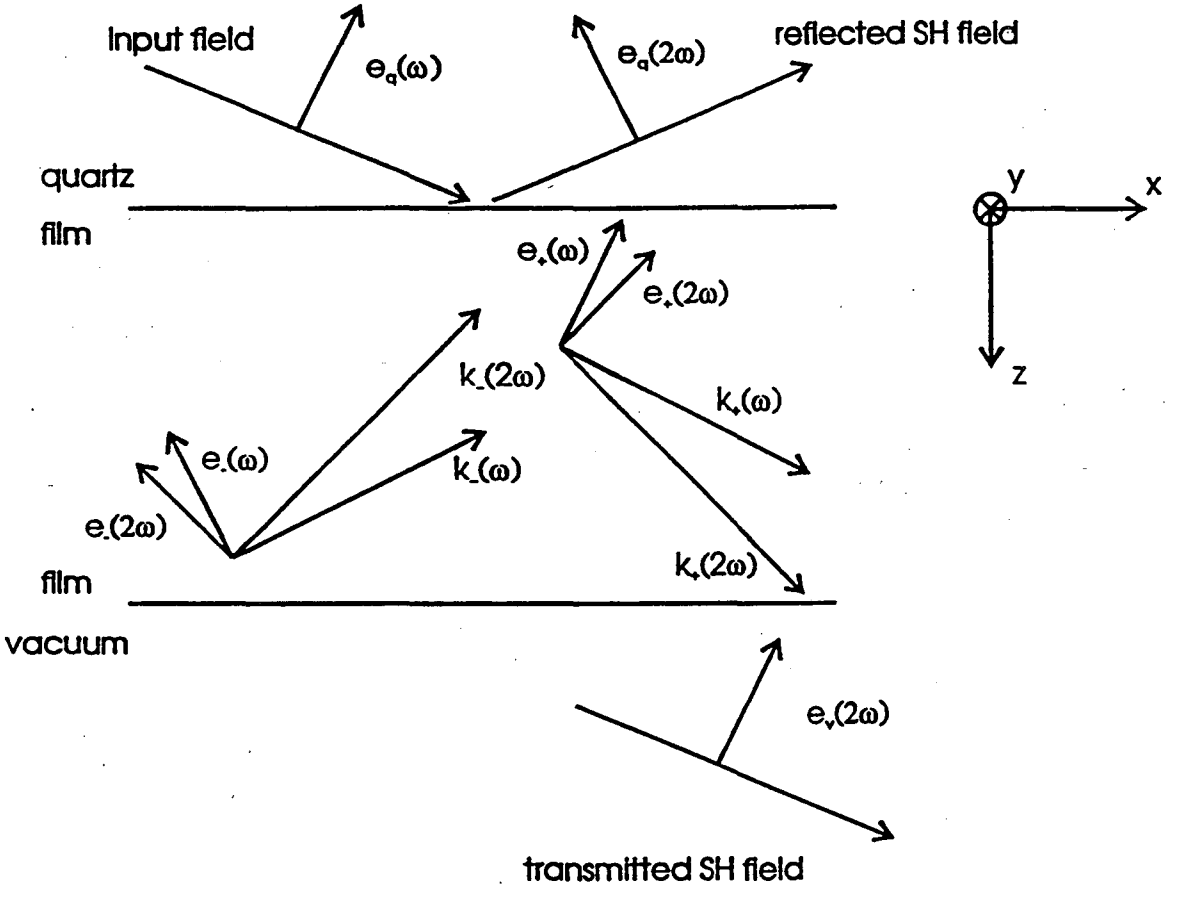
Input field
$e_q(\omega)$
$e_q(2\omega)$
reflected SH field
quartz
film
y
x
z
$e_+(\omega)$
$e_+(2\omega)$
$k_-(2\omega)$
$k_+(\omega)$
$e_-(\omega)$
$k_-(\omega)$
$e_-(2\omega)$
$k_+(2\omega)$
film
vacuum
$e_v(2\omega)$
transmitted SH field

Fig 1

III. Second Order Nonlinear Spectroscopy of C_{60} Thin Films

Introduction

Since the initial discovery of C_{60}, many calculations and measurements have been carried out to understand the electronic structure of C_{60}. However, its properties near the band gap are still not well understood. They are however important, as these electronic states play a key role in achieving superconductivity in alkali-doped C_{60}[1], in the reaction of C_{60} with oxygen in the presence of ultraviolet light, which leads to ring scission[2], and in the formation of an ordered overlayer of C_{60} on a relatively inert Au(111) surface[3,4].

Extensive work using photoemission [5], linear optical spectroscopy [6,7,8] and third order nonlinear optical spectroscopy [9,10,11] has been performed to elucidate the electronic structure near the band gap. Results from linear spectroscopy have shown four strong peaks in the visible to ultraviolet region, with the lowest energy peak at 2.8 eV. However, results from High Resolution Electron Energy Loss Spectroscopy (HREELS) studies show that there are excitations below 2.8 eV which are electric dipole (ED) forbidden[12]. Tunable SHG on C_{60} has been performed and a strong magnetic dipole(MD) excitation has been observed at 1.81 eV[13]. The theory predicts a pure electric quadrupole (EQ) excitation at about 2.3 eV which has not been observed

experimentally[17]. In this section we first discuss the low energy excitation spectrum of C_{60} and then show how second-order nonlinear spectroscopy can be used to observe and distinguish both EQ and MD excitations of C_{60}.

The electronic energy level for the isolated C_{60} molecule near the HOMO-LUMO(highest unoccupied molecular orbital-lowest unoccupied molecular orbital) gap is shown in Fig. 1. This figure includes the single electron diagram(Fig. 1a)) and multi-electron level diagram(Fig. 1b)), which takes into account the electron-electron interactions of C_{60}. Note that the HOMO-LUMO transitions are all ED(electric dipole) forbidden. However, the multiplet splitting shown in the multi-electron-level diagram(see Fig. 1b)) gives rise to both pure EQ and MD allowed transitions. The ^1A_g to $^1T_{1g}$ transition, with an energy of 1.81 eV, is MD allowed while the ^1A_g to ^1H_g transition, with an energy of about 2.3 eV, is EQ allowed[13]. Excitations from $^1A_{1g}$ to ^1G_g and $^1T_{2g}$ symmetry are neither MD nor EQ allowed. In principle, one should be able to observe these pure MD and EQ transitions in the linear absorption spectroscopy. Of course these peaks will be much weaker than the ED transitions. To investigate this possibility should consider the linear spectrum, shown in Figures 2 and 3[8]. Figure 2 shows the linear absorption spectrum from 200nm to 700nm. The most likely assignment of the 4 strong peaks is shown in table 1. The probable wavelength of the EQ transition is 532nm and the wavelength

of the MD transition is 685nm. Instead of peaks at these positions, one observes a long "tail" originating from the lowest energy allowed ED transition at 2.8 eV. Figure 3 gives an expanded view of the region of interest (note the abscissa has units of eV) and one can see more clearly this absorption tail, which extends down to about 1.8 eV before decreasing sharply. Presumably, this tail comes from the broadening of the ED transitions due to intermolecular interactions in the solid state. Contaminants, structural defects, and disorder may also contribute to absorption in this region. As a result, it appears that the EQ and MD peaks cannot to observed due to this relatively strong absorption background. One way to solve this problem is to somehow suppress this background with respect to the EQ and MD peaks. This can be accomplished by second-order sum frequency generation (SFG) spectroscopy. Because the C_{60} film is centrosymmetric, the sum frequency generation is forbidden even if the SF is at an ED resonance. Therefore in SFG, the background due to the ED transition will be suppressed, and should be the same order of magnitude as the EQ and MD peaks. If one performs the experiment using two input beams at frequencies ω_1 and ω_2 and varies ω_1 and/or ω_2 such that the sum frequency $\omega_S=\omega_1+\omega_2$ ranges from energies of 1.5 to 3.0 eV then the sharp peaks at 1.8 and 2.3 eV should be visible on top of the background.

In the following sections, we will derive expressions for the resonant second-order nonlinear polarization of the centrosymmetric C_{60} thin film. Then, a simple microscopic model is used to estimate the nonlinear EQ and MD susceptibilities of the C_{60} molecule.

Resonant SFG from a Homogeneous Isotropic Medium

This derivation is analogous to the derivation of the SH nonlinear polarization in chapter 2. We consider again here an isotropic film, which is a good approximation for C_{60} films. The expression for the effective nonlinear polarization is identical to Eq. 12 of Chapter 2, with 2ω replaced by $\omega_S=\omega_1+\omega_2$. To the order linear in spatial gradient in $\vec{P}^{(2)}(\omega_s=\omega_1+\omega_2)$, we have

$$\begin{aligned}\vec{P}_d^{(2)} &= \vec{\chi}^{D}:\vec{E}(\omega_1)\vec{E}(\omega_2) + \vec{\chi}^{P1}:\vec{E}(\omega_1)\nabla\vec{E}(\omega_2) + \vec{\chi}^{P2}:\vec{E}(\omega_2)\nabla\vec{E}(\omega_1)\\ \vec{Q}^{(2)} &= \vec{\chi}^{Q}:\vec{E}(\omega_1)\vec{E}(\omega_2)\\ \vec{M}^{(2)} &= \vec{\chi}^{M}:\vec{E}(\omega_1)\vec{E}(\omega_2)\end{aligned} \qquad [1]$$

As in chapter 2, $\vec{\chi}^{D}$ describes a local response, $\vec{\chi}^{P1}$, $\vec{\chi}^{P2}$, $\vec{\chi}^{Q}$, and $\vec{\chi}^{M}$ are nonlocal. Note, however, that in the case of sum frequency generation, we have in general two nonequivalent terms $\vec{\chi}^{P1}$ and $\vec{\chi}^{P2}$. If we have $\omega_1=\omega_2$ then above relations reduce to Eq. 13 of Chapter 2. Also, if there is spatial inversion symmetry and time reversal symmetry, then $\vec{\chi}^{M}$ is proportional to the antisymmetric tensor of the third rank and therefore $\chi^{M}_{ijk}=\chi^{M}_{jki}=\chi^{M}_{kij}=-\chi^{M}_{jik}=-\chi^{M}_{ikj}=-\chi^{M}_{kji}$, which is only true if $\omega_1 \neq \omega_2$. Otherwise we would obtain $\vec{M}(2\omega)=0$

since $\chi^{M}_{ijk}(2\omega) = \chi^{M}_{ikj}(2\omega)$ [10]. Using these relations, we can find $\vec{P}^{(2)}(\omega_s)$ in the form

$$
\begin{aligned}
P_i^{(2)}(\omega_1+\omega_2) &= \delta_1'\left[\vec{E}(\omega_2)\cdot\nabla\right]E_{1i}(\omega_1)+\delta_2'\left[\vec{E}_1(\omega_1)\cdot\nabla\right]E_{2i}(\omega_2) \\
&+\beta_1 E_{2i}(\omega_2)\left[\nabla\cdot\vec{E}_1(\omega_1)\right]+\beta_2 E_{1i}(\omega_1)\left[\nabla\cdot\vec{E}_2(\omega_2)\right] \\
&+\gamma_1\left[\vec{E}_2(\omega_2)\cdot\nabla_i\vec{E}_1(\omega_1)\right]+\gamma_2\left[\vec{E}_1(\omega_1)\cdot\nabla_i\vec{E}_2(\omega_2)\right]-\nabla_j\chi^{Q}_{ijkl}E_{1k}(\omega_1)E_{2l}(\omega_2) \\
&+\frac{c}{\omega_s}\chi^{M}\left[\left(\vec{k}_1(\omega_1)+\vec{k}_2(\omega_2)\right)\times\left(\vec{E}_1(\omega_1)\times\vec{E}_2(\omega_2)\right)\right]_i
\end{aligned}
\qquad [2]
$$

with $\delta_h' = (\delta_h - \beta_h - 2\gamma_h) = 2\left(\chi_4^{Ph} - \chi_3^{Q}\right)$

$$\delta_h = 2(\chi_1^{Ph} - \chi_1^{Q})$$

$$\beta_h = 2\left(\chi_2^{Ph} - \chi_3^{Q}\right)$$

$$\gamma_h = \chi_3^{Ph} - \chi_2^{Q}$$

where

$$\chi_1^{Q(P)} = \chi_{iiii}^{Q(P)}, \quad \chi_2^{Q(P)} = \chi_{iijj}^{Q(P)},$$
$$\chi_3^{Q(P)} = \chi_{ijij}^{Q(P)}, \quad \chi_4^{Q(P)} = \chi_{ijji}^{Q(P)},$$

$$\chi^{M} = \chi^{M}_{ijk},$$

and h=1,2. As in Chapter 2, $\nabla\cdot\vec{E}=0$ in a homogeneous, isotropic dielectric and the β_1, β_2 terms in $P_i^{(2)}(\omega_1+\omega_2)$ do not contribute to bulk SFG. Also, the $\nabla_j\chi^{Q}_{ijkl}$ term vanishes in a homogeneous bulk. Substituting the equation

$$\vec{E}_i(\omega_i,\vec{r}) = \vec{E}_i(\omega_i)\cdot e^{i(\vec{k}(\omega_i)\cdot\vec{r}-\omega_i t)}$$

where i = 1, 2 we obtain

$$P_i^{(2)}(\omega_1+\omega_2) = i\delta_1\left[\vec{k}_1(\omega_1)\cdot\vec{E}_2(\omega_2)\right]E_{1i}(\omega_1)+i\delta_2\left[\vec{k}_2(\omega_2)\cdot\vec{E}_1(\omega_1)\right]E_{2i}(\omega_2)$$
$$+i(k_{1i}(\omega_1)\gamma_1+k_{2i}(\omega_2)\gamma_2)\left[\vec{E}_1(\omega_1)\cdot\vec{E}_2(\omega_2)\right] \qquad [3]$$
$$+\frac{c}{\omega_s}\chi^M\left[\left(\vec{k}_1(\omega_1)+\vec{k}_2(\omega_2)\right)\times\left(\vec{E}_1(\omega_1)\times\vec{E}_2(\omega_2)\right)\right]_i$$

If the two input beams at ω_1 and ω_2 are collinear, then the output sum frequency polarization is aligned along the direction of propagation and cannot radiate, ignoring the boundary effects. Therefore, in order to observe the bulk SFG from a centrosymmetric, homogeneous medium, two noncollinear beams must be used.

We now consider two special cases. First we consider the case in which the sum frequency ω_S is resonant with the EQ transition while the two input frequencies, ω_1 and ω_2 are nonresonant. In this case, $\vec{\chi}^Q \rangle\rangle \vec{\chi}^P, \vec{\chi}^M$ and we can neglect the contributions from $\vec{\chi}^P$ and $\vec{\chi}^M$. The expression for the effective polarization $P_i^{(2)}(\omega_1+\omega_2)$ then becomes

$$P_i^{(2)}(\omega_1+\omega_2) = -i\chi_3^Q\left[\left[\vec{k}_1(\omega_1)\cdot\vec{E}_2(\omega_2)\right]E_{1i}(\omega_1)+\left[\vec{k}_2(\omega_2)\cdot\vec{E}_1(\omega_1)\right]E_{2i}(\omega_2)\right]$$
$$-i\chi_2^Q(k_{1i}(\omega_1)+k_{2i}(\omega_2))\left[\vec{E}_1(\omega_1)\cdot\vec{E}_2(\omega_2)\right] \qquad [4]$$

The first term gives a nonlinear polarization perpendicular ($\bar{P}_{\perp}^{(2)}(\omega_1+\omega_2)$) to the sum frequency wave vector ($\bar{k}_s=\bar{k}_1+\bar{k}_2$) and the second term gives a nonlinear polarization parallel ($\bar{P}_{\parallel}^{(2)}(\omega_1+\omega_2)$) to the sum frequency wave vector. Choosing to observe the sum siganl along $\bar{k}_s$, and using an aperture of 0.5 degrees, then the $\sin(\theta)$ dependence of the electric dipole radiation field effectively supresses the contribution from $\bar{P}_{\parallel}^{(2)}(\omega_1+\omega_2)$ parallel to $\bar{k}_s$. Therefore, one may neglect the contribution from χ_2^{Q}(See Eqn. 4). We will see in Chapter 5 that this condition is easily achieved in the experiment. Therefore, the resonant nonlinear response can be characterized by one independent nonlinear susceptibility, χ_3^{Q}. Now, Eqn. 4 can be rewritten if we assume that the z axis denotes the direction of the sum frequency polarization wave vector,

$k_S(\omega_1+\omega_2)$, the x axis denotes the orthogonal direction to z in the plane of polarization, angles $\theta_1(\theta_2)$ are the angles made between the beam at $\omega_1(\omega_2)$ and the sum frequency polarization wave vector, angles α and β denote the angle of polarization measured clockwise from the plane of incidence(x-z plane) made by the input beams at ω_1 and ω_2, respectively. A schematic of this geometry is shown in Figure 4. The polarization along the x and y directions then become

$$P_x^{(2)}(\omega_1+\omega_2) = -i\chi_3^Q k_s(\omega_1+\omega_2)\cos(\alpha)\cos(\beta)\sin(\theta_2-\theta_1)[E_1(\omega_1)E_2(\omega_2)]$$
$$P_y^{(2)}(\omega_1+\omega_2) = -i\chi_3^Q k_s(\omega_1+\omega_2)[\sin(\alpha)\cos(\beta)\sin(\theta_2)-\sin(\beta)\cos(\alpha)\sin(\theta_1)][E_1(\omega_1)E_2(\omega_2)]$$

[5]

Note that if $\omega_1=\omega_2=\omega$ then $\theta_1=\theta_2$ and $P_x^{(2)}(\omega_1+\omega_2)=0$, independent of the input polarizations. Even if ω_1 is not equal to ω_2 then $P_x^{(2)}(\omega_1+\omega_2)$ is suppressed by the $\sin(\theta_1-\theta_2)$ factor. The magnitude of $P_y^{(2)}(\omega_1+\omega_2)$ depends on the input polarizations (α and β) and may be suppressed or enhanced, depending on the values of α and β. The maximum occurs when α = 45°, -45°, 135°,-135° and $\beta=\alpha\pm90°$. The minimum occurs when $\beta=\alpha$.

Now we consider the case in which the output frequency ω_S is resonant with a MD transition. Therefore, we have $\vec{\chi}^M \rangle\rangle \vec{\chi}^Q, \vec{\chi}^P$ and Eq. 4 simplifies to

$$P_i^{(2)}(\omega_1+\omega_2) = \frac{c}{\omega_s}\chi^M\left[\left(\vec{k}_1(\omega_1)+\vec{k}_2(\omega_2)\right)\times\left(\vec{E}_1(\omega_1)\times\vec{E}_2(\omega_2)\right)\right]_i . \qquad [6]$$

Using the coordinate system and parameters shown in Fig. 4, one obtains

$$P_x^{(2)}(\omega_1+\omega_2) = \frac{c}{\omega_s}\chi^M k_s(\omega_1+\omega_2)\cos(\alpha)\cos(\beta)\sin(\theta_2+\theta_1)[E_1(\omega_1)E_2(\omega_2)]$$
$$P_y^{(2)}(\omega_1+\omega_2) = \frac{c}{\omega_s}\chi^M k_s(\omega_1+\omega_2)[\sin(\alpha)\cos(\beta)\sin(\theta_2)+\sin(\beta)\cos(\alpha)\sin(\theta_1)][E_1(\omega_1)E_2(\omega_2)]$$

In this case $P_x^{(2)}(\omega_1+\omega_2)$ is maximized for p polarization of both input frequencies and at $\theta_1+\theta_2=90°$. The component P_y is maximized at α= 45°,135°, -45°, -135° and $\beta=\alpha$ and is minimized when $\beta=\alpha\pm90°$, which is just reversed from the case for the polarization dominated by the EQ transition. This implies that one may be able to distinguish EQ and MD dominated responses in isotropic media using the sum frequency technique. In the case of C_{60} this technique is particularly applicable since the lowest energy electronic excitations of the C_{60} free molecule are EQ and MD allowed but ED forbidden.

Estimate of the EQ and MD Susceptibilities of C_{60}

At this point we estimate the resonant nonlinear susceptibilities χ_3^Q and χ^M for the C_{60} solid film. The calculation is carried out for the case in which χ_3^Q and χ^M are enhanced by the EQ and MD transitions across the HOMO-LUMO gap (See Fig. 1b), respectively. The output sum frequency ω_s is resonant with the EQ and MD transitions but the input frequencies ω_1 and ω_2 are non resonant.

We use the free electron model for the C_{60} molecule, where it is assumed that the 60 π electrons are non-interacting and confined to move on a thin spherical shell of radius

3.55 Angstroms. The validity of this approximation can be argued as follows. From detailed microscopic calculations on the C_{60} molecule[17], it has been shown that one valence electron per carbon atom on the C_{60} molecule occupies the π molecular orbitals, which are loosely bound compared to the other three valence electrons of each carbon atom. Therefore, only the π electrons of C_{60} are considered in this model. Because our experiments probe the 1 to 3 eV energy range, only those states occupied by the π electrons are important.

We now derive the expressions for the resonant EQ and MD nonlinear susceptibilities of C_{60} using the free electron model. Let us start with the radial part of the Hamiltonian for a system with spherical symmetry;

$$H = -\frac{\hbar^2}{2m_e}\left(\frac{\partial^2}{\partial r^2} + \left(\frac{2}{r}\frac{\partial}{\partial r}\right) - \frac{l(l+1)}{r^2}\right) + V(r) \qquad [8]$$

Taking a very narrow spherical potential well of thickness a centered about a radius R with infinitely high walls, the Hamiltonian can then be approximated:

$$H = -\frac{\hbar^2}{2m_e}\left(\frac{\partial^2}{\partial r^2} + \frac{2}{r}\frac{\partial}{\partial r} - \frac{l(l+1)}{R^2}\right) + 0 \quad R-a/2 < r < R+a/2$$

[9]

$V(r)=\infty$ r < R-a/2, r > R+a/2

The radial and angular part of the solution are completely separable and the solutions to the corresponding Schroedinger equation are

$$\Psi_{nlm}(r)=Y_{lm}(\vartheta,\varphi)R(r) \qquad R-a/2 < r < R+a/2 \qquad [10]$$

$\Psi_{nlm}(r)=0$ r < R-a/2, r > R+a/2

where $Y_{lm}(\theta,\phi)$ are the spherical harmonics and the R(r) are the radial parts of the wave function. To solve for R(r), we make the substitution u(r)=rR(r) and Schroedinger equation for R-a/2<r<R+a/2 becomes

$$-\frac{\hbar^2}{2m_e}\left(\frac{\partial^2}{\partial r^2}-\frac{l(l+1)}{R^2}\right)u(r)=Eu(r) \qquad [11]$$

This is just the Schroedinger equation for the one-dimensional box. Solving with the appropriate boundary conditions and then using R(r)=u(r)/r we obtain

$$R_n(r)=\begin{cases}\sqrt{\frac{2}{a}}\dfrac{\cos\left(\frac{2(2n-1)\pi}{a}(r-R)\right)}{r}, & n=0,1,2,\ldots \\ \sqrt{\frac{2}{a}}\dfrac{\sin\left(\frac{2n\pi}{a}(r-R)\right)}{r}, & n=1,2,3,\ldots\end{cases} \qquad [12]$$

The corresponding energy levels are given by

$$E_{nl}=\frac{\hbar^2}{2m_e}\frac{4n^2\pi^2}{a^2} + \frac{\hbar^2}{2m_e}\frac{l(l+1)}{R^2} \quad n=1,2,3,\ldots \quad l=0,1,2,\ldots, \qquad [13]$$

where m_e is the mass of the electron. The energy degeneracy is 2(2l+1), where the factor of 2 accounts for the spin degeneracy. In the thin spherical shell model we have a << R and so $E_{n=2,l}-E_{n=1,l} >> E_{n=1,l'}-E_{n=1,l}$. Therefore, when one fills up the energy levels with 60 electrons(applying the exclusion principle), all levels up to l=5 are filled, with the l=5 states partially filled. The n=2 level is far above the fermi level.

The important term for the electric dipole interaction hamiltonian is the electric dipole operator and it is given by

$$-ez = -er\sqrt{\frac{4\pi}{3}}Y_{1,0}(\theta,\phi), \qquad [14]$$

and the ED matrix element between the states $Y_{lm}(\theta,\varphi)$ and $Y_{l'm'}(\theta,\varphi)$ is

$$\langle Y_{lm}|-ez|Y_{l',m'}\rangle = -eR\sqrt{\frac{(l+m+1)(l-m+1)}{(2l+1)(2l+3)}}\delta_{l',l}\delta_{m',m\pm1} \qquad [15]$$

The EQ operator is

$$Q_{xy} = -exy = -eR^2\sqrt{\frac{2\pi}{15}}i\left(Y_{2,-2} - Y_{2,2}\right) \qquad [16]$$

and the matrix element between states $Y_{lm}(\theta,\varphi)$ and $Y_{l'm'}(\theta,\varphi)$ is given by

$$\langle Y_{lm}|-eR^2\sqrt{\frac{2\pi}{15}}i\left(Y_{2,-2} - Y_{2,2}\right)|Y_{l',m'}\rangle \qquad [17]$$

Finally, the MD operator can be written as

$$M_z = \frac{eL_z}{m_e c} = -\frac{e\hbar}{m_e c}\frac{\partial}{\partial\phi}, \qquad M_z|Y_{lm}\rangle = -\frac{ime\hbar}{m_e c}|Y_{lm}\rangle \qquad [18]$$

and the matrix element between states $Y_{lm}(\theta,\varphi)$ and $Y_{l'm'}(\theta,\varphi)$ is

$$\langle Y_{lm}|M_z|Y_{l'm'}\rangle = -\frac{ime\hbar}{m_e c}\delta_{l',l}\delta_{m',m} \qquad [19]$$

The selection rules for the ED, EQ, MD transitions are

$$\begin{aligned} &ED \quad \Delta l = \pm 1, \Delta m = \pm 1 \\ &EQ \quad \Delta l = 0, \pm 2, \Delta m = \pm 2 \\ &MD \quad \Delta l = 0, \Delta m = 0 \end{aligned} \qquad [20]$$

We use Eqns. 15-21 to evaluate the numerator of the microscopic expression for the resonant EQ and MD nonlinear susceptibilities:

$$N_{ijj}^{(EQ)} = 2\sum_{m,m',m''}\langle Y_{lm}|r_i|Y_{l'm'}\rangle\langle Y_{l'm'}|r_j|Y_{l''m''}\rangle\langle Y_{l''m''}|Q_{ij}|Y_{lm}\rangle = \frac{2eR^4 l(l+1)}{15(2l+3)} \qquad [21]$$

$$N_{ijk}^{(MD)} = 2\sum_{m,m',m''}\langle Y_{lm}|r_i|Y_{l'm'}\rangle\langle Y_{l'm'}|r_j|Y_{l''m''}\rangle\langle Y_{l''m''}|M_k|Y_{lm}\rangle = \frac{-2\hbar R^2 l(l+1)}{3m_e\omega_s} \qquad [22]$$

for the EQ and MD susceptibilities, respectively. The Clebsch-Gordon coefficients have been used to evaluate the matrix elements and the factor of 2 takes into account the spin degeneracy.

The microscopic nonlinear EQ and MD susceptibilities resonant at $\omega_S=\omega_1+\omega_2$ are derived from the density matrix formalism[16]:

$$\chi_3^Q = \chi_{ijij}^Q = N\frac{e^2}{\hbar^2}\sum_{gnn'} \frac{<Q_{ij}>_{gn}}{(\omega_1+\omega_2-\omega_{ng}+i\Gamma_{ng})}\left(\frac{<r_i>_{nn'}<r_j>_{n'g}}{(\omega_2-\omega_{n'g}+i\Gamma_{n'g})}+\frac{<r_j>_{nn'}<r_i>_{n'g}}{(\omega_1-\omega_{n'g}+i\Gamma_{n'g})}\right)\rho_g^{(0)}$$
$$-\frac{<r_i>_{ng}<r_j>_{gn'}<Q_{ij}>_{n'n}}{(\omega_1+\omega_2-\omega_{nn'}+i\Gamma_{nn'})}\left(\frac{1}{(\omega_2+\omega_{n'g}+i\Gamma_{n'g})}+\frac{1}{(\omega_1-\omega_{ng}+i\Gamma_{ng})}\right)\rho_g^{(0)}$$
$$-\frac{<r_j>_{ng}<r_i>_{gn'}<Q_{ij}>_{n'n}}{(\omega_1+\omega_2-\omega_{nn'}+i\Gamma_{nn'})}\left(\frac{1}{(\omega_2-\omega_{ng}+i\Gamma_{ng})}+\frac{1}{(\omega_1+\omega_{n'g}+i\Gamma_{n'g})}\right)\rho_g^{(0)} \quad [23]$$

$$\chi_{ijk}^M = N\frac{e^2}{\hbar^2}\sum_{gnn'} \frac{<M_i>_{gn}}{(\omega_1+\omega_2-\omega_{ng}+i\Gamma_{ng})}\left(\frac{<r_j>_{nn'}<r_k>_{n'g}}{(\omega_2-\omega_{n'g}+i\Gamma_{n'g})}+\frac{<r_k>_{nn'}<r_j>_{n'g}}{(\omega_1-\omega_{n'g}+i\Gamma_{n'g})}\right)\rho_g^{(0)}$$
$$-\frac{<r_j>_{ng}<r_k>_{gn'}<M_i>_{n'n}}{(\omega_1+\omega_2-\omega_{nn'}+i\Gamma_{nn'})}\left(\frac{1}{(\omega_2+\omega_{n'g}+i\Gamma_{n'g})}+\frac{1}{(\omega_1-\omega_{ng}+i\Gamma_{ng})}\right)\rho_g^{(0)}$$
$$-\frac{<r_k>_{ng}<r_j>_{gn'}<M_i>_{n'n}}{(\omega_1+\omega_2-\omega_{nn'}+i\Gamma_{nn'})}\left(\frac{1}{(\omega_2-\omega_{ng}+i\Gamma_{ng})}+\frac{1}{(\omega_1+\omega_{n'g}+i\Gamma_{n'g})}\right)\rho_g^{(0)} \quad [24]$$

where r_i is the component of the position, Q_{ij} is the electric quadrupole operator, M_i is the magnetic dipole operator (See Eqns. 15,17,19) , N in the number density of molecules. Here $\rho_g^{(0)}$ is given by the Fermi-Dirac distribution and is 1 for occupied orbitals and 0 for unoccupied orbitals. We have already eliminated the two nonresonant terms having the denominator $\omega_1+\omega_2+\omega_{ng}+i\Gamma_{ng}$. From this point on we discuss only the EQ susceptibility, since the method for estimating the MD dipole susceptibility is the same. If the output frequency is resonant with the HOMO-LUMO EQ transition, then one need only consider the h_u and t_{1u} states in matrix element of Q_{ij}. However, one sum over all states still exists for the input frequencies, which are not resonant with any of the electronic transitions of C_{60}. In principle, one must sum over all of the states of C_{60} connected by the ED operator(See Eqns. 23 and 24). One can reduce the number of terms in the nonresonant sum by recognizing the correlation between the free electron model and linear combination of orbitals(LCAO) model(see Fig. 1). This correlation is illustrated in Fig. 5[18], where the dashed lines connect the free electron energy levels on the far right to the LCAO energy levels on the far left. The set of orbitals in the middle of Figure 5 represent the nearly free electron model. Because the ED dipole selection rule in the free electron model is $\Delta l=\pm 1$, we expect that those LCAO states derived from l=4,5,and 6 free electron states will be the most significant

contribution to the nonresonant sum in Eqn. 23. Therefore we expect all of the transitions shown in table 1 to contribute, as well as the $h_u \rightarrow g_g$ transition, which is further in the UV and has not been observed by linear optical absorption spectroscopy. Using this approximation and neglecting the damping terms in the nonresonant denominators, we have

$$\chi^{Q}_{ijij} = N\frac{e^2}{\hbar^2}\sum_{\substack{h_u,t_{1u},\\ n}} -\frac{<Q_{ij}>_{h_u t_{1u}}}{(\omega_1+\omega_2-\omega_{t_{1u}h_u}+i\Gamma_{t_{1u}h_u})}\left(\frac{<r_i>_{t_{1u}n}<r_j>_{nh_u}}{(\omega_2-\omega_{nh_u})}+\frac{<r_j>_{t_{1u}n}<r_i>_{nh_u}}{(\omega_1-\omega_{nh_u})}\right)$$
$$-\frac{<r_i>_{t_{1u}n}<r_j>_{nh_u}<Q_{ij}>_{h_u t_{1u}}}{(\omega_1+\omega_2-\omega_{t_{1u}h_u}+i\Gamma_{t_{1u}h_u})}\left(\frac{1}{(\omega_2+\omega_{t_{1u}n})}+\frac{1}{(\omega_1-\omega_{t_{1u}n})}\right)$$
$$-\frac{<r_j>_{t_{1u}n}<r_i>_{nh_u}<Q_{ij}>_{h_u t_{1u}}}{(\omega_1+\omega_2-\omega_{t_{1u}h_u}+i\Gamma_{t_{1u}h_u})}\left(\frac{1}{(\omega_2-\omega_{t_{1u}n})}+\frac{1}{(\omega_1+\omega_{t_{1u}n})}\right) \qquad [25]$$

Here, the h_u and t_{1u} levels are the HOMO and LUMO levels, respectively, which are derived from the l=5 free electron states. The states labeled by "n" refer to those LCAO states derived from the l=6 and l=4 states (See Fig. 5). Note that the first term in the susceptibility involves HOMO states (derived from l=5 spherical harmonics) and the higher energy unoccupied states (derived from the l=6 spherical harmonics) and the next two terms involves the HOMO and

HOMO-1 states(derived the l=5 and l=4 spherical harmonics states, respectively). The calculation is further simplified by replacing the real electron wavefunctions in the numerators of Eqn. 25 with wavefunctions of the free electron model discussed at the beginning of this section. Then, the numerators are taken out from the sums by assuming them to be independent of energy. The sums over terms with energy denominators of nonresonant sums are then approximated by a single average energy denominator. The expression for the resonant EQ susceptibility then simplifies to

$$\chi^{Q}_{ijij} = N\frac{e^2}{\hbar^2}\sum_{\substack{l=5\\ l=6\\ l=4}} \frac{<Q_{ij}>_{55}}{(\omega_1+\omega_2-\omega_{t_{lu}h_u}+i\Gamma_{t_{lu}h_u})}\left(\frac{<r_i>_{56}<r_j>_{65}}{(\overline{\omega_2-\omega_{nh_u}})}+\frac{<r_j>_{56}<r_i>_{65}}{(\overline{\omega_1-\omega_{nh_u}})}\right)$$
$$-\frac{<r_i>_{54}<r_j>_{45}<Q_{ij}>_{55}}{(\omega_1+\omega_2-\omega_{t_{lu}h_u}+i\Gamma_{t_{lu}h_u})}\left(\frac{1}{(\overline{\omega_2+\omega_{t_{lu}n}})}+\frac{1}{(\overline{\omega_1-\omega_{t_{lu}n}})}\right)$$
$$-\frac{<r_j>_{54}<r_i>_{45}<Q_{ij}>_{55}}{(\omega_1+\omega_2-\omega_{t_{lu}h_u}+i\Gamma_{t_{lu}h_u})}\left(\frac{1}{(\overline{\omega_2-\omega_{t_{lu}n}})}+\frac{1}{(\overline{\omega_1+\omega_{t_{lu}n}})}\right)$$

[26]

where $\frac{N_s}{(\overline{\omega_i \pm \omega_{ng}})} = \sum_n \frac{D_{ng}}{(\omega_i \pm \omega_{ng})}$ $i = 1,2$.

Here D_{ng} is the degeneracy factor and N_S is the total number of transitions in the sum. For the first term we have:

$$N_s = 11\times 11\times 13 = 1573$$
$$D_{t_{1g}-h_u} = 5\times 3\times 3 = 45,$$
$$D_{h_g-h_u} = 5\times 5\times 3 = 75$$
$$D_{g_g-h_u} = 5\times 4\times 3 = 60$$

and for the next two terms

$$N_s = 11\times 11\times 9 = 1089$$
$$D_{t_{1u}-h_g+g_g} = 5\times 3\times 9 = 45$$

The terms $\omega_i \pm \omega_{ng}$ are obtained from table 1 and the $h_u \rightarrow g_g$ transition is also obtained from table 1, assuming the energy difference between the h_g and g_g states given in Figure 5 is a reasonable approximation.

To evaluate the numerator, we use Eqn. 22. Since the EQ transition is expected to be at about 2.3 eV and the input energy available from the Nd:YAG laser is $\hbar\omega_1 = 1.15eV$, we have $\hbar\omega_1 \approx \hbar\omega_2 = 1.15eV$. Using N=1.38*$10^{21}$ molecules/cm^3, a linewidth $\Gamma_{t_{1u}-h_u} \approx 0.3eV$ [19], and including the microscopic local field correction[16], we find

$$\chi^{Q}_{ijij}(\omega_1+\omega_2) = 1\times 10^{-14}\ esu.$$

For χ^M we perform the same approximations, using $\hbar\omega_1 = 1.17\,eV, \hbar\omega_2 = .63\,eV$, and $\Gamma = .06$ eV[18], to obtain

$$\frac{c\chi^M_{ijk}}{\omega_s} = 9 \times 10^{-14}\,esu\,.$$

The multiplication of χ^M_{ijk} by c/ω_s allows a direct comparison with χ^Q_{ijij}. These susceptibilities are detectable by photon counting techniques.

Conclusion

In this section we have discussed the advantages of using SFG to probe the low energy ED forbidden electronic states of the C_{60} solid. In the centrosymmetric C_{60}, one can distinguish the EQ and MD transitions by the dependence of the relative polarization of the two noncollinear input beams at different frequencies. Furthermore, using a microscopic model, we have approximately calculated the resonant electric quadrupole and magnetic dipole nonlinear susceptibilities of the C_{60} thin film.

References

1. K. Holczer, et. al. Science **252**, 1154 (1991).

2. A. M Vassallo, S. K. Pang, P. A. Cole-Clarke, M. A. Wilson, J. Am. Chem. Soc. **113**, 7820 (1991).

3. R. J. Wilson, et. al., Nature **348**, 621 (1990).

4. E. I. Altman, and R. J. Colton, Surf. Sc. **279**, 49 (1992).

5. R. W. Lof, et. al. Phys. Rev. Lett. **68** 3924 (1992).

6. A. F. Hebard, R. C. Haddon, R. M. Fleming, and A. R. Kortan, Appl. Phys. Lett. **59**, 2109 (1991).

7. J. Feldmann, et. al., Phys. Stat. Sol. (b) **173** 339 (1992).

8. Skumanich, A. Chem. Phys. Lett. **182**, 486 (1991).

9. J. S. Meth, H. Vanherzeele, Y. Wang, Chem. Phys. Lett. **197** 26 (1992).

10. Z. H. Kafafi, et. al. Chem. Phys. Lett. **188** 492 (1992).

11. W. H. Blau, et. al. Phys. Rev. Lett. **67** 1423 (1991).

12. G. Gensterblum, et. al. Phys. Rev. Lett. **67** 2171 (1991).

13. B. Koopmans, A. M. Janner, H. T. Jonkman, G. A. Sawatzky, and F. van der Woude, Phys. Rev. Lett. **71**, 3569 (1993).

14. S. Leach, et. al., J. Chem. Phys. **160**, 451 (1992).

15. Pershan, P. S., Phys. Rev. **130**, 919 (1963).

16. Y. R. Shen, Principles of Nonlinear Optics, Wiley and Sons, 1984.

17. F. Negri, G. Orlandi, F. Zerbetto, Chem. Phys. Lett. **144**, 31 (1988).

18. B. Koopmans, PhD Thesis 1994.

19. Hai-Tian Zhou, Northwestern University, private communication.

Figure Captions

Fig. 1

Energy level diagrams of molecular C_{60} near the HOMO-LUMO (h_u-t_{1u}) transitions of C_{60}. (a) Single electron level diagram, and (b) Multi-electron level diagram.

Fig. 2

UV-Visible Spectra of two films of C_{60} [8]

Fig. 3

Visible-Near IR Spectrum of a C_{60} film [8]

Fig. 4

Schematic of Nonlinear Sum Frequency Generation Experiment

Fig. 5

Molecular orbitals of the C_{60} isolated molecule. Left: The LCAO model. Middle: Nearly Free Electron Model Right: The Free Electron Model

Tables

Table 1

Linear Absorption Spectrum Assignment

for C_{60}

Transition	Energy(eV)	Wavelength(nm)
$h_u \rightarrow t_{1g}$	2.8	443
$hg+g_g \rightarrow t_{1u}$	3.6	346
$h_u \rightarrow h_g$	4.6	268
$hg+g_g \rightarrow t_{2u}$	5.6	220

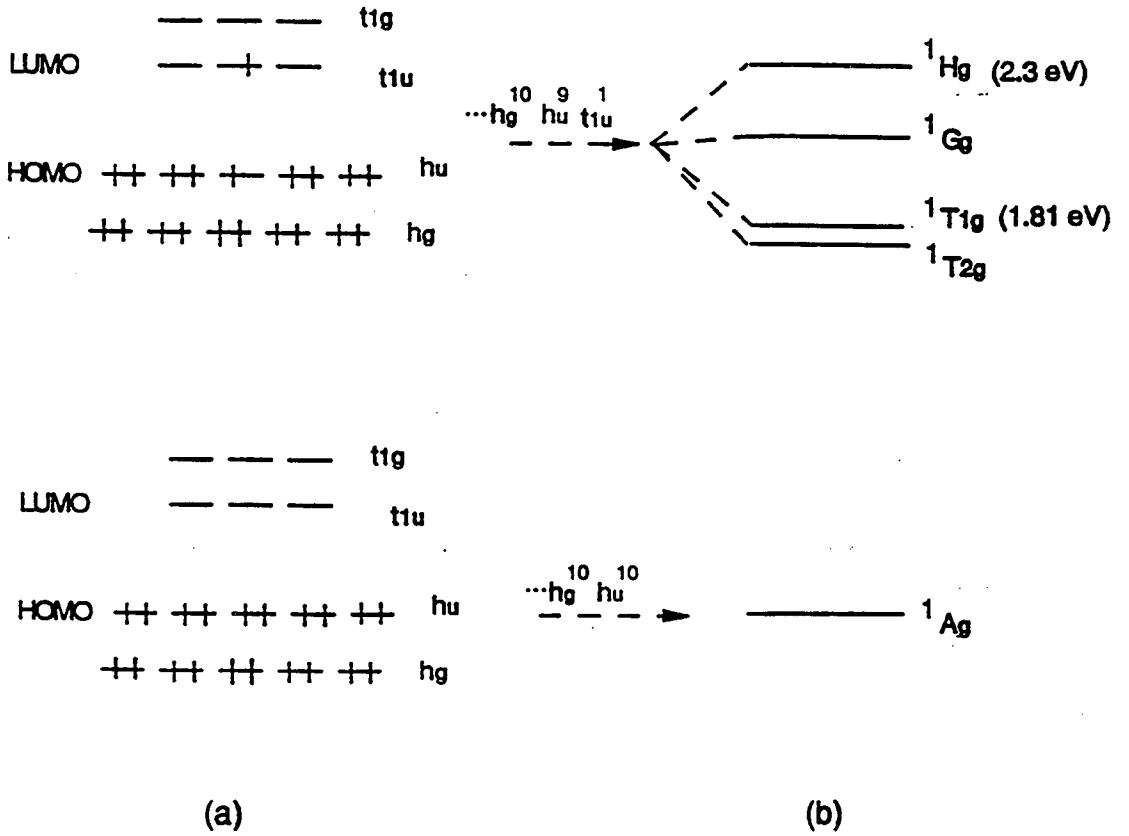
t1g
LUMO
t1u
HOMO
hu
hg
···hg10 hu9 t1u1
1Hg (2.3 eV)
1Gg
1T1g (1.81 eV)
1T2g
t1g
LUMO
t1u
HOMO
hu
hg
···hg10 hu10
1Ag
(a)
(b)

Fig. 1

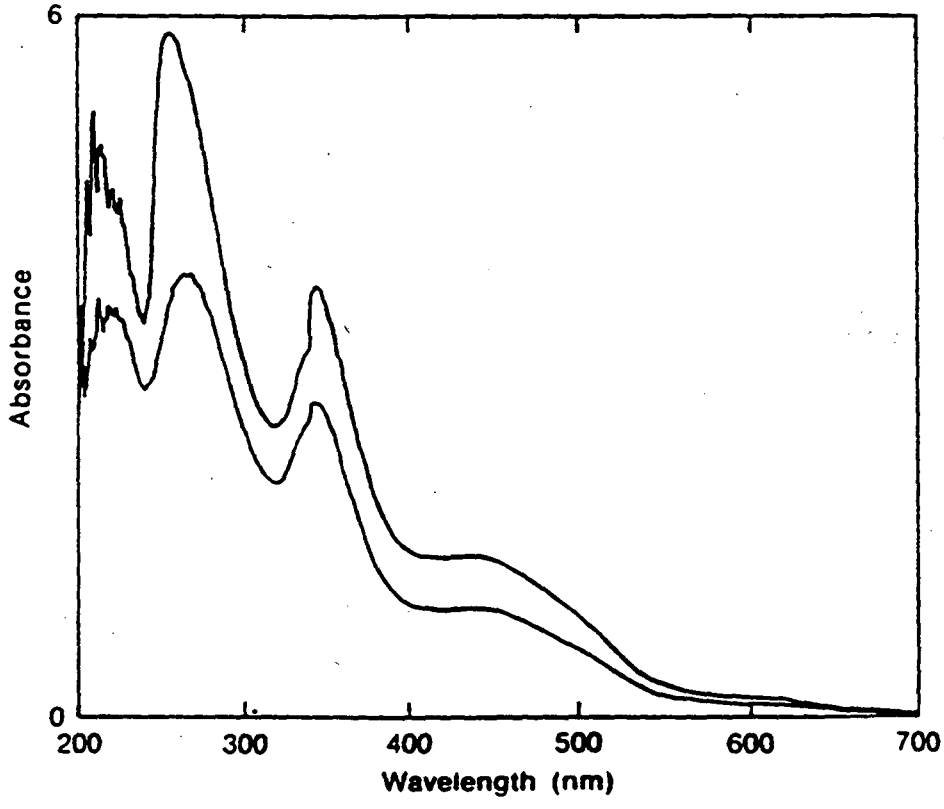

Fig. 2

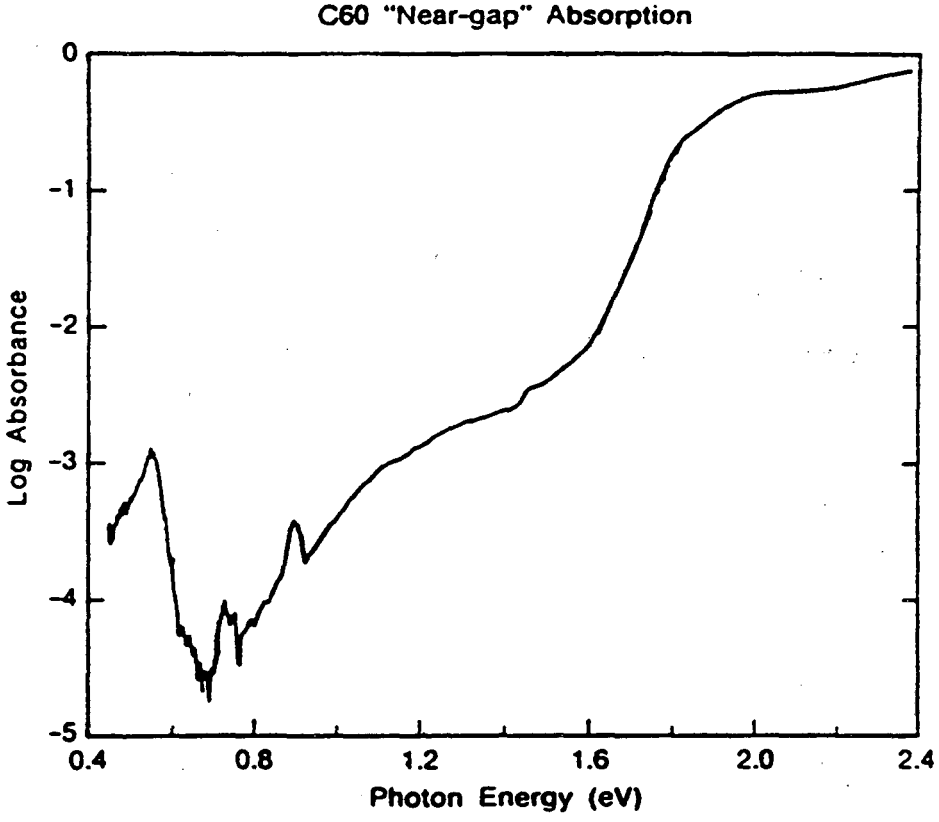

Fig. 3. Visible and near-IR spectrum of C_{60} thin film.

Fig. 3

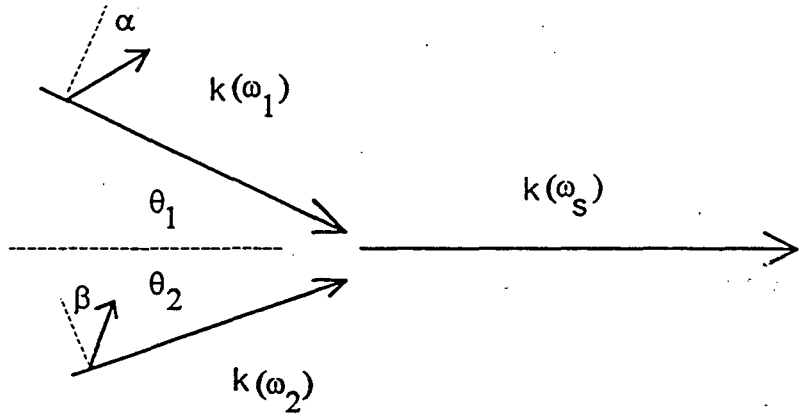

Fig. 4

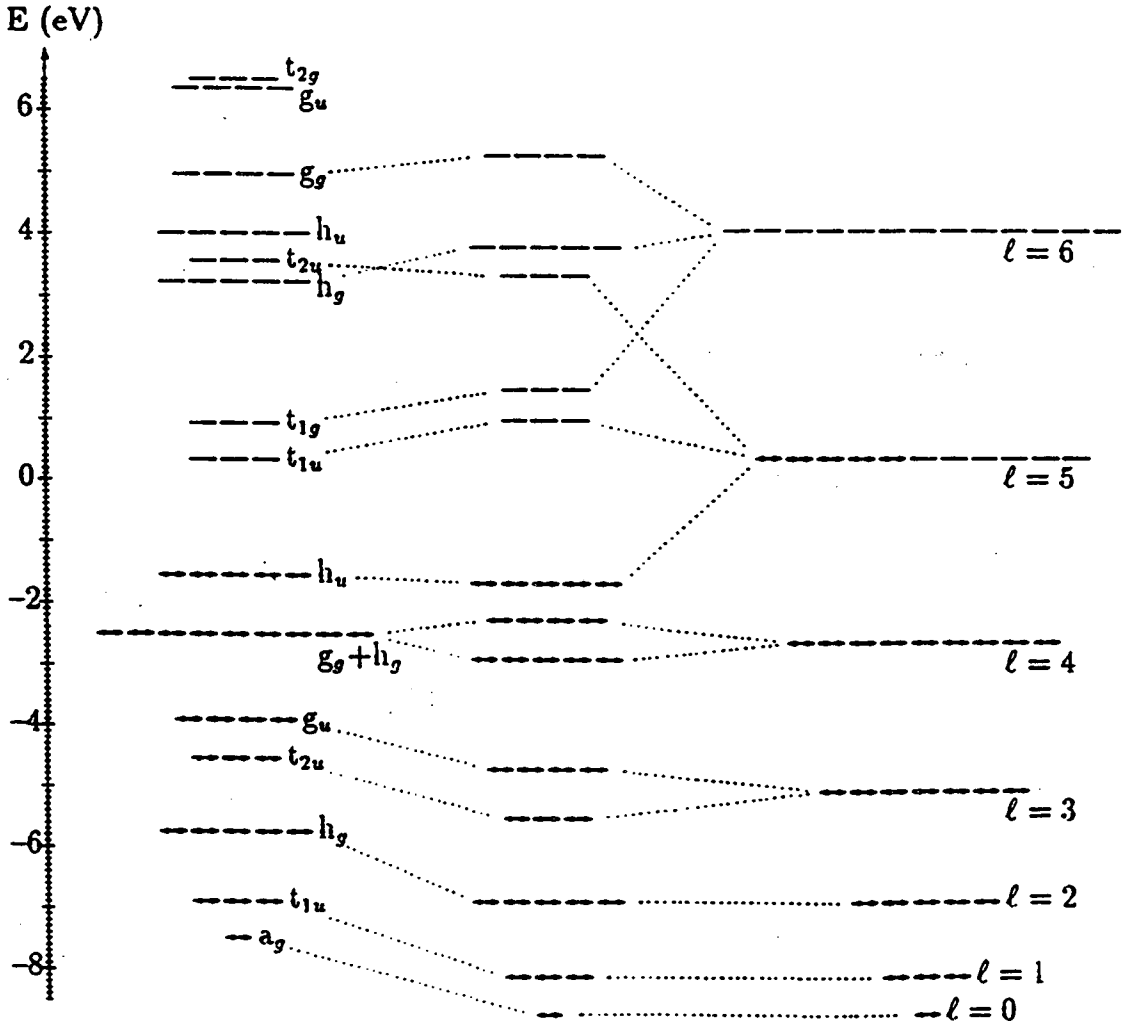
E (eV)
6
4
2
0
−2
−4
−6
−8
t_{2g}
g_u
g_g
h_u
t_{2u}
h_g
t_{1g}
t_{1u}
h_u
g_g+h_g
g_u
t_{2u}
h_g
t_{1u}
a_g
$\ell = 6$
$\ell = 5$
$\ell = 4$
$\ell = 3$
$\ell = 2$
$\ell = 1$
$\ell = 0$

Fig. 5

IV. SHG from C60 Thin Films at λ=1.064 μm

Introduction and Background

In this section we report measurements of optical second harmonic generation (SHG) from C_{60} thin films. The C_{60} molecules crystallize in an fcc lattice that also has inversion symmetry. Therefore SHG is forbidden in the electric dipole approximation at both *macroscopic* and *microscopic* levels. Thus, SHG from the C_{60} bulk must come from nonlocal electric quadrupole and/or magnetic dipole contributions. In the case of C_{60} films, SHG can in principle also have contributions from the surface layers where the inversion symmetry is broken by the local environment. The main purpose of this experiment is to deduce separately the surface and bulk nonlinear optical susceptibilities and thereby determine the source of the second harmonic generation from C_{60} films.

There have been several previous reports of SHG from C_{60} films. Though Hoshi et al[1] were the first to report SHG, no attempt was made to quantify the SH signal and to identify the source of the signal. Wang and co-workers[2] measured SHG from C_{60} thin films in air using 1064 nm fundamental light. After measuring the SH signal for several films of different thickness they concluded that the major contribution to the SH signal was from the bulk of the film. However, this conclusion cannot be drawn from their data,

since their experiment does not distinguish between the bulk and surface contributions localized at the two interfaces of the film[3]. More recently, Koopmans et. al.[4] reported measurements of SHG from C_{60} thin films in an ultra-high vacuum (UHV) environment. A study of the frequency dependence of the SH signal using fundamental light in the wavelength range of 774-620 nm showed resonant enhancement at 688nm ($2\hbar\omega$=3.6 eV). The film thickness dependence of the strong resonantly enhanced SH signal at $2\hbar\omega$= 3.6eV was measured in reflection geometry in order to determine its source. The SHG resonance was explained in terms of the h_g(second highest occupied molecular orbital)$\rightarrow$ h_u(HOMO)$\rightarrow$ t_{1u}(LUMO)$\rightarrow h_g$.excitation sequence of C_{60}. The SHG signal was found to be predominantly of bulk character and dominated by the magnetic dipole h_u-t_{1u} transition.

In our experiment, we measured SHG in both transmission and reflection geometry from C_{60} films deposited by sublimation in a UHV chamber. We then deduced the independent non vanishing surface and bulk nonlinear susceptibility elements of C_{60} films from the results. Using the simple model discussed in chapter 2, we could also successfully relate the surface nonlinear susceptibility elements to the nonlocal electric quadrupole and magnetic dipole nonlinear susceptibility elements of the C_{60} bulk. Our study differs from that of Koopmans et al[4] in that we used fundamental light at 1064 nm as the excitation source. Thus, the second

harmonic frequency ($2\hbar\omega$= 2.33eV) is on the tail of the electric-dipole allowed h_u-t_{1g} transition of C_{60} as well as near resonance with the electric-quadrupole allowed and vibration-assisted electric-dipole allowed h_u-t_{1u} transitions.

In the next section, we describe the experiment, the results, and the theoretical fits to the data. Next, we discuss the relative importance of surface and bulk contributions to the observed SHG, the microscopic understanding of the origin of the nonlinearity, and comparison with work of others.

Experiment

Figure 1 shows a schematic of the experimental setup. A Q-switched mode locked Nd:YAG laser was used as the source of the fundamental at 1064 nm. The energy per Q-switched pulse, which contained about 20 mode-locked pulses, each with a pulse width of 80 psec, was 1.2 mJ and the repetition rate was 500 Hz. The peak intensity at the sample was about 30 MW/cm^2, which was at least a factor 10 below the damage threshold. No laser induced changes of the C_{60} sample could be observed, even over six hours. We measured SHG from C_{60} films in-situ during their growth by evaporation on fused quartz substrates in a UHV chamber. The pressure in the chamber was kept below 2×10^{-9} mbar before evaporation and below 10^{-8} mbar during evaporation. The C_{60} powder, purchased from SES Research Inc., was placed in a Knudsen

cell at a distance of approximately 20 cm from the substrate and the evaporation temperature was about 450 °C. Prior to evaporation, the cell was kept at 200 °C for at least 12 hours in order to remove any residual solvent. Further, evaporation began only after the cell had been heated to about 450 °C for about 20 minutes as controlled by a flag between the cell and the substrate. The C_{60} evaporation typically lasted about 7 hours to obtain a film thickness of 1.5 μm. The substrate was kept at room temperature during the evaporation. Experiments with the substrate at a temperature of 200 °C were also carried out and similar results were obtained.

The angle of incidence of the 1064 nm input beam was 61°, which is close to the Brewster angle of C_{60} films. We simultaneously monitored the second harmonic intensity in four detection channels during the film growth. These corresponded to the two SH output polarizations s and p in both reflection and transmission. A half-wave plate in the input beam was used to set the input polarization, which was manually switched to p and m (denoting linear polarization at 45° from the plane of incidence) every 5 minutes and inbetween to s. In detecting the SH signal, color filters to block the fundamental beam from the detectors were used (Two-photon fluorescence from C_{60} was negligible). Gated integration was employed to reduce the background to about 50 counts per minute. The signal typically was between 100

and 20,000 counts per minute, depending on the input/output polarization combination. The relative detection efficiency of the four channels was determined prior to evaporation by placing a quartz crystal in the input beam. However, it was only accurate to about 30 % and was the main source of error in our deduction of nonlinear susceptibilities from the data. The overall calibration of the second harmonic efficiencies was done with respect to a quartz crystal at the sample position. We estimate the precision to be about 40 %.

A photodiode monitored the interference pattern of the linearly transmitted fundamental beam and the difference between the maxima and the minima of this interference pattern determined the refractive index of C_{60} at the fundamental frequency. The position of the peaks was used for thickness calibration. A quartz crystal microbalance was used to measure the thickness of the C_{60} film. Since the quartz crystal was somewhat displaced to the side from the sample and the angular evaporation profile was unknown, calibration of the quartz crystal microbalance was necessary. This was done by linking the frequency shift of the quartz oscillator to the interference pattern of the fundamental light in transmission. While the frequency shift of the quartz crystal responded very sensitively to the speed of evaporation at any given moment, the optical interference provided the overall calibration. The

refractive index of C_{60} at 532 nm was determined in an independent experiment by analyzing the linear interference pattern at 532 nm obtained during growth of a C_{60} film. Figure 3 displays these data together with the fit.

The experiment yielded 8 sets of data to be analyzed: s-in/p-out, p-in/p-out, mixed-in/s-out, and mixed-in/p-out in reflection and transmission. The polarization combinations s-in/s-out and p-in/s-out were also measured but gave zero SH-signal for reasons of symmetry. All data sets were obtained as functions of film thickness, which display complex interference patterns, resulting from superposition of the fundamental and the second harmonic interferences. Theoretical fits of the data allowed us to determine the non vanishing nonlinear susceptibilities.

Results

Figure 3 shows the experimental data (circles) together with the theoretical fit (lines) using the model with 7(6 surface and 1 bulk) nonlinear susceptibility elements as discussed in Section II. We were able to reduce the number of independent parameters in this fit from 7 to 5 (all bulk susceptibilites) by using Eq. 21. The best-fit susceptibilities are listed in Tables 1 and 2. The uncertainty of 40% for our fit parameters is dominated by uncertainties in the calibration of the relative detection

efficiencies of the different channels. While the theory reproduces most of the experimental data, the fit for some polarization combinations at low film thickness is poor. This is particularly true for s-in/p-out, where presumably only effective surface nonlinear susceptibility elements $\chi_{s,zyy}(q/f) - \gamma$ and $\chi_{s,zyy}(v/f) + \gamma$ should contribute to SHG. One may think that the film characteristics could have changed during the initial period of film growth. As seen in Fig. 3, no anomaly in the linear optical properties of the film in the low thickness regime has been observed. However, SHG is generally far more sensitive to the surface properties than linear optic effects. The anomalous behavior of SHG at low film thickness could still be connected to the surface anomaly. We realize that surface roughness in the thin film limit could be the source of trouble. For example, for a flat surface or interface of C_{60}, $\chi_{s,zzz}$ does not contribute to SHG with the s-in/p-out polarization combination. This is no longer true if the surface is rough as the local surface normal can then be tilted away from z. It is believed that the film growth of C_{60} deposited on a fused quartz substrate starts from islands that later merge and form a continuous film. This is confirmed by Figure 5, which displays a typical atomic force microscopy picture for a 1.5 μm C_{60} film, in which one observes domains with a size of a couple of thousand Å. The vertical scale of the thickness variations is about 100 Å. Looking at the shape of the domains, we can conclude that

the growth of the film must have started with formation of clusters of a roughly spheroidal shape. Thus, in the early phase of the film growth one has to consider the C_{60} film as an assembly of clusters instead of a smooth uniform film. Second harmonic generation from such a film certainly cannot be described by the theoretical formulation for smooth films discussed in the previous section unless for some particular polarization combinations such as p-in/p-out, the process is insensitive to the film roughness. Also, because the film roughness depends critically on nucleation, SHG in the early phase of the film growth is expected to be less reproducible than the later phase when the film is smoothed out, as we have indeed observed. The film quality should improve as the film grows in thickness. We expect that the theoretical description of SHG from a smooth film should be a reasonable approximation for a film thickness greater than a few thousand Å. Therefore, in fitting the experimental data in Fig. 4, we have excluded points with thicknesses less than 6000 Å in the fitting procedure. Also, we have made the reasonable assumption that the relative phases of the $\chi^{(2)}$ elements are zero.

The thickness dependence of the SHG for the different polarization combinations depends on the angle of incidence of the input fundamental as well as the linear optical properties of the C_{60} film. Because the angle of the input beam is near the brewster angle of the C_{60}- vacuum

interface, the p-in/ p-out SHG signal in transmission shows almost no interference pattern while the s-in/p-out signal shows an interference pattern mainly from the s-polarized fundamental. All of the transmission SHG data clearly show a long wavelength interference pattern, which is the first Maker fringe associated with phase matching of SHG in C_{60}. To optimize the theoretical fit to the data, it was necessary to slightly adjust the indices of refraction of the film. We find $n_\omega = 1.98$ and $n_{2\omega} = 2.3 + i.087$, which is within the variation measured for different films.

Discussion

Figure 4 shows that the model fits the data reasonably well for thicknesses greater than 6000 Å. We first discuss the results in terms of the 7 (6 surface and 1 bulk) parameters. From the fitted nonlinear susceptibilities, we can conclude that the separable bulk term δ' and the two surface susceptibilities $\chi^{(2)}_{s,yzy}(q/f)$ and $\chi^{(2)}_{s,yzy}(f/v)$ contribute significantly to the observed SHG. Setting $\delta'=0$ or setting $\chi^{(2)}_{s,yzy}(q/f) = \chi^{(2)}_{s,yzy}(f/v) = 0$ makes the theoretical fit with the experimental data very poor, especially for the mixed-in/s-out case. The surface susceptibilities $\chi^{(2)}_{s,zyy}(q/f)$, $\chi^{(2)}_{s,zyy}(f/v)$, χ

$\chi^{(2)}_{s,zzz}(q/f)$, and $\chi^{(2)}_{s,zzz}(f/v)$ also contribute significantly to the SHG, as can be seen from the following argument. If the just mentioned surface susceptibilities are negligible, then the nonlinear parameters in the first four rows of table 2 would be equal in magnitude but the values in rows 2 and 4 and rows 1 and 3 would have the opposite sign. Any deviation from these relationships must be due to contributions from the surface susceptibilities. For the quartz film interface we subtract $\chi^{(2)}_{s,zyy}(q/f) - \gamma$ from $\chi^{(2)}_{s,zzz}(q/f) - \gamma$ and obtain $\chi^{(2)}_{s,zzz}(q/f) - \chi^{(2)}_{s,zyy}(q/f) = 16.7 \times 10^{-15}$ esu. This quantity is independent of the bulk term γ and is comparable in magnitude to both $\chi^{(2)}_{s,zyy}(q/f) - \gamma$ and $\chi^{(2)}_{s,zzz}(q/f) - \gamma$, indicating that either $\chi^{(2)}_{s,zzz}(q/f)$ or $\chi^{(2)}_{s,zyy}(q/f)$ or both contribute significantly to the SH response. A similar argument can be made for the film-vacuum interface susceptibilities. Note that nothing can be said about the importance of γ. From our 7-parameter fit we conclude that both surface susceptibilities and bulk δ' contributions are important for SHG from the C_{60} film and therefore neither can be neglected in our interpretation. Our results are consistent with previous SHG results on C_{60} films, although the latter are not so complete or exhibit only a special case of our results. Wang et al [2], who also worked at 1064 nm, found a significant surface contribution by linear extrapolation to zero of SHG data taken at several thicknesses below 0.3 μm. However, they did not obtain the necessary thickness

dependence with different polarization combinations to separate the surface and bulk contributions. A careful thickness dependent measurement was performed at the fundamental frequency of 1.81 eV[4]. In this case, a bulk magnetic-dipole resonance at the fundamental dominated the SH signal such that the surface contribution could be neglected.

As determined from Eq. 21, the 5-parameter model, using bulk susceptibilities $\tilde{\chi}^{P}$ and $\tilde{\chi}^{Q}$ to describe both bulk and surface contributions, are displayed in Table 3 along with the bulk parameters β, γ, δ, and δ', deduced by their relations given in Eq. (15). To understand the microscopic origin of these susceptibilities, we need to consider the optical absorption spectrum of C_{60}, shown in Fig. 6 [5]. On this figure, we have marked the wavelength of the SH frequency used in our experiment. While the fundamental is not close to any absorption features, the SH frequency appears on the long wavelength tail of the peak centered at 442 nm (2.80 eV). The most reasonable assignment for this 442 nm peak is the lowest-energy h_u-t_{1g} electric dipole (ED) transition of C_{60} shown in Fig. 7, along with the next higher energy electric dipole transition of (g_g+h_g) - t_{1u} at 346 nm (3.58 eV). The energy levels are labeled according to the icosahedral symmetry group. Since C_{60} is weakly interacting, we assume that this isolated molecule picture is still reasonable for the interpretation of the optical spectrum of the solid C_{60}

film. The electronic transitions across the HOMO-LUMO(h_u-t_{1u}) gap(see Fig. 7) are ED forbidden. However, coupling of the h_u or t_{1u} states to the vibrational modes of C_{60} of the proper symmetry can lead to vibration-assisted ED transitions from h_u to t_{1u}. These transitions have been observed from solutions of C_{60} in hexane[6]. They appear as a series of very weak peaks centered about 540 nm and spread over a width of about 100 nm and the intensity of each peak is about an order of magnitude less than the ED-allowed h_u-t_{1g} transition. For solid C_{60}, we expect the transitions to be 'hidden' in the long wavelength tail of the 442 nm h_u-t_{1g} peak. For reasons which will be discussed shortly, we also need to consider those transitions across the HOMO-LUMO gap of C_{60} which are only electric quadrupole (EQ) and magnetic dipole (MD) allowed. In Fig. 8, we show the electronic energy level diagram of C_{60} with electron interactions taken into account; the excited levels arise from one electron being promoted from the h_u orbital to the t_{1u} orbital and are split into T_{1g}, T_{2g}, G_g, and H_g multiplets by symmetry [7]. Calculations [7] suggest that they are ordered as shown in Fig. 8, with the $^1A_{1g}$ - ^1H_g transitions about 0.5 eV higher than the $^1A_{1g}$ - $^1T_{1g}$ transitions. The excitation from the ground level $^1A_{1g}$ to the excited level $^1T_{1g}$ is MD allowed and to the ^1H_g symmetry is EQ allowed. Excitations from $^1A_{1g}$ to ^1G_g and $^1T_{2g}$ symmetry are neither MD nor EQ allowed. There is experimental evidence indicating that the $^1A_{1g}$ to T_{1g} MD

transition is at 1.81 eV [4]. Therefore, we assign the energy of the $^1T_{1g}$ level to be at 1.81 eV and accordingly, the ^1H_g level at about 2.3 eV in Fig. 8. We now have a complete picture of the low energy optical transitions in C_{60} that are important to our SHG experiment. While the SHG process is non-resonant in the input field at 1.17 eV, resonant enhancement by transitions of ED and EQ symmetry can occur in the output field at 2.33 eV. To understand in more detail how these transitions contribute we need to recall the microscopic expressions of both $\tilde{\chi}^P$ and $\tilde{\chi}^Q$ bulk susceptibilities. The $\tilde{\chi}^Q$ contribution is given by the microscopic expression with ED matrix elements at the input frequency and an EQ matrix element at the SH frequency. Therefore, we expect that the EQ transition from $^1A_{1g}$ to $^1H_{1g}$ at about 2.3 eV will enhance the $\tilde{\chi}^Q$ susceptibility. The $\tilde{\chi}^P$ susceptibility consists of an EQ and/or MD matrix element, an ED matrix element at the input frequency and an ED matrix element at the SH frequency. If $\tilde{\chi}^P$ is dominated by EQ (or MD) transitions in the input field, then the additional relations $\chi_3^P = \chi_4^P$ (or $\chi_3^P = -\chi_4^P, \chi_2^P = 0$) should apply. From our results, displayed in Table 3, we find that none of these relations are applicable and EQ and MD transitions at the input field contribute equally to $\tilde{\chi}^P$. This result is not surprising because the input field at $\hbar\omega$ =1.17 eV is far from both the $^1A_{1g}$ to $^1T_{1g}$ MD and $^1A_{1g}$ to $^1H_{1g}$ EQ transition energies. However, the ED transition at 2.80 eV and the vibration-assisted ED transitions of h_u-t_{1u}

can resonantly enhance $\tilde{\chi}^P$. Additionally, we find that $\tilde{\chi}^P$ and $\tilde{\chi}^Q$ are of similar order of magnitude, which indicates that processes involving the EQ transition in the output field are about as strong as processes involving the ED allowed transitions in the output field.

At this point it is very interesting to compare our results with the results of Koopmans et. al. [4]. They performed a similar experiment with the only difference being that they worked at a frequency of $2\hbar\omega$ = 3.6 eV. They find that their SH signal is resonantly enhanced with the input field in resonance with the $^1A_{1g}$ to $^1T_{1g}$ MD transition at 1.81 eV and the output SH field in resonance with the h_g-t_{1u} ED transition at 3.56 eV. They obtain $\chi_3^P \approx 1.35 \times 10^{-13}$ esu. Since the process is doubly resonant, it is not surprising to see their value higher than ours by more than an order of magnitude. Also, for this double resonance case, the experiment is adequately described by χ^P only (with $\chi^Q \cong 0$). Furthermore, with the input field at resonance with a MD transition, one gets $\chi_3^P = -\chi_4^P$, $\chi_1^P = \chi_2^P = 0$. In this case, there is no contribution to the surface susceptibility through the bulk susceptibilities $\tilde{\chi}^P$ and $\tilde{\chi}^Q$, as can be seen from Eq. [21] of Chapter 2. Therefore, in their experiment, the surface contributions to SHG can be neglected. In our experiment, however, EQ and ED transitions play a more important role and hence we find $\tilde{\chi}^P$ and $\tilde{\chi}^Q$ are comparable and non vanishing. This also means that surface contributions

are as important as the bulk contributions. Though the results of the two experiments at first glance look quite different, they are fully consistent with each other.

Conclusion

We have measured, using Q-switched mode-locked Nd:YAG laser pulses, the second harmonic signal at 2.33 eV from C_{60} films during growth. Analyzing the full thickness dependence in four different polarization combinations in reflection as well as in transmission, we could deduce surface and bulk contributions to the observed SHG. Both are non-negligible and can be adequately described in terms of the nonlocal bulk susceptibility tensors $\tilde{\chi}^{P}$ and $\tilde{\chi}^{Q}$, which constitute five independent nonlinear susceptibilities in the isotropic film. We find that all five susceptibilities are of the order of 10^{-15} esu. We suggest that $\tilde{\chi}^{Q}$ is singly resonant at the SH frequency ($2\hbar\omega$=2.33 eV) with the $^{1}A_{1g}$ to $^{1}H_{1g}$ EQ transition in the h_u-t_{1u} (HOMO-LUMO) manifold and that $\tilde{\chi}^{P}$ is singly resonant at 2.33 eV with the broad h_u - t_{1g} ED transition at 2.8 eV and vibration-assisted h_u - t_{1u} ED transitions. Our results are very different from that of Koopmans et al, where the input field is resonant with the $^{1}A_{1g}$ to $^{1}T_{1g}$ magnetic dipole (MD) transition at 1.81 eV in the h_u-t_{1u} manifold the SH field is resonant with the (g_g +

h_g) -t_{1u} ED transition at 3.56 eV. In the latter case, the process is doubly resonant, and with the input MD resonance, can be adequately described by $\tilde{\chi}^P$ only (with $\tilde{\chi}^Q \approx 0$). Because of the double resonance, it is not surprising that the susceptibilities they found are more than an order of magnitude larger than our susceptibilities.

References

1. H. Hoshi, N. Nakamura, Y. Maruyama, T. Nakagawa, S. Suzuki, H. Shiromaru, Y. Achiba, Jpn. J. Appl. Physics, Part 2 - Letters **30**, : L1397 (1991).

2. X. K. Wang, T. G. Zhang, W. P. Lin, S. Z. Liu, G. K. Wong, M. M. Kappes, R. P. H. Chang, and J. B. Ketterson, Appl. Phys. Lett. **60**, (7), 810 (1992).

3. J. Sipe, V. Mizrahi, G. Stegeman, Phys. Rev. B **35**, 9091 (1987).

4. B. Koopmans, A. M. Janner, H. T. Jonkman, G. A. Sawatzky, and F. van der Woude, Phys. Rev. Lett. **71** ,3569 (1993).

5. A. F. Hebard, R. C. Haddon, R. M. Fleming, and A. R. Kortan, Appl. Phys. Lett. **59**, 2109 (1991).

6. S. Leach, et. al., J. Chem. Phys. **160**, 451 (1992).

7. F. Negri, G. Orlandi, F. Zerbetto, Chem. Phys. Lett. **144**, 31 (1988).

Figure Captions

Fig. (1)

A schematic outline of the experimental setup that measures simultaneously transmitted and reflected SHG from a C_{60} film in four different detection channels. Pol: Polarizer, $\lambda/2$ plate: half wave plate, S: Substrate, QCM: Quartz crystal micro balance, PBS: Rochon Polarizer beam separator, M: Mirror, F: Filter, PMT: Photomultiplier tube, P:Prism, DBP: Dichroic beam separator, PD: Photodiode.

Fig. (2)

SHG versus film thickness from a C_{60} film grown at room temperature. The lines are the theoretical fit to the experimental data (circles). (a) fundamental input s-polarized and reflected SH output p-polarized (b) fundamental input s-polarized and transmitted SH output p-polarized (c) fundamental input p-polarized and reflected SH output p-polarized (open circles) fundamental input p-polarized and transmitted SH output p-polarized (solid circles) (d) fundamental input mixed-polarized and reflected SH output s-polarized (e) fundamental input mixed-polarized and transmitted SH output s-polarized (f) fundamental input mixed-polarized and reflected SH output p-

polarized (g) fundamental input mixed-polarized and transmitted SH output p-polarized. The fit parameters are listed in table 2 and table 3.

Fig. (3)

Thickness dependent linear interferences at 532 nm in reflection and transmission. Data (circles), theory (lines) (a) s-polarized reflection, (b) s-polarized transmission, (c) p-polarized reflection, (d) p-polarized transmission. The theoretical fit allows the determination of the refractive index $n(2\omega) = 2.3 + i\ 0.13$.

Fig. (4)

An Atomic Force Microscope picture of the surface of a 1.2 μm C_{60} film. The domains are a couple of thousand Å in diameter. The vertical distance between the bright and the dark areas is about

100 Å.

Fig, (5)

Linear absorption spectra of a 98 nm thick C_{60} film in the visible wavelength region after Ref. 22. The arrow indicates the second-harmonic wavelength in the experiment.

Fig. (6)

Energy level diagram for the isolated C_{60} molecule near the fermi energy. The two lowest energy electric dipole allowed transitions at 2.80 eV and 3.58 eV shown by the arrows correspond to the features at 442 nm and 346 nm in Figure 7, respectively.

Fig. (7)

Energy level diagrams of molecular C_{60} near the HOMO-LUMO (h_u-t_{1u}) transitions of C_{60}. (a) Single electron level diagram, and (b) Multi-electron level diagram.

Tables

Table 1

Best Fit Parameters for 7 Parameter Model for SHG at λ =1.064 μm from a C_{60} film

Nonlinear Susceptibility Component	Susceptibility (10^{-15} esu)
$\chi_{s,zzz}(q/f)-\gamma$	22.8
$\chi_{s,zzz}(f/v)+\gamma$	-41.7
$\chi_{s,zyy}(q/f)-\gamma$	6.1
$\chi_{s,zyy}(f/v)+\gamma$	-2.9
$\chi_{s,yzy}(q/f)$	3.9
$\chi_{s,yzy}(f/v)$	-4.3
δ'	10.0

Table 2

Best fit Bulk Susceptibilities ($\tilde{\chi}^P$,$\tilde{\chi}^Q$) and 4 dependent Susceptibilities (δ, β, γ, δ')

for SHG at λ=1.064 μm from a C_{60} film

Bulk Susceptibility Component	Susceptibility (10^{-15} esu)
χ_2^P	-1.3
χ_3^P	-9.2
χ_4^P	1.7
χ_2^Q	5.9

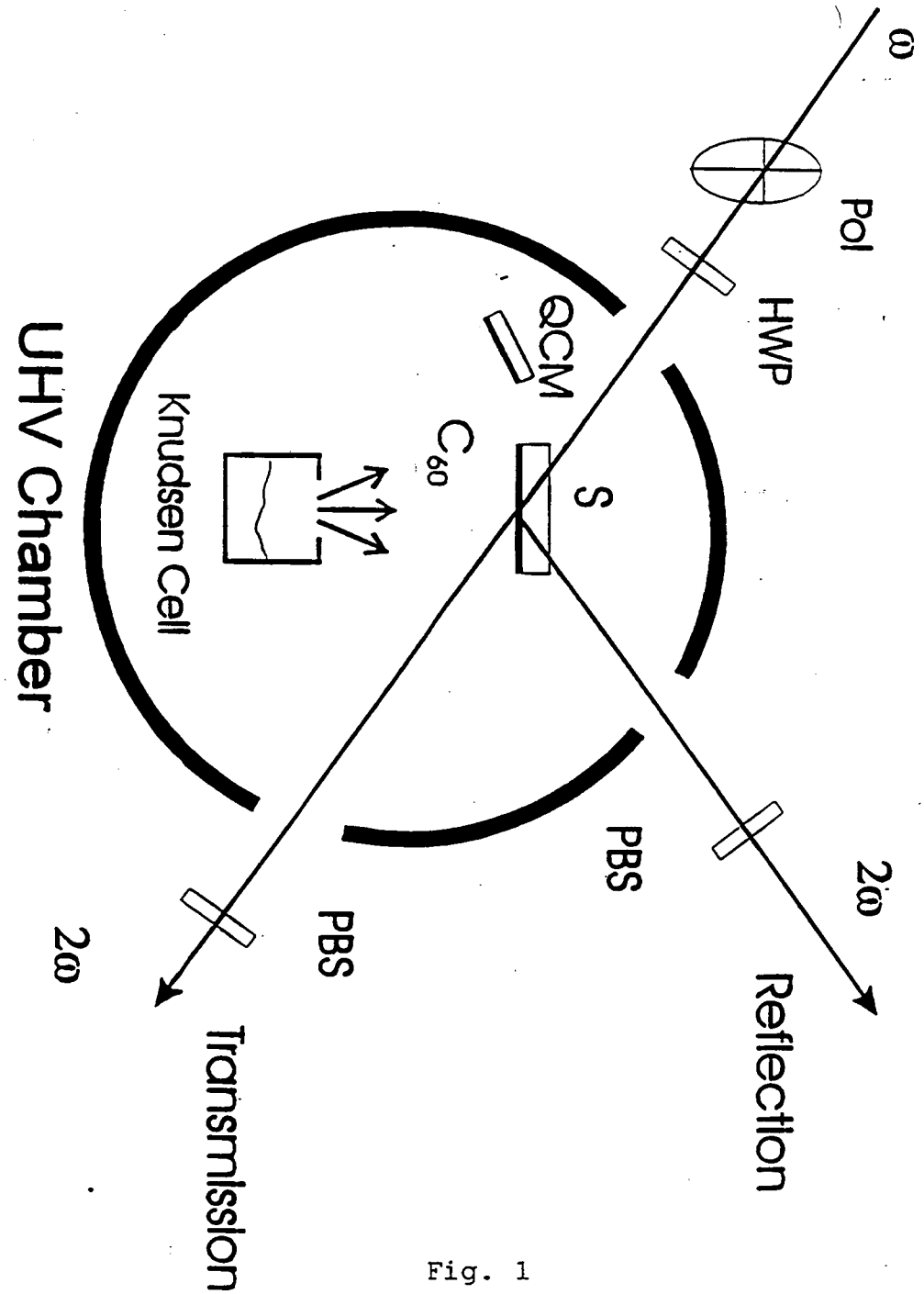
ω
Pol
HWP
QCM
Knudsen Cell
C60
S
UHV Chamber
PBS
PBS
2ω
2ω
Reflection
Transmission

Fig. 1

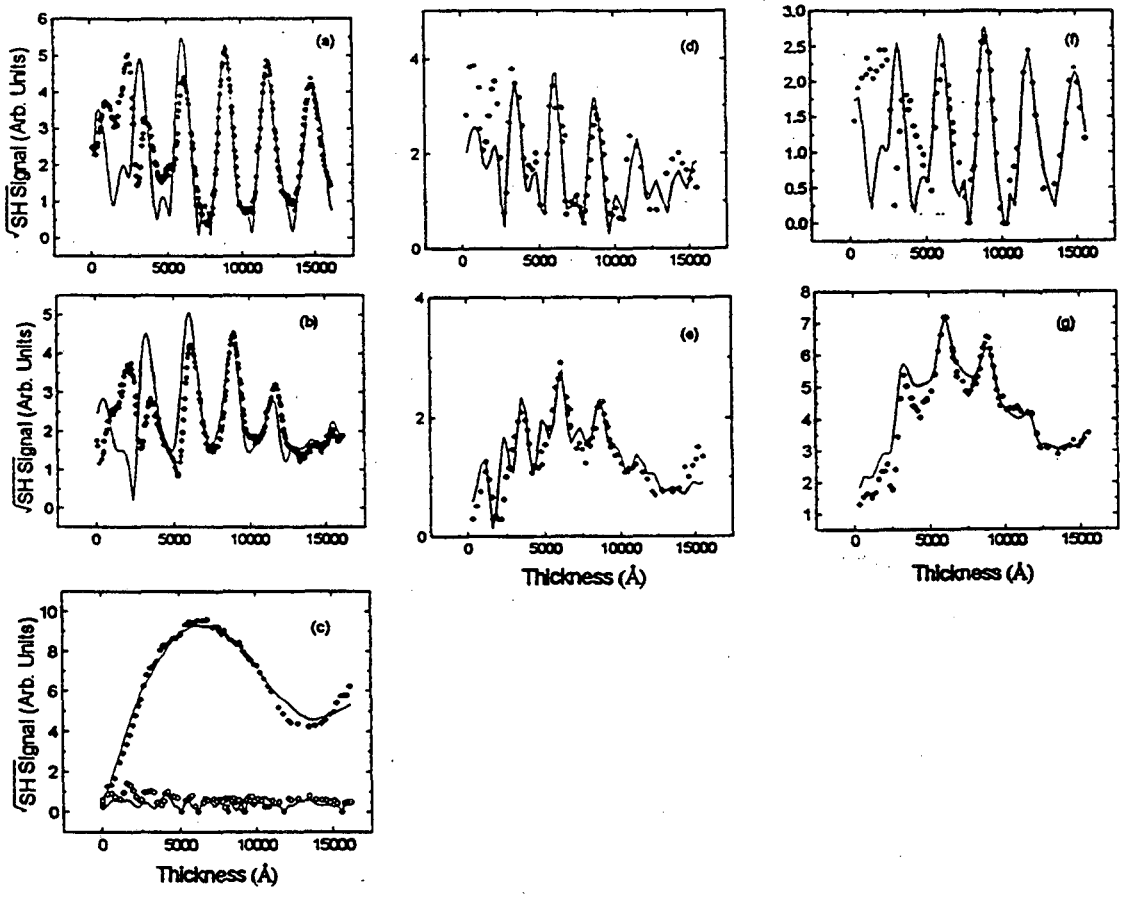

Fig. 2

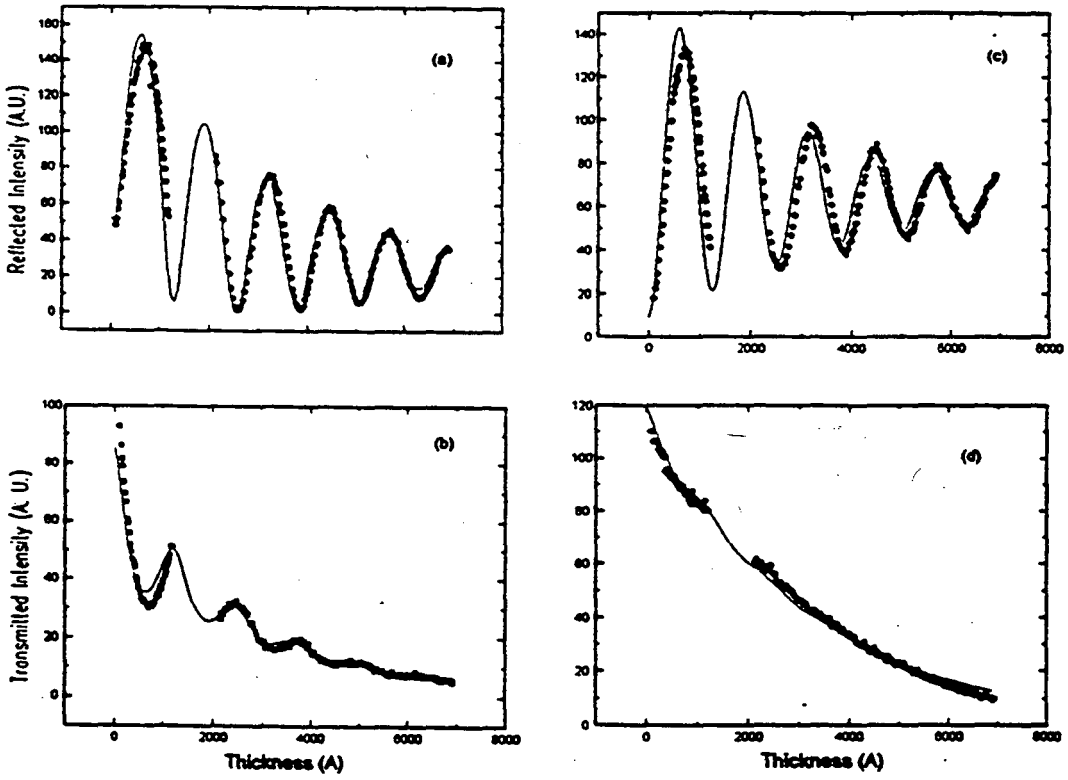
(a)
(c)
(b)
(d)
Reflected Intensity (A.U.)
Transmitted Intensity (A.U.)
Thickness (A)
Thickness (A)

Fig. 3

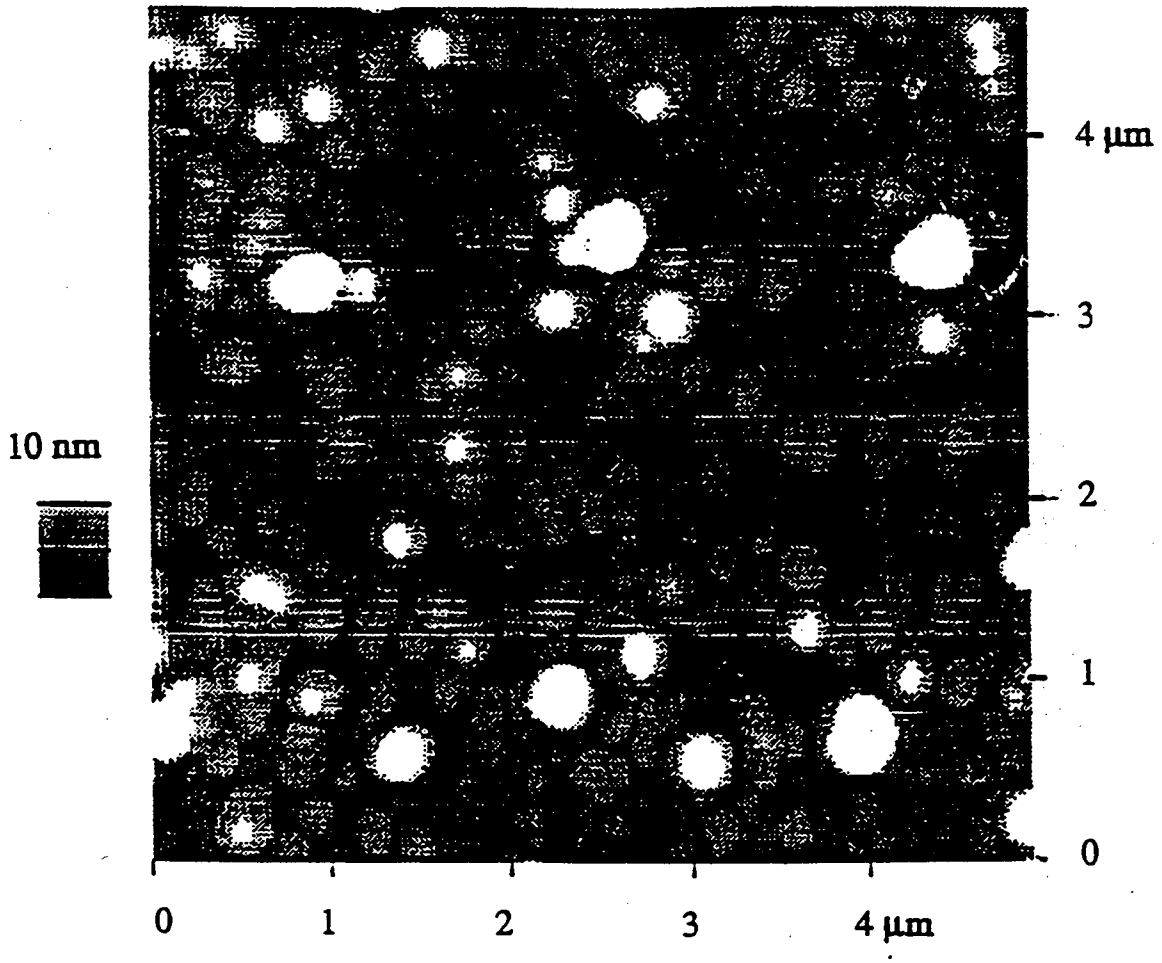

Fig. 4

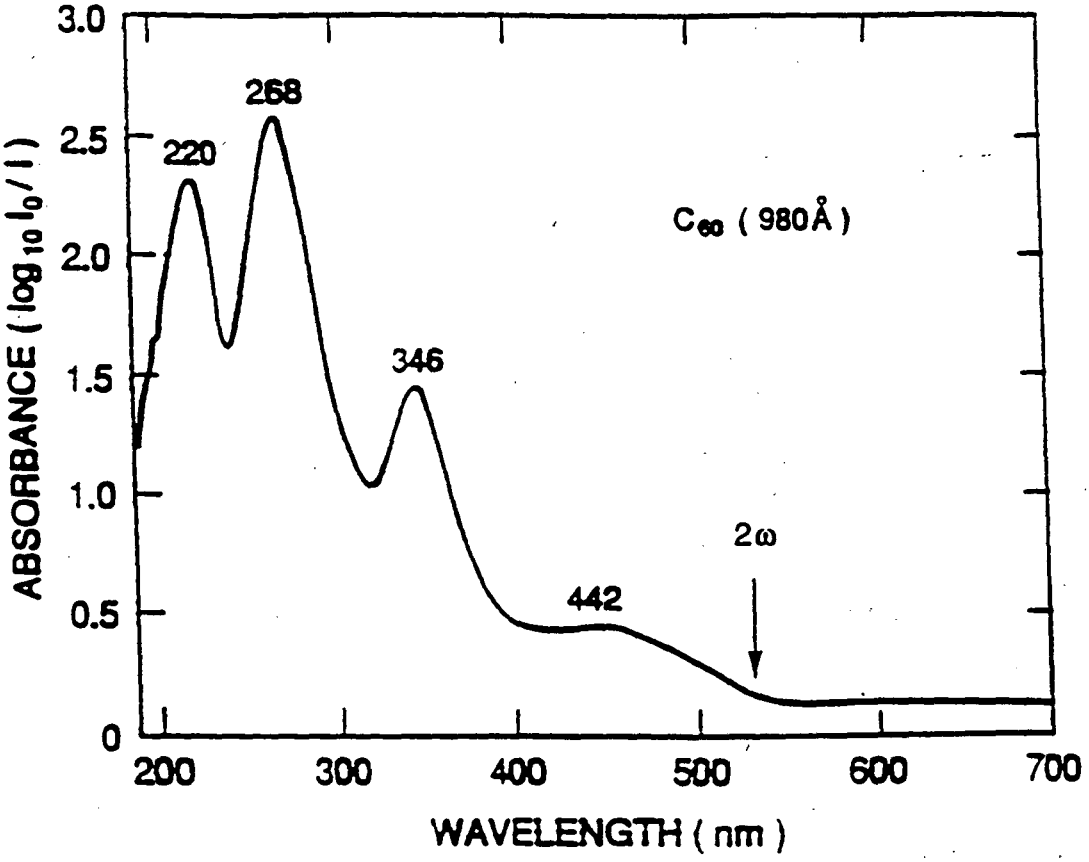
3.0
2.5
2.0
1.5
1.0
0.5
0
ABSORBANCE ($\log_{10} I_0/I$)
220
268
346
442
2ω
C_{60} (980Å)
200
300
400
500
600
700
WAVELENGTH (nm)

Fig. 5

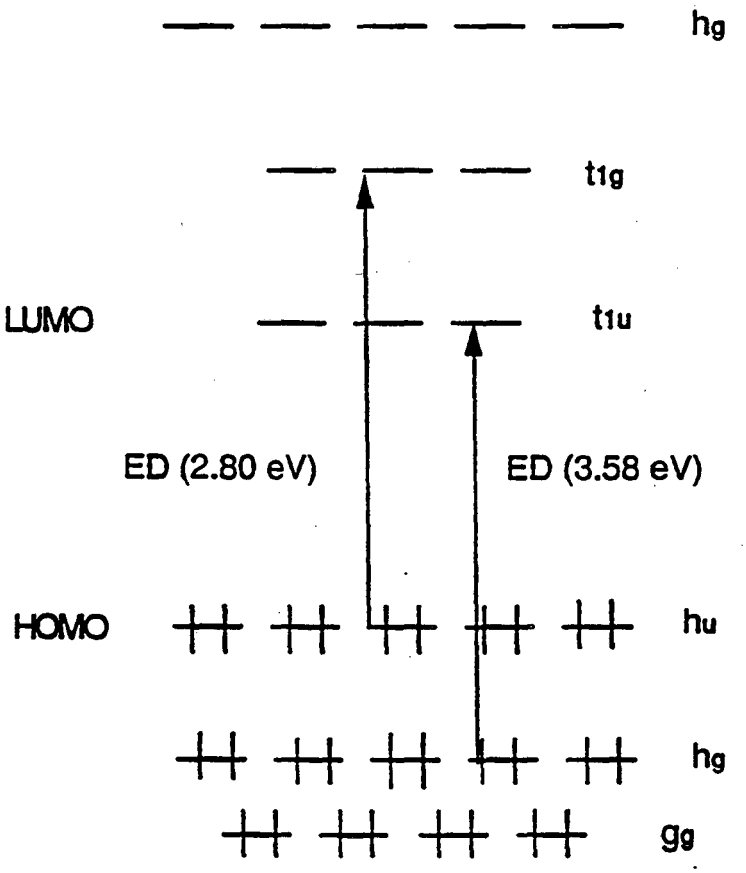

Fig. 6

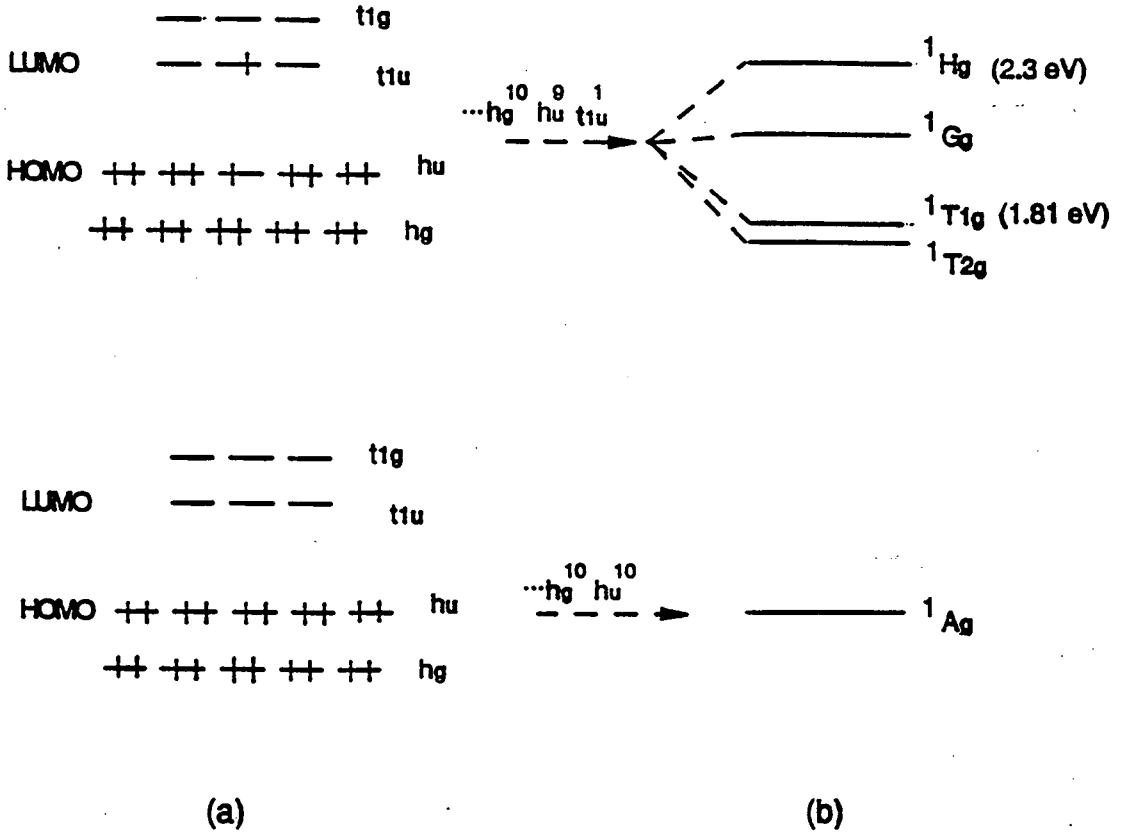
t1g
LUMO
t1u
HOMO
hu
hg
···hg10 hu9 t1u1
1Hg (2.3 eV)
1Gg
1T1g (1.81 eV)
1T2g
t1g
LUMO
t1u
HOMO
hu
hg
···hg10 hu10
1Ag
(a)
(b)

Fig. 7

V. Tunable SHG and SFG from C60 Thin Films

Introduction and Background

The results discussed in chapters 3 and 4 suggest that further studies of the ^1A_g to ^1H_g EQ and ^1A_g to $^1T_{1g}$ MD transitions of C_{60} using nonlinear optical spectroscopy could be very interesting. Our results and the results of others[1] indicate that the ^1A_g to $^1T_{1g}$ MD transition is around 1.8 eV while the ^1A_g to ^1H_g EQ transition could be around 2.33 eV. Tunable Sum Frequency Generation (SFG) with $\hbar\omega_S$ ($\omega_S=\omega_1+\omega_2$) ranging from 2.0 to 2.5 eV could be performed to locate the center of this EQ transition. In this case $\vec{\chi}^Q$ will be resonantly enhanced by the EQ transition, but $\vec{\chi}^P$ will not and will only contribute to the non-resonant background. Alternatively, one could use a single input beam with $\hbar\omega$ ranging from 2.0 to 2.5 eV, in which case the input field at $\hbar\omega$ would be resonant with the EQ transition while the output field at $2\hbar\omega$ would be resonant with the high-lying ED transition at 4.6 eV (See Fig. 4, Ch. 4). This double resonance then make $\vec{\chi}^P >> \vec{\chi}^Q$ and $\vec{\chi}^M$. However, in this case, the input beam frequency lies in a region of significant linear absorption (See Fig. 5, Ch. 4), and the C_{60} film is easily damaged at the minimum intensity required to generate a detectable SH signal.

The ^1A_g to ^1T_g MD transition at 1.81 eV could be further investigated by SHG at $2\hbar\omega$= 1.81 eV and by sum frequency

generation (SFG) at $\hbar(\omega_1+\omega_2)$ = 1.81 eV. However, SHG is not allowed by the MD transition at 2ω due to isotropy and time reversal symmetry [2]. However, if $\omega_1 \neq \omega_2$, the SF signal is resonantly enhanced when $\omega_s=\omega_1+\omega_2$ equals the MD transition frequency. In addition, the beams at ω_1 and ω_2 must be noncollinear, as was shown in Chapter 3. To observe this effect, one can use two frequency-tunable sources, with $\hbar(\omega_1+\omega_2)$ fixed at 1.81 eV, but ω_1 and ω_2 varied relatively. As long as $\omega_1 \neq \omega_2$, one should be able to observe the resonant enhancement. Alternatively, one could perform the experiment by keeping ω_1 fixed and varying ω_2 such that $\omega_1 + \omega_2$ passes though the MD resonance at 1.81 eV. The latter method will be used in our experiment.

To perform the above mentioned experiments, we require a tunable, high intensity source. The optical parametric oscillator (OPO), using LBO as a the nonlinear medium, is an ideal source for these experiments and is discussed in the following section.

Optical Parametric Oscillator

Introduction and Background

Optical parametric oscillators (OPO) have been recognized for many years as potentially useful tunable coherent optical sources because of their broad tuning range and high conversion efficiency along with ease of operation[3]. The recent emergence of nonlinear crystals such as β-BaB_2O_4

(BBO), LiB_3O_5 (LBO) [4] and $KTiOPO_4$ (KTP) nonlinear crystals have made these devices a practical reality. Of them LBO is particularly convenient because of temperature tunability, which yields non critical phase matching for the parametric process over a wide frequency range. The non critical phase matching significantly increases the acceptance angle and reduces the beam walk-off. Successful operation of OPO with LBO has been reported by other authors [5,6]. Recently, picosecond OPOs using BBO and LBO have become commercially available.

The schematic of the typical OPO, shown in Fig. 1, consists of a resonant cavity, which may have highly reflective mirrors at both or either of the signal and/or idler frequencies of the OPO, and a nonlinear medium in which the amplification process occurs. The cavity is pumped from one or both sides by a high power, coherent source (usually a laser) which may be properly focused into the cavity so as to overlap with the allowed cavity modes. Energy conservation requires that $\omega_p = \omega_i + \omega_s$, where ω_p is the pump frequency, ω_s is the signal frequency, and ω_i is the idler frequency. Ideally, 100% conversion from the pump to the signal and idler is possible, however absorption and scattering losses prevent this ideal situation from occurring.

The effective operation of the OPO depends on a high nonlinear second order polarizability described by χ_{ijk} in

the optical transparency range of the crystal such that it is independent of the optical frequency. In addition to the high nonlinearity, the coherence condition requires phase matching between the signal, idler, and pump waves, which is given by $\vec{k}_p = \vec{k}_s + \vec{k}_i$. To meet this condition requires control of the indices of refraction that is accomplished by the angular dependence of the birefringence and also by the temperature variation. Using these techniques one can obtain a coherent, high intensity optical source with a tuning range from the UV to IR.

In the case of the OPO we start out with a high intensity pump wave and generate both signal and idler waves from noise. Additionally, we assume that the amplitude of the pump wave does not change as the pump wave passes through nonlinear medium. In this approximation the intensity of the signal and idler waves increase exponentially with the propagation distance z in the nonlinear medium. Combining this result with the oscillation condition of the OPO cavity, one can obtain the threshold pump intensity for oscillation. In general there are two cases to consider when determining the OPO oscillation threshold. First, one can have a doubly resonant oscillator (DRO) or a singly resonant oscillator (SRO). In the case of the DRO, the oscillator is resonant at both the signal and idler frequencies and the SRO is resonant at either the signal frequency or idler frequency. As expected, the oscillation

threshold for the DRO is significantly lower that the threshold for the SRO. It therefore seems more desirable to operate the OPO as a DRO. However, the cavity stability requirements are very stringent for the DRO and so it is difficult to keep the amplitude and frequency of the DRO stable. Therefore, the SRO oscillator is more popular and easier to use.

Temperature Tuned LBO OPO

For our experiment, we use a singly-resonant temperature tuned OPO (shown schematically in Fig. 2), in which the temperature-tuned LBO crystal is synchronously pumped by 600 mW (average power) of 532 nm radiation. The 532 nm light is the frequency-doubled output from a Quantronix CW-pumped Q-switched and 100 MHz mode-locked Nd:YAG laser operating at 500 Hz. The OPO cavity consists of two concave HR mirrors with reflectivities > 97% from 650 nm to 1000 nm and radii of curvature of 30 cm , a flat output coupler with 70% reflectivity, and a diffraction grating ,which serves to narrow the linewidth of the OPO and serves as a broad band high reflector. The temperature tuned LBO crystal is located midway between the two concave HR mirrors and the overall optical path length of 150 cm is matched to that of the Nd:YAG pump laser. The tunable range of the OPO (signal plus idler) is from 650 nm to about 2500 nm. For single mode Gaussian TEM 00 operation of the oscillator, the beam size is about 180 μm in diameter at the center of the

LBO crystal. The pump beam is focused into the cavity in order match this cavity mode and therefore maximize the conversion efficiency. With a green pump beam average power of about 600 mW one obtains a signal average power of about 200mW and an idler output of about 100 mW.

Proposed Experiment

The proposed experiment for probing the bulk EQ and MD transitions of the C_{60} film is outlined schematically in Fig. 3, where the two noncollinear beams of frequency ω_1 and ω_2 are overlapped onto the C_{60} film. The film is prepared in a UHV chamber as described in the experimental section of Chapter 4. The beam at ω_1 is 400 mW of 1064 nm light from the Nd:YAG laser, which is separated from 600 mW at 532 nm by the harmonic beam splitter located just after the LBO Second-Harmonic generating crystal (See Fig. 3). The beam at ω_2 is the tunable beam of about 200 mW from the OPO signal or idler beam. The wavelength of the signal beam varies from 650 nm to about 1000 nm and the idler beam varies from 1000 nm to 2900 nm. In combination with the fixed wavelength 1064 nm beam, the signal and idler can be used to probe the EQ and MD transitions of C_{60}, respectively. Due to physical restrictions in our experiment, the maximum angle of incidence for each beam

with respect to the film surface normal is about 8°, leading to a 4° angle of incidence inside the thin film, due to refraction at the film-vacuum interface. In this geometry the direction of the nearly phase-matched output sum frequency beam is approximately normal to the film surface and varies only a few degrees within 1.2 eV of the expected resonances at 1.8 and 2.3 eV.

Now, the bulk sum-frequency electric field inside the film is given by[7]

$$\vec{E}_{\perp}(\omega_1+\omega_2) = -\frac{4\pi\vec{P}_{\perp}(\omega_1+\omega_2)}{(\varepsilon_S(\omega_1+\omega_2)-\varepsilon_3(\omega_3))}\left(e^{i\Delta kz}-1\right) \qquad [1]$$

$$\vec{E}_{\parallel}(\omega_1+\omega_2) = -\frac{4\pi\vec{P}_{\parallel}(\omega_1+\omega_2)}{\varepsilon_3(\omega_3)}\left(e^{i\Delta kz}-1\right)$$

where $\vec{P}_{\perp}(\omega_1+\omega_2)$, $\vec{P}_{\parallel}(\omega_1+\omega_2)$ are given by Eqn. 7 in chapter 3 (for the EQ case) or Eqn. 8 in chapter 3 (for the MD case). By controlling the thickness of the C_{60} film we can make $\Delta kz_{opt}=\pi$ and therefore maximize the transmitted output SF field. For the EQ case, we have $\varepsilon(\lambda_1\cong\lambda_2=1064nm)=4.0$, $\varepsilon(\lambda_3=532nm)=5.29$ and input beam angles of about 4°, so $z_{opt}=873nm$. Assuming $\chi_2^{Q} \cong \chi_3^{Q}$ we find

$$\frac{\vec{E}_{\parallel}(\omega_1+\omega_2)}{\vec{E}_{\perp}(\omega_1+\omega_2)} \approx 4$$

We can set up the detection system using an iris such that only a 0.5° aperture about $\vec{k}_s$ is observed. Therefore, $\vec{E}_{\parallel}(\omega_1+\omega_2)$ by the factor sin(0.5°)=0.0087 and $\vec{E}_{\parallel}(\omega_1+\omega_2) \ll \vec{E}_{\perp}(\omega_1+\omega_2)$, allowing one to neglect the contribution from χ_2^Q. The resultant transmitted SF intensity given in photons per pulse is [7]

$$I^{EQ}(\omega_1+\omega_2)=\frac{2\pi\omega_s^2}{c\sqrt{\varepsilon(\omega_s)}}\left|\bar{P}_{\perp}^{EQ}(\omega_1+\omega_2)\right|^2\left(\frac{\pi}{\Delta k}\right)^2 \qquad [2]$$

Using Eqn. 7 of Ch. 3 and the intensity $I(\omega_i)=\frac{c\sqrt{\varepsilon(\omega_i)}}{2\pi}\left|E(\omega_i)\right|^2$ Eqn. 2 becomes

$$I^{EQ}(\omega_1+\omega_2)=\frac{8\pi^2\omega_s^2}{c^3\sqrt{\varepsilon(\omega_1)\varepsilon(\omega_2)\varepsilon(\omega_s)}}\left|\chi_3^Q \mathrm{k}_s(\omega_1+\omega_2)[\sin(\alpha)\cos(\beta)\sin(\theta_2)-\sin(\beta)\cos(\alpha)\sin(\theta_1)]\right|^2 \left(\frac{\pi}{\Delta k}\right)^2 I(\omega_1)I(\omega_2) \qquad [3]$$

or in terms of photons per pulse,

$$S^{EQ}(\omega_1+\omega_2)=I^{EQ}(\omega_1+\omega_2)AT \qquad [4]$$

Here A is the input beam overlap area and T is the temporal pulse width. Using α=45°, β=-45°, $\theta_1=\theta_2$, $\pi/\Delta k=z_{opt}$= 872nm, A=2 mm^2 (large enough beam size to avoid damage), T=70 ps, $\varepsilon(\lambda_1\cong\lambda_2$=1064nm)=4.0, $\varepsilon(\lambda_3$=532nm)=5.29, $I(\omega_1)$=400mW, $I(\omega_2)$=100mW, and a detection efficiency of 5%, we obtain

$S^{EQ}(\omega_1+\omega_2)\approx 0.03$ photons/pulse,

which is well above the background of .0003 photons per pulse for our detection arm. In the case of the SF signal enhanced by the MD transition, we get (for the same film thickness)

$S^{MD}(\omega_1+\omega_2)\approx 0.3$ photons/pulse

which is about an order of magnitude higher because $\chi^{MD} \cong 9\chi^{EQ}$.

Conclusion

In this section we have discussed how to carry out the experiment to test the idea of using nonlinear spectroscopy to probe pure EQ and MD transitions across the HOMO-LUMO gap of the C_{60} molecule. This idea(discussed in chapter 3) can be tested by using a commercial CW Q-switched and Mode-locked Nd:YAG laser along with a synchronously-pumped Optical Parametric Oscillator (OPO) which is tunable from 650-2900 nm. Growing a C_{60} under UHV conditions insures

negligible effects of contamination and the proper geometry of should allow one to observe the EQ and MD resonant spectrum of C_{60}.

References

1. F. Negri, G. Orlandi, F. Zerbetto, Chem. Phys. Lett. **144**, 31 (1988).

2. Pershan, P. S., Phys. Rev. **130**, 919 (1963).

3. R. L. Byer and R. L. Herbst, Parametric Oscillation and Mixing, in Topics in Applied Physics, vol. 16: Nonlinear Infrared Generation, ed. by Y. R. Shen (Springer-Verlag, Berlin, Heidelberg, New York 1977), p. 81.

4. C. Chen, Laser Focus World, **129**, Nov. 1989.

5. G. Robertson, M. H. Dunn, and M. Ebrahimzadeh, CFM2, CLEO, 1991, Baltimore, CA

6. Z. Xu, D. Deng, Y. Wang, CWE6, CLEO, 1990, Anaheim, CA.

7. Y. R. Shen, Principles of Nonlinear Optics, Wiley and Sons, 1984.

Figure Captions

Fig. (1)

Schematic of a optical parametric oscillator. ω_p is the pump frequency, ω_s is the signal frequency, and ω_i is the idler frequency.

Fig. (2)

Schematic of temperature-tuned singly-resonant LBO optical parametric oscillator used in our experiment.

Fig. (3)

Schematic of tunable SFG experiments on the C_{60} thin film using the OPO, QS ML Quantronix Laser, and the UHV chamber system.

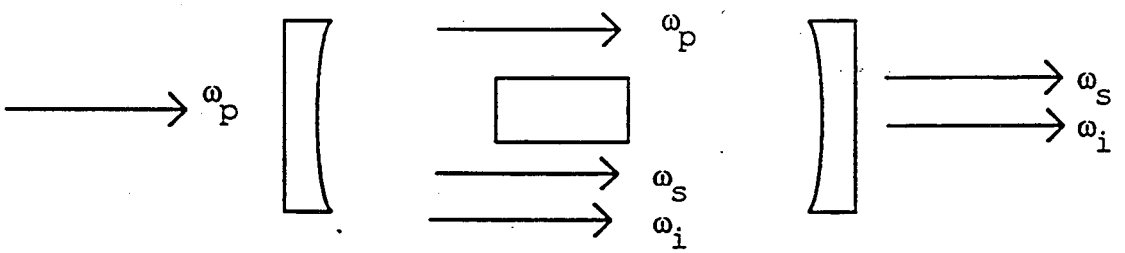

Fig. 1

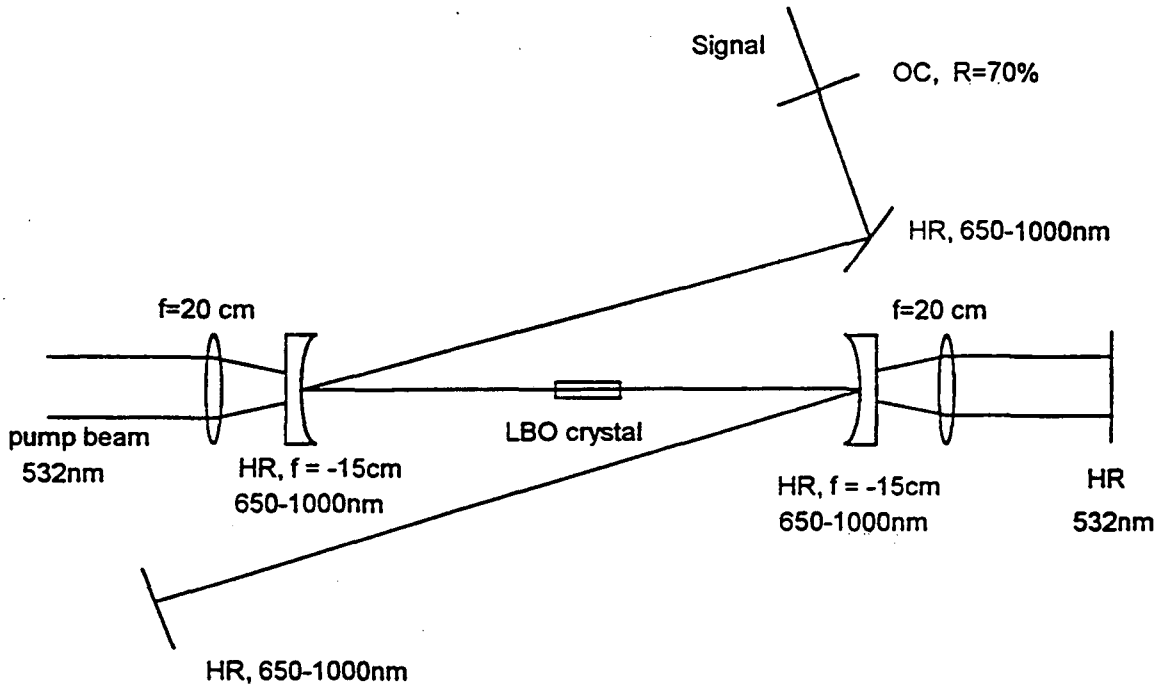
Signal
OC, R=70%
HR, 650-1000nm
f=20 cm
f=20 cm
pump beam
532nm
HR, f = -15cm
650-1000nm
LBO crystal
HR, f = -15cm
650-1000nm
HR
532nm
HR, 650-1000nm

Fig. 2

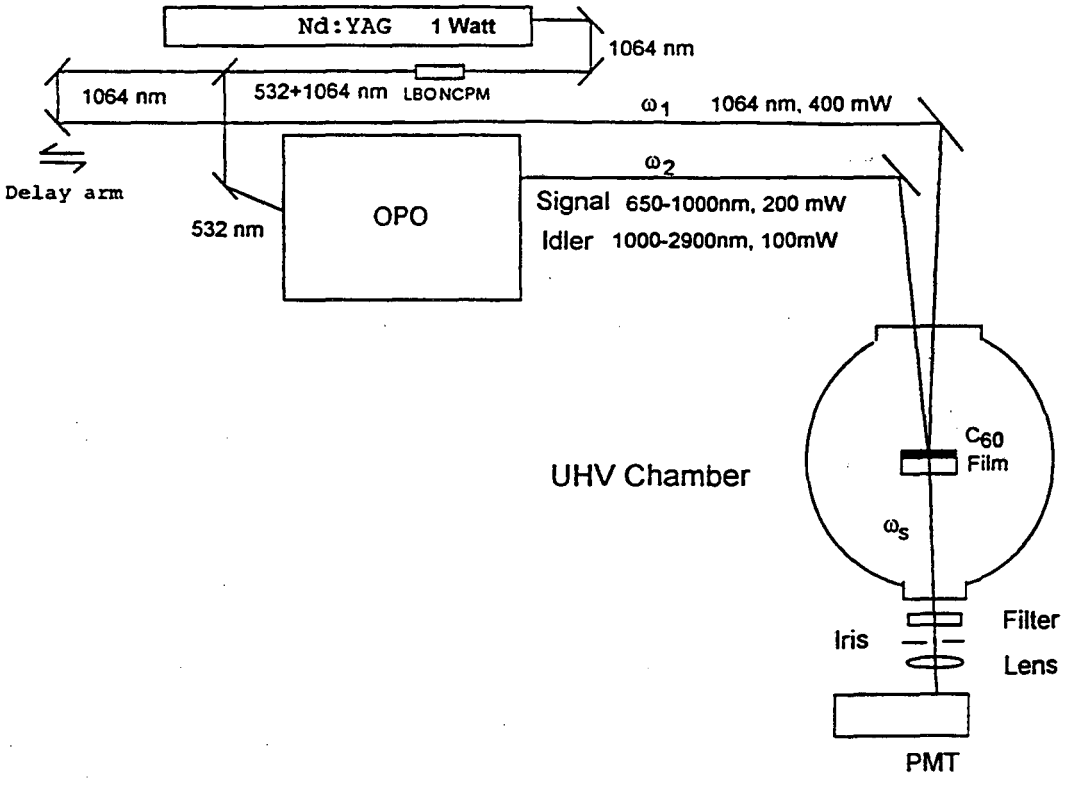
Nd:YAG 1 Watt
1064 nm
1064 nm
532+1064 nm LBONCPM
ω_1 1064 nm, 400 mW
Delay arm
532 nm
OPO
ω_2
Signal 650-1000nm, 200 mW
Idler 1000-2900nm, 100mW
UHV Chamber
C_{60} Film
ω_s
Iris
Filter
Lens
PMT

Fig. 3

VI. Adsorption Structure and Thermal Decomposition of Ortho- and Para-Xylene on Pt(111)

Introduction

Aromatic compounds are an important class of organic molecules. Most adsorption and thermal decomposition studies of aromatics on metal surfaces have been performed using benzene (1, 2). However, adsorption and thermal decomposition of dimethyl substituted benzene molecules on platinum have not been investigated. An interesting aspect of the thermal decomposition of methyl substituted aromatics on transition metal surfaces is that initial decomposition occurs by dehydrogenation of the methyl groups. Thermal desorption studies of selectively deuterated toluene on Ni(111) show that aliphatic CH bond breaking occurs more readily than aromatic CH bond breaking (3). This dehydrogenation pathway also occurs initially for toluene on Pt(111) (4). In another study (5), thermal desorption spectra of partially deuterated o- , m-, and p-xylene ($(CD_3)_2C_6H_4$) on Ni(111) and Ni(100) showed that all xylenes decompose with the aliphatic CH bonds breaking at a lower temperature than the aromatic CH bonds. In view of the limited information on disubstituted benzene chemisorption and the importance of Pt(111) as a catalyst for aromatic hydrocarbon reactions, we have investigated the molecular structure and thermal decomposition fragments of p- and o-

xylene on Pt(111) using high resolution electron energy loss spectroscopy (HREELS), thermal desorption spectroscopy (TDS), and low energy electron diffraction (LEED). This is the first time that HREELS has been used to study the adsorption and decomposition of xylenes on any transition metal surface. We found that both p- and o-xylene undergo stepwise dehydrogenation and the initial dehydrogenation occurs at the methyl groups, leaving the aromatic ring structure intact on the surface. We have proposed structural models for p- xylene ond o-xylene between each dehydrogenation step of the decomposition process.

Experimental

The experiments were performed in a single stage UHV chamber with a background pressure of $2x10^{-10}$ torr. The system is equipped with a high resolution electron energy loss spectrometer (HREELS), a quadrupole mass spectrometer, low energy electron diffraction (LEED), and Auger electron spectroscopy (AES). A tube made from tantalum foil was placed over the end of the mass spectrometer to eliminate background signal from the manipulator parts during the thermal desorption experiments. The high resolution electron energy loss spectrometer is described in detail elsewhere (6). Briefly, the spectrometer consists of two 120 degree cylindrical deflectors (monochromator and analyser) with a cathode system for generating electrons, electrostatic lenses for guiding and focusing the electron beam, and a

channeltron detector for electron counting. The angle of incidence of the electron beam on the sample is 60 degrees with respect to the surface normal. Typically, experiments were performed with a beam energy of 3.2 eV and a resolution of 50-80 cm^{-1}. The platinum crystal used in the experiments was oriented in the (111) direction to +-0.5 degree and polished using standard procedures. The crystal was initially cleaned by cycles of high temperature oxygen treatment ($1x10^{-7}$ torr) at about 800K followed by argon bombardment (600 eV, $2x10^{-5}$ torr Ar) at room temperature and annealing in UHV at 1300 K. The daily cleaning treatment consisted of about 15 minutes of Argon bombardment (6 μA at the sample) at room temperature followed by annealing in ultra-high vacuum (UHV) at 1300K. Cleanliness of the surface was monitored by AES and HREELS. The para-xylene and ortho-xylene used in these experiments were obtained from Aldrich Chemical Company (99%) and Baker Anaylzed (reagent grade), respectively. Fully deuterated o-xylene (o-xylene-d_{10}), p-xylene (p-xylene-d_{10}) and p-xylene with deuterated methyl groups (p- xylene-d_6), all at 99% purity, were obtained from Aldrich chemical company. O-xylene with deuterated methyl groups (o-xylene-d_6), at 99% purity, was purchased from Merck Isotope Company. All the xylenes were treated with several freeze-pump-thaw cycles before each experiment. The leak valve used for the xylenes was equipped with a tube, allowing more direct dosing of the sample. During xylene dosing, the sample surface was placed about 1 inch from the

end of the tube. Exposures (1 L = $1x10^{-6}$ torr-sec) reported are not corrected for ion gauge sensitivity.

Results and Discussion

1) Thermal Desorption Spectroscopy (TDS) and Low Energy Electron Diffraction (LEED)

Thermal desorption experiments were performed after the Pt(111) surface was exposed to 2L of the xylene at 150K, under which conditions both xylenes formed a multilayer. A full monolayer was prepared by dosing at least 0.5L of xylene at temperatures between 245K and 275K. The heating rate for all thermal desorption experiments was approximately 10K/s. The thermal desorption spectrum of p-xylene, monitoring mass 106 is shown in Fig. 1a. The low temperature peak at about 200K is due to desorption of multilayer p-xylene and at 325K a small fraction of the monolayer desorbs intact. Auger intensity measurments of the carbon 272 eV peak before and after the monolayer desorption indicate that only 10% of the p-xylene leaves the surface, while the rest stays and eventually decomposes. A similar result was obtained for toluene on Pt(111) (4), where it was shown that less than 10% of the molecule desorbs from the surface at about 340K. Following a saturation dose of p-xylene-d_{10} at 245K, a thermal desorption experiment was performed while monitoring the D_2 evolution (mass 4), as shown in Fig. 2. The spectrum shows peaks at 345 K and 550K with a broad shoulder at 640K. The areas under each of the

desorption peaks relative to the total area were 0.2 (345K peak), 0.5 (550K peak), and 0.3 (640K shoulder). To determine the origin of the D_2 desorption peaks, the thermal desorption of p-xylene-d_6 ((CD_3)$_2C_6H_4$) was performed while the mass signals of H_2 (mass 2), D_2 (mass 4), and HD (mass 3) were recorded, as shown in Fig. 3. At 345K mainly D_2 desorbs, indicating that decomposition is occuring at the methyl groups. This result, combined with the relative area under the 345K peak, shows that two methyl deuterium atoms for each p-xylene-d_{10} molecule are lost at this temperature. A small amount of HD appears, indicating that some exchange occurs on the surface. At 550K H_2, D_2, and HD evolve from the surface. Comparing the H_2, HD, and D_2 spectra (Fig. 3), it appears that D_2 begins to desorb at a slightly lower temperature than HD or H_2, which indicates that further decomposition starts at the aliphatic carbons of p- xylene. By comparing the relative areas of the the H_2, D_2, and HD peaks at 545K, one finds that equal amounts of H and D evolve from the surface. This shows that both the aromatic and aliphatic CH bonds break at this temperature. The decomposition pattern of p-xylene exhibited in these results is very similar to that of toluene, where initial decomposition occurs at the methyl group at 345K and further hydrogen evolution from both the methyl and aromatic groups occurs at about 500K (4). The thermal desorption spectrum of o-xylene at mass 106 is nearly identical to that of p-xylene, as shown in Fig. 1b. A multilayer peak at about 200K

was observed and a small molecular desorption peak at 315K was also detected, indicating that most of the monolayer of o-xylene remains on the surface. The o-xylene-d_{10} deuterium thermal desorption spectrum, shown in Fig. 4, gives D_2 peaks at 350K, 445K and 615K. The initial decomposition occurs at the same temperature as that of p-xylene-d_{10} and the relative area under the peak at 350K corresponds to a loss of 2 deuterium atoms for each o-xylene-d_{10} molecule. The main difference in this spectrum, as compared to that for p-xylene-d_{10}, is the desorption peak at 445K, which accounts for 4 deuterium atoms for each o-xylene-d_{10} molecule. The thermal decomposition of o-xylene was further investigated by monitoring H_2, D_2, and HD evolution during the thermal decomposition of o-xylene-d_6, as shown in Fig. 5. Mainly D_2 evolves from the surface at 350K and 445K, showing that the methyl groups completely dehydrogenate before any aromatic CH bonds are broken. Small quantities of H_2 and HD were detected at these temperatures. This indicates that some diffusion and exchange on the surface occur. Above 445K only H_2 evolves from the surface, indicating that the aromatic CH bonds stay intact until about 600K. The thermal decomposition of both o- and p-xylene occurs in a stepwise fashion, similar to what is observed for the decomposition of alkenes on Pt(111) (7,8). This implies that the xylenes are decomposing to stable fragments on the surface after each dehydrogenation step. We have further characterized the surface species by LEED and EELS at temperatures between the

H_2 desorption peaks, where relatively stable surface species exists.

Low energy electron diffraction (LEED) experiments were performed after annealing to the desired temperatures and cooling to 120K. The annealing temperatures were chosen to correspond to the stable surface fragment regions, as determined by the thermal desorption experiments. For p-xylene, a disorded ring pattern around the Pt(111) substrate spots was visible at 245K and remained after annealing to 370K. This pattern is similar to the pattern seen from benzene on Pt(111) (9). However, at 570K, only a diffuse background was visible, indicating that the structure of the adsorbate layer changes significantly after the evolution of H_2 at 550K (see Fig. 2). In the case of o-xylene a similar diffuse ring pattern was visible at 245K and 370K. But at 470K the ring pattern disappeared and only a diffuse background was observed. Therefore, one can associate a significant change in the structure of the adsorbate layer with the dehydrogenation peak at 445K(see Fig. 4).

2) High Resolution Electron Energy Loss Spectra (HREELS)

The results of the HREELS experiments are presented in the following order. First, the multilayer and monolayer spectra of intact p- xylene and o-xylene are considered, and then the dehydrogenated fragments at higher temperatures are discussed. The temperatures chosen for the decomposition studies correspond to temperatures between the hydrogen

thermal desorption peaks. For each spectrum, the sample was annealed to the appropriate temperature for several minutes and then cooled to 120K, at which point the spectrum was obtained. All results shown were obtained from an initial saturation coverage of adsorbate.

a) p-Xylene and o-Xylene Multilayers at 120K

The multilayer spectra of p-xylene, p-xylene-d_{10} and o-xylene, o-xylene-d_{10} on Pt(111) are shown in Figs. 6 and 7. These spectra were obtained to help interpret the HREELS spectra of p- and o-xylene monolayers on Pt(111) and their thermal decomposition fragments. All HREELS loss features were readily assigned to the liquid phase infrared absorption bands, as shown in Tables 1 and 2 (10). The deuterated HREELS loss frequencies are shown in parentheses, adjacent to those corresponding to the hydrogenated loss features. In subsequent tables and discussions the corresponding hydrogenated and deuterated loss frequencies will appear in this manner.

b) p-Xylene and o-Xylene at 245K

It is known from the TDS data that at 245K p- and o-xylene remain intact on Pt(111). The HREELS spectra for p-xylene, p-xylene-d_{10}, and p-xylene- d_6 monolayers are shown in Fig. 8 and the corresponding mode assignment is shown in Table 1. The strong feature at 860 (665) cm^{-1} is assigned to an out-of-plane CH bending mode, which is shifted up in frequency from the 798 cm^{-1} liquid phase infrared and HREELS

multilayer frequency. This feature is also observed in the p-xylene-d_6 spectrum at 885 cm^{-1}, where it is overlapped with the CD_3 "rocking" mode . The upward frequency shift of the out-of-plane CH bending modes is a general feature for aromatic molecules bonded to a transition metal surface, which has been observed for benzene on many transition metal surfaces (11) and for toluene (12) and pyridine (13) on Pt(111). For benzene on Pt(111), the out-of-plane CH mode shifts from the liquid phase value of 671 cm^{-1} to 800 cm^{-1} when adsorbed on the surface (14). This frequency shift for aromatic molecules can be explained by rehybridization of the carbon atoms of the aromatic ring, which is caused by bonding of the occupied p-orbital (π-bonding) of the aromatic ring to the surface. Molecular orbital calculations of benzene bonded to chromium tricarbonyl and to cluster models of Ag(111), Ni(111), and Pt(111) show that the p-orbital of the aromatic ring must distort to maximize overlap with the d-orbitals of the metal atoms (15). This distortion results in a rehybridization of the carbon atoms from sp^2 toward sp^3. Gas phase spectra of various organic molecules show that the CH bending modes increase in frequency as the hybridization of the carbon atoms change from sp to sp^2 to $sp^3$3 (16). Therefore, the upward shift in frequency for the CH out-of-plane mode of p-xylene on Pt(111) indicates that p-xylene is also bonded to the surface through the p-electrons of the aromatic ring. The frequency shift also indicates that the aromatic ring is

parallel to the surface, since the most efficient overlap of the p-orbital with the surface is achieved with this molecular orientation. The parallel orientation of p-xylene with respect to the Pt(111) surface is confirmed by comparing the IR absorption spectra of liquid p-xylene with the HREELS spectra and by using the surface dipole selection rule. Infrared active dipole modes parallel to the molecular ring plane at 1529 cm^{-1} (ring stretch) and 1027 cm^{-1} (in-plane CH bend) and perpendicular to the ring plane at 860 cm^{-1} (CH bend) have similar dipole intensities in the liquid phase infrared spectum (10). In our HREELS spectrum (Fig. 8), the strong out-of-plane CH bend at 860 cm^{-1} and no visible dipole dominated modes parallel to the plane indicates that the aromatic ring is oriented parallel to the Pt(111) su rface . The peaks appearing at 1040, 1365, and 1445 cm^{-1} and their shifts upon deuteration are consistent with a CH_3 rocking mode, CH_3 symmetric deformation, and CH_3 antisymmetric deformation, respectively. The barely resolved peaks at 2915 and 3010 cm^{-1} in the p-xylene spectrum are assigned to the CH_3 and aromatic CH stretches, respectively. The CH_3 and aromatic CH stretches are most clearly distinguished in the p-xylene-d_6 spectrum (Fig. 8). The CD_3 stretches appear at 2105 (symmetric stretch) and 2225 cm^{-1} (antisymmetric stretch) and the aromatic CH stretch is visible at 3010 cm^{-1}. In conclusion, the HREEL spectra at this temperature are consistent with p-xylene adsorbed intact on the Pt(111) surface with the aromatic ring

oriented parallel to the su rface . The HREEL spectra of o-xylene and o-xylene-d_{10} at 245K, shown in Fig. 9, look similar to the p-xylene spectra at this temperature. The assignment of the loss features is shown in Table 2. The spectra show a strong feature at 845 (645) cm^{-1}, which is due to a CH out-of- plane bending mode. This mode is shifted up in frequency from the infrared liquid phase value of 729 cm^{-1}, indicating that o-xylene is also pI-bonded to the surface and oriented with the aromatic ring parallel to the surface. The relatively high intensity of the out-of-plane CH mode at 845 cm^{-1} and the absence of observable dipole dominated in-plane modes confirms that the aromatic ring is oriented parallel to the surface. The o-xylene CH_3 rock and deformations as well as the CH_3 and CH stretches are readily assigned from agreement with the liquid phase infrared frequencies. We conclude that a monolayer of o-xylene adsorbs intact at 245K with the aromatic ring oriented parallel to the surface.

c) p-Xylene Decomposition

p-Xylene at 370K

At this temperature the TDS results show that two methyl hydrogen atoms for each p-xylene molecule have been lost. The HREEL spectra for p-xylene, p-xylene-d_{10}, and p-xylene-d_6 after annealing to 370K are shown in Fig. 10 and the corresponding mode assignment is shown in table 3. Changes in the surface species due to the dehydrogenation are

reflected in the HREELS spectra at this temperature. The loss peak at 875 (675) cm^{-1} is assigned to the aromatic CH (CD) out-of-plane bend of the ring, since this peak does not undergo a downward frequency shift when the methyl groups are deuterated. This feature has decreased considerably in relative intensity at this temperature compared to the relative intensity of the same mode at 245K. The strong loss feature at 1440 cm^{-1} in the p-xylene spectrum, which is not observed in the p- xylene spectrum at 245K, shifts to 1340 cm^{-1} in the fully deuterated p-xylene-d_{10} spectrum and shifts only 10 cm^{-1} to 1430 cm^{-1} in the partially deuterated p-xylene-d_6 spectrum. This shows that the loss peak is also due to a ring vibration, and is closest in frequency to the in-plane ring stretch of liquid p-xylene at 1530 cm^{-1}. Applying the dipole selection rule, the decrease in intensity of the out-of-plane 875 cm^{-1} ring CH bend and the appearance of the 1440 cm^{-1} in-plane ring stretch suggests that the aromatic ring may be tilted with respect to the surface at this temperature. However, off-specular measurements (not shown here) show that this loss feature is due to impact scattering and therefore we cannot use the dipole selection rule to determine if the molecule is tilted .

After this first dehydrogenation step, the HREEL spectra of p-xylene show that both aromatic and aliphatic CH groups remain on the surface. This is most clearly observed in the

p-xylene-d_6 spectrum, where the aromatic CH stretch appears at 3005 cm^{-1} and the aliphatic CD stretches appear at 2160 and 2240 cm^{-1} (Fig. 10c). These two different CH (CD) stretches appear as broad loss peaks in the p-xylene and deuterated p- xylene spectra. Unfortunately, the limited resolution of our HREEL spectrometer does not allow one to distinguish between CH_2 andCH_3 modes in this case. If we look for other features in our HREELS spectra corresponding to characteristic frequencies of CH_2 andCH_3 groups, we find that the assignment cannot be definite because of mode overlapping. The peaks at 1055cm^{-1} (815 cm^{-1}) and 1440 cm^{-1} (1050 cm^{-1}) can be assigned to the CH_3 group rock and deformation, respectively (the CH_3 deformation is overlapped with the in-plane ring mode at 1440 cm^{-1}). Alternatively, the 1055 cm^{-1} peak could be assigned to a CH_2 "wagging" mode and the 1440 cm^{-1} peak could be due to a CH_2 "scissors" mode. The ambiguity in the assignment of aliphatic CH modes of the p-xylene fragment leads to more than one possible surface species at this temperature. The thermal desorption results indicate that 2 hydrogens per p-xylene molecule are lost from the surface, leaving 8 hydrogen atoms in the p-xylene fragment. The two likely surface fragments are shown in Figs. 11 a and 11 b. The fragment in Fig. 11a has a CH_3 group attached to the aromatic ring and the mode assignment is shown in column three of Table 3. Loss features due to the remaining CH group after dehydrogenation could be overlapped with the CH_3 stretching mode and the

aromatic CH out-of-plane bending mode. To produce this fragment from intact p- xylene, one of the methyl carbons of p-xylene loses two hydrogen atoms and the other methyl group remains intact, resulting in a likely tilted fragment which is bonded to the surface through the aromatic ring and one methyl carbon. In this figure and in all following illustraions of surface fragments the platinum atoms are not shown because the bonding site is uncertain . For the fragment in Fig. 11 b, the HREELS assignment is also shown in column 3 of Table 3. This symmetric structure consists of only CH aromatic and CH_2 groups and is obtained by the loss of one hydrogen atom from each CH_3 group. One expects the aromatic ring to be oriented nearly parallel to the surface in this case, with perhaps a small tilt or distortion due to unequal bonding sites of the two methyl carbons. This structure is still consistent with the presence of the in-plane mode at 1440 cm^{-1}, since dipole scattering does not contribute to this feature. Therefore, the dipole selection rule cannot be used to determine the orientation of the aromatic ring. This fragment is supported by previous experiments with toluene on Pt(111) and TDS results of of toluene on Pt(111) obtained in this laboratory, which have indicated that toluene first decomposes at the methyl group at 340K (4). The most likely fragment of toluene is a benzyl group which is bonded to the platinum surface through the aromatic ring and through the substituent carbon. Further dehydrogenation of toluene does not occur until about 500K,

which suggests that breaking the CH bond of the CH_2 group of the fragment requires considerably more energy than breaking the methyl CH bond of intact toluene on the surface. Given the chemical similarity of toluene and p-xylene and their similar H_2 thermal desorption spectra on Pt(111), we expect that p-xylene dehydrogenates at 345K by losing one hydrogen atom from each methyl group, as opposed to losing 2 hydrogen atoms from one of the methyl groups.

p-Xylene at 550K

At this temperature p-xylene has lost 7-8 hydrogen atoms per molecule, as determined from the TDS results. The HREELS spectrum for the p-xylene fragments is shown in Fig. 12 and the assignment is given in Table 4. The features at 800 cm^{-1} and 3100 cm^{-1} can be attributed to the CH bend and stretch of CH and C_2H fragments, respectively, while the broad hump centered at 1300 cm^{-1} can be attributed to the CC stretch of C_2H fragment. Very similar spectra of CH and C_2H fragments left by decomposition of alkenes on Pt(111) (8) and Rh(111) (2) have been successfully compared to spectra of organometallic CH and C_2H ligands . From the HREELS spectra, it is clear that the decomposition of the aromatic ring occurs by CH and CC bond beaking at 540K, leaving only polymeric carbon, CH and C_2H on the surface.

d) o-Xylene Decomposition

o-Xylene at 370K

As in the case of p-xylene, TDS results show that 2 hydrogen atoms for each o-xylene molecule have been lost at this temperature. The spectra for o-xylene and fully deuterated o-xylene-d_{10} on Pt(111) after annealing to 370K are shown in Fig. 13. These spectra look similar to the spectra of p-xylene at this temperature and the mode assignment is shown in Table 5. The loss peak at 855 (605) cm^{-1} is assigned to the CH out-of-plane bend, and is also present in the o-xylene spectra at 245K. The presence of this mode, shifted up in frequency from the infrared liquid phase value, indicates that the aromatic ring structure of o-xylene is still intact and that the ring is bonded to the Pt surface through the electrons, as was the case for p-xylene at this temperature. However, new peaks at 1150, 1380 (1250) and 1450 (1340) cm -1, which are not observed at 245K, can be assigned to in-plane modes of the aromatic ring. The appearance of these modes parallel to the ring plane suggests that the aromatic ring is tilted with respect to the surface. The 855 cm^{-1} out-of- plane mode still dominates the spectrum and so it is expected that the tilt of the ring is small. The features at 1040 (805) cm^{-1} and 2950 (2135) cm^{-1} have two possible interpretations. Assuming a CH_3 group remains on the o-xylene fragment, the 1040 cm^{-1} loss can be due to a CH_3 rocking mode while the 2950 cm^{-1} feature can be due to a CH_3 stretch. However, if only CH_2 groups were to remain on the o-xylene fragment, then we can assign the 1040 cm^{-1} loss to a CH_2 "wagging" mode and the

2950 cm^{-1} loss to the CH_2 stretch. As in the case for p-xylene at this temperature, the resolution of the HREELS technique does not allow one to distinguish these two groups. The most likely o-xylene fragment structures at 370K are shown in Figs. 14a and 14b. Both structures can give a tilted aromatic ring as suggested by the HREELS spectra and both have 8 remaining hydrogen atoms, consistent with the TDS data. It has been observed for decomposition of hydrocarbons on transition metal surfaces that the proximity of the CH bond to the surface plays the most important role for realising facile carbon-hydrogen bond breaking (17). Therefore, the structure in Fig. 14b seems more likely because the loss of a hydrogen from one methyl group would tend to bring the other methyl group closer to the platinum surface, facilitating CH bond breakage. Also, previous experiments involving toluene support tilting of the aromatic ring of o-xylene after initial decomposition at the methyl groups. For toluene on Pt(111) it was found that initial dehydrogenation of the methyl group occurs at 340K (4), which is at the same temperature found in the present study for o-xylene on Pt (111). It was also shown by NEXAFS that below 340K the aromatic ring is oriented parallel to the surface and above 340K the ring is tilted (18).

o-Xylene at 470K

At this temperature, TDS results show that all six hydrogen atoms of the methyl groups of each o-xylene molecule have

been lost. After annealing to 470K, the o-xylene and deuterated o-xylene spectra (Fig. 15) appear very different from the o-xylene spectra at 245K and 370K. The mode assignment is shown in Table 6. We assign the strong loss feature at 1235 (1170) cm^{-1} to a C-C stretching mode between the methyl and aromatic carbon atoms because of the relatively small isotope shift (ω_H/ω_D= 1.05) compared to the isotope shifts expected for modes involving motion of the hydrogen atoms (ω_H/ω_D= 1.20-1.40). Also, this frequency closely corresponds with the CC stretch found in the liquid phase o-xylene spectrum. The feature at 1535 (1340) cm^{-1} is assigned to an in-plane ring stretch and the loss feature at about 870 (870) cm^{-1} is assigned to a pure CC breathing mode of the aromatic ring. The CC breathing mode is assigned here because almost no isotope shift in the frequency of this peak rules out the possibility of a CH vibration. The loss feature appearing at 3095 cm^{-1} is assigned to the aromatic CH stretch. The loss peak at 760 cm^{-1} in the o-xylene spectrum appears to shift down in frequency to 605 cm^{-1} in the o-xylene -d_{10} spectrum and therefore is due to a CH mode. The frequency of this loss peak is close to that of the out-of-plane CH bending mode, which appears at 729 cm^{-1} in the o-xylene liquid phase IR spectrum. The peaks appearing at 620 cm^{-1} (overlapped with the CH out-of-plane bend in the o-xylene-d_{10} spectrum) and 450 cm^{-1} in the o-xylene spectra are attributed to metal-carbon modes. These loss features show negligible frequency shifts in the fully

deuterated o-xylene spectrum, ruling out the possibility of their being due to CH modes. The low frequency CC ring modes seem unlikely, since they are very weak in the liquid phase spectra of o-xylene, leaving only metal carbon modes as a possibility. At 470K, the possible surface species is a fragment which has lost all of the aliphatic hydrogen atoms and is bonded to the surface through the aliphatic carbon atoms (See fig. 16). The strongest evidence for this structure is given by the intense mode at 1235 (1170) cm^{-1}, which is close to the C-C stretch mode for o-xylene. The additional ring modes at 1535 (1340) cm^{-1} and 870 (870) cm^{-1} are also consistent with this structure. The 765 (605) cm^{-1} loss feature is assigned to the same mode that appears at 845 cm^{-1} at 245K and, when the o-xylene molecule is p-bonded and oriented parallel to the surface. The fact that the mode has now shifted to lower frequency, closer to the liquid phase infrared value of 729 cm^{-1}, indicates that the aromatic ring of the fragment is no longer p-bonded to the surface. The weak intensity of the 760 cm^{-1} out- of-plane mode compared to the strong intensity of the in-plane mode at 1235 cm^{-1} suggests that the aromatic ring is now oriented more towards the surface normal. The absence of loss features around 2950 cm^{-} rules out the possibility of CH_2 or CH_3 groups on the surface.

o-Xylene at 640K

It is known from our TDS results that only 1 to 2 hydrogen atoms for each o-xylene molecule remain on the surface at this temp- erature. After annealing to 640K, the HREELS spectrum of o-xylene fragments is similar to that for p-xylene fragments at 550K and is shown in Fig. 17. The three peaks seen here can be attributed to a Pt-C mode and CH groups on the surface. The peak at 800 cm^{-1} can be assigned to a CH bend while the peak at 3100 cm^{-1} is given by the CH stretch. No loss features around 1300 cm^{-1} were observed, which would correspond to the C-C stretch mode of a C_2H species. The loss feature at 400 cm^{-1} corresponds to the Pt-C stretch. Therefore, at this temperature, only polymeric carbon and CH groups remain on the surface. The assignment is shown in Table 7.

Conclusions

The chemisorption and subsequent thermal decomposition of o- xylene and p-xylene on Pt(111) has been studied. We have shown that both xylenes bond intact to the Pt surface with the aromatic ring parallel to the surface and are stable at 245K. Upon increasing the temperature, both p- xylene and o-xylene initially lose 2 methyl hydrogens per molecule, with the ring structure staying intact. The HREELS results indicate that the aromatic ring is likely tilted for o-

xylene after the initial dehydrogenation at 340K. Above 340K the decomposition pattern for p- and o-xylene are markedly different. The p-xylene fragment undergoes further decomposition at 540K to give CH and C_2H fragments. The o-xylene fragment loses the remaining aliphatic hydrogen atoms at 440K, leaving a fragment which is bonded to the surface through the previously aliphatic carbon atoms with the aromatic ring intact and nearly perpendicular to the surface. At 640K, the o-xylene fragment further decomposes to give CH species.

References

1. (a) K. L. Shanahan; E. L. Muetterties, J. Phys. Chem. 88 (1984) 1996, and references therein. (b) B. E. Koel, J. E. Crowell, C. M. Mate, G. A. Somorjai J. Phys Chem. 88 (1984) 1988, and references therein.

2. B. E. Koel, J. E. Crowell, B. E. Bent, C. M. Mate, and G. A. Somorjai, J. Phys. Chem. 90 (1986) 2949.

3. C. M. Friend and E. L. Muetterties, J. Am. Chem. Soc. 103 (1981) 773.

4. Min-Chi Tsai and E. L. Muetterties, J. Am. Chem. Soc. 103 (1981) 773.

5. D. G. Klarup, E. L. Muetterties and A. M. Stacy, Langmuir 1 (1985) 764.

6. L. Dubois, Ph. D. Thesis, University of California, Berkeley, 1981.

7. A. M. Baro and H. Ibach, J. Chem. Phys. 74(7) (1981) 4194.

8. N. R. Avery and N. Sheppard, Proc. R. Soc. Lond. A 405 (1986) 1.

9. D. F. Ogletree, M. A. Van Howe and G. A. Somorjai, Surf. Sci. 183 (1987) 1.

10. L. M. Sverdlov, M. A. Kovner and E. P. Krainov et. al., Vibrational Spectra of Polyatomic Molecules (Halsted Press, New York, 1974) p. 338.

11. G. D. Waddill and L. L. Kesmodel, Phys. Rev. B 31(8) (1985) 4940.

12. M. Abon, J. C. Bertolini, J. Billy, J. Massardier and B. Tardy, Surf. Sci. 162 (1985) 395. 13. V. H. Grassian and E. L. Muetterties, J. Phys. Chem. 90 (1986) 7183.

14. S. Lehwald, H. Ibach and J. E. Demuth, Surf. Sci. 78 (1978) 578.

15. A. B. Anderson. M. R. McDevitt and F. L. Urbach, Surf. Sci. 146 (1984) 80.

16. T. Shimanouchi, Natl. Stand. Ref. Data Ser., Natl. Bur. Stanc. No. 39, J. Chem. Ref. Data, 6 (1977) 993.

17. G. A. Somorjai, Chemistry in Two Dimensions, Cornell University Press, Ithaca, NY, 1981. 18. A. L. Johnson, E. L. Muetterties, J. Stohr, F. Sette, J. Phys. Chem. 89 (1985) 4071. 27

Figure Captions

Figure 1.

Thermal desorption spectra of a) p-xylene and b) o-xylene following multilayer deposition on Pt(111) at 150K.

Figure 2.

D_2 thermal desorption spectrum from the decomposition of a saturation coverage at 245K of fully deuterated p-xylene-d_{10} on Pt(111).

Figure 3.

H_2, HD, D_2 thermal desorption spectra from the decomposition of a saturation coverage at 245K of partially deuterated p-xylene-d_6 ($(CD_3)_2C_6H_4$) on Pt(111).

A sketch of the probable decomposition pathway is shown above the spectra.

Figure 4.

D_2 thermal desorption spectrum from the decomposition of a saturation coverage at 245K of fully deuterated o-xylene-d_{10} on Pt(111).

Figure 5.

H_2, HD, D_2 thermal desorption spectra from the decomposition of a saturation coverage at 245K of partially deuterated o-xylene-d_6 ($(CD_3)_2C_6H_4$) on Pt(111).

A sketch of the probable decomposition pathway is shown above the spectra.

Figure 6.

HREEL spectra of a) p-xylene and b) fully deuterated p-xylene-d_{10} multilayers deposited on Pt(111) at 120K.

Figure 7.

HREEL spectra of a) o-xylene and b) fully deuterated o-xylene-d_{10} multilayers deposited on Pt(111) at 120K.

Figure 8.

HREEL spectra of saturation coverages of a) p-xylene, b) fully deuterated p-xylene-d_{10}, and c) partially deuterated p-xylene-d_6 adsorbed on Pt(111) at 245K.

Figure 9.

HREEL spectra of saturation coverages of a) o-xylene and b) fully deuterated o-xylene-d_{10} adsorbed on Pt(111) at 245K.

Figure 10.

HREEL spectra of a) p-xylene, b) fully deuterated p-xylene-d_{10}, and c) partially deuterated p-xylene-d_6 full monolayers on Pt(111) after annealing to 370K.

29

Figure 11.

Two possible surface fragments from the decomposition of a full monolayer of p-xylene on Pt(111) after annealing to 370K: a) fragment left after losing two hydrogen atoms at one methyl group b) fragment left after losing one hydrogen atom from each methyl group.

Figure 12.

HREEL spectrum of a full monolayer of p-xylene after annealing to 550K.

Figure 13.

HREEL spectra of a) o-xylene and b) fully deuterated o-xylene-d_{10} full monolayers on Pt(111) after annealing to 370K.

Figure 14.

Two possible surface fragments from the decomposition of a full monolayer of o-xylene on Pt(111) after annealing to 370K: a) fragment left after losing two hydrogen atoms at one methyl group b) fragment left after losing one hydrogen atom from each methyl group.

Figure 15.

HREEL spectra of a) o-xylene and b) fully deuterated o-xylene-d_{10} full monolayers on Pt(111) after annealing to 470K.

Figure 16.

Fragment left from the decomposition of a full monolayer of o-xylene on Pt(1 1 1) after annealing to 470K.

Figure 17.

HREEL spectrum of a full monolayer of o-xylene after annealing to 640K.

Table 1

Multilayer p-Xylene on Pt(111) (cm^{-1})	Monolayer p-Xylene on Pt(111) (cm^{-1})	Infrared Liquid Phase p-Xylene (cm^{-1})	Symmetry	Mode Description
—	355 (345)	—	—	Pt-C stretch
490 (415)	—	483	A_u	C-H out-of-plane ring bend
—	760 (—)	702	Bg	C-H out-of-plane ring bend
805 (645)	860 (665)	798	A_u	C-H out-of-plane ring bend
1050 (845)	1040 (865)	1041	A_u	CH_3 rock
1110 (845)	—	1100	Bu	C-H in-plane ring bend
—	1365 (1050)	1379	Bu	CH_3 deform (sym.)
1450 (1050)	1445 (1050)	1456	A_u	CH_3 deform (antisym.)
(1050) 1510	—	1485	Bu	CH_3 deform (anitsym.)
(1450)		1529	B_u	C-C, C-H ring stretch
2945 (2115)	2915 (2100)	2929	Bu	CH_3 stretches
		2975	A_u	
3030 (2260)	3010 (2230)	3064	B_u	C-H aromatic stretches
		3074	B_u	

Table 2

Multilayer o-Xylene on Pt(111) (cm^{-1})	Monolayer o-Xylene on Pt(111) (cm^{-1})	Infrared Liquid Phase o-Xylene (cm^{-1})	Symmetry	Mode Description
280 (240)	—	250	B_2	C-H o.o.p. ring bend
—	395 (345)	—	—	Pt-C stretch
465 (405)	—	436	B_2	C-H o. o. p. ring bend
—	705 (—)	?	—	—
775 (585)	845 (645)	729	B_2	C-H o. o.p.* ring bend
(785) 1050	1030 (845)	1022	B_2	CH_3 rock
(830)		1060	A_1	C-H in-plane ring bend
1210 (—)	—	1221	A_1	C-C stretch
1330 (—)	—	1300	A_1	C-H in-plane ring bend
—	1410 (1050)	1380	B_2	CH_3 deform (sym.)
(1065) 1480	1470 (1050)	1460	A_1	CH_3 deform (anitsym.)
(1420)	—	1500	A_1	C-C, C-H ring stretch
(2135) 3005	2905 (2180)	2971,2882	B_1, A_1	CH_3 stretch
(2280)	3025 (2260)	3040	B_1	C-H aromatic stretch

* out-of-plane

Table 3

p-Xylene on Pt(111) annealed to 370K (cm^{-1})	Infrared Liquid Phase p-Xylene (cm^{-1})	Mode Description
405 (405)	----	Pt-C stretch
635 (530)	483	C-H out-of-plane bend
755 (---)*	702	C-H out-of-plane bend
875 (675)	798	C-H out-of-plane bend
1055 (815)	1041	CH_2 wag or CH_3 rock
(1050) 1440	1456	CH_2 scissors or CH_3 deformation
(1340)	1529	C-C, C-H ring stretch and deformation
(2130) 2990	2929, 2975	CH_2 or CH_3 stretch
(2190)	3064	C-H aromatic stretch

* This mode is masked masked by the 675 cm^{-1} loss in the deuterated p-xylene spectrum.

Table 4

p-Xylene on Pt(111) annealed to 550K (cm^{-1})	Mode Description
800	C-H fragment bend
1300	C-C stretch of C_2H
3100	C-H fragment stretch

Table 5

o-Xylene on Pt(111) annealed to 370K (cm^{-1})	Infrared Liquid Phase o-Xylene (cm^{-1})	Mode Description
390 (380)	---	Pt-C stretch
605 (490)	436	C-H out-of-plane ring bend
755 (---)	694	C-H out-of-plane ring bend
855 (605)	729	C-H out-of-plane ring bend
1040 (805)	---	CH_2 wag
1150 (---)	1120	C-H in-plane bend
1380 (1250)	1450	C-C, C-H in-plane ring stretch and deformation
1450 (1340)	1500	C-C, C-H in-plane ring stretch and deformation
2950 (2135)	----	CH_2 stretch
3035 (2220)	3040	C-H aromatic stretch

Table 6

o-Xylene on Pt(111) annealed to 470K (cm^{-1})	Infrared Liquid Phase o-Xylene (cm^{-1})	Mode Description
450 (425)	---	Pt-C stretch
620 (605)	---	Pt-C stretch
760 (605)	729	C-H out-of-plane ring bend
870 (870)	830	C-C in-plane ring breathing
1010 (1000)	---	?
1235 (1170)	1221	C-C stretch
1535 (1340)	1500	C-C, C-H ring stretch
3090 (2295)	3071	C-H aromatic stretch

Table 7

o-Xylene on Pt(111) annealed to 640K (cm^{-1})	Mode Description
400	Pt-C stretch
800	C-H fragment bend
3100	C-H fragment stretch

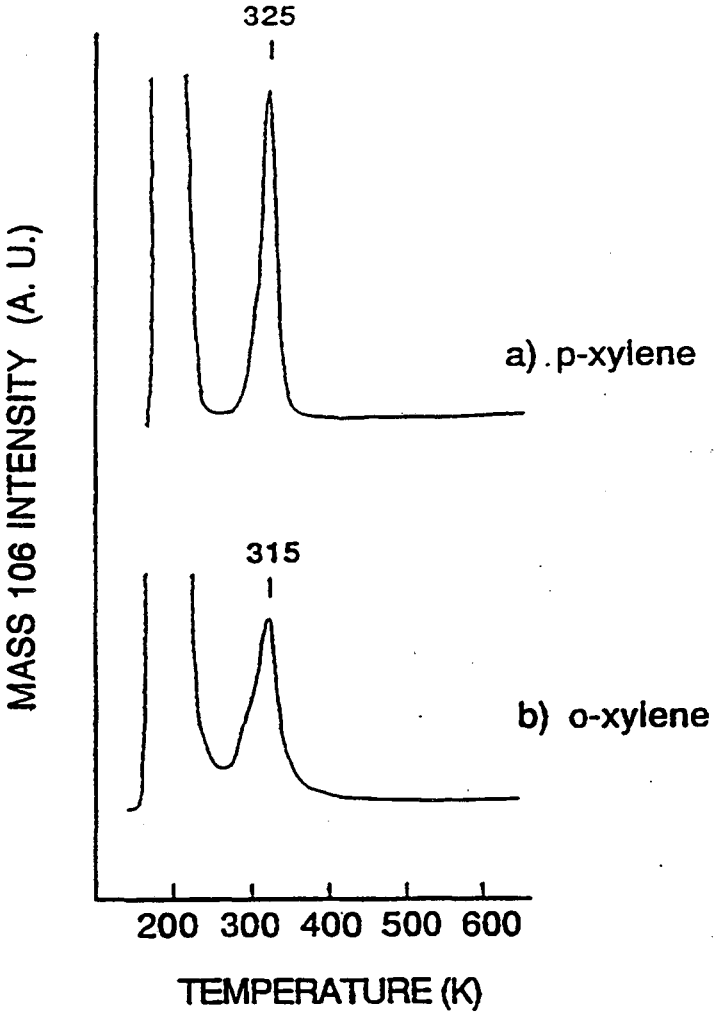
325
315
MASS 106 INTENSITY (A. U.)
a) p-xylene
b) o-xylene
200 300 400 500 600
TEMPERATURE (K)

Fig. 1

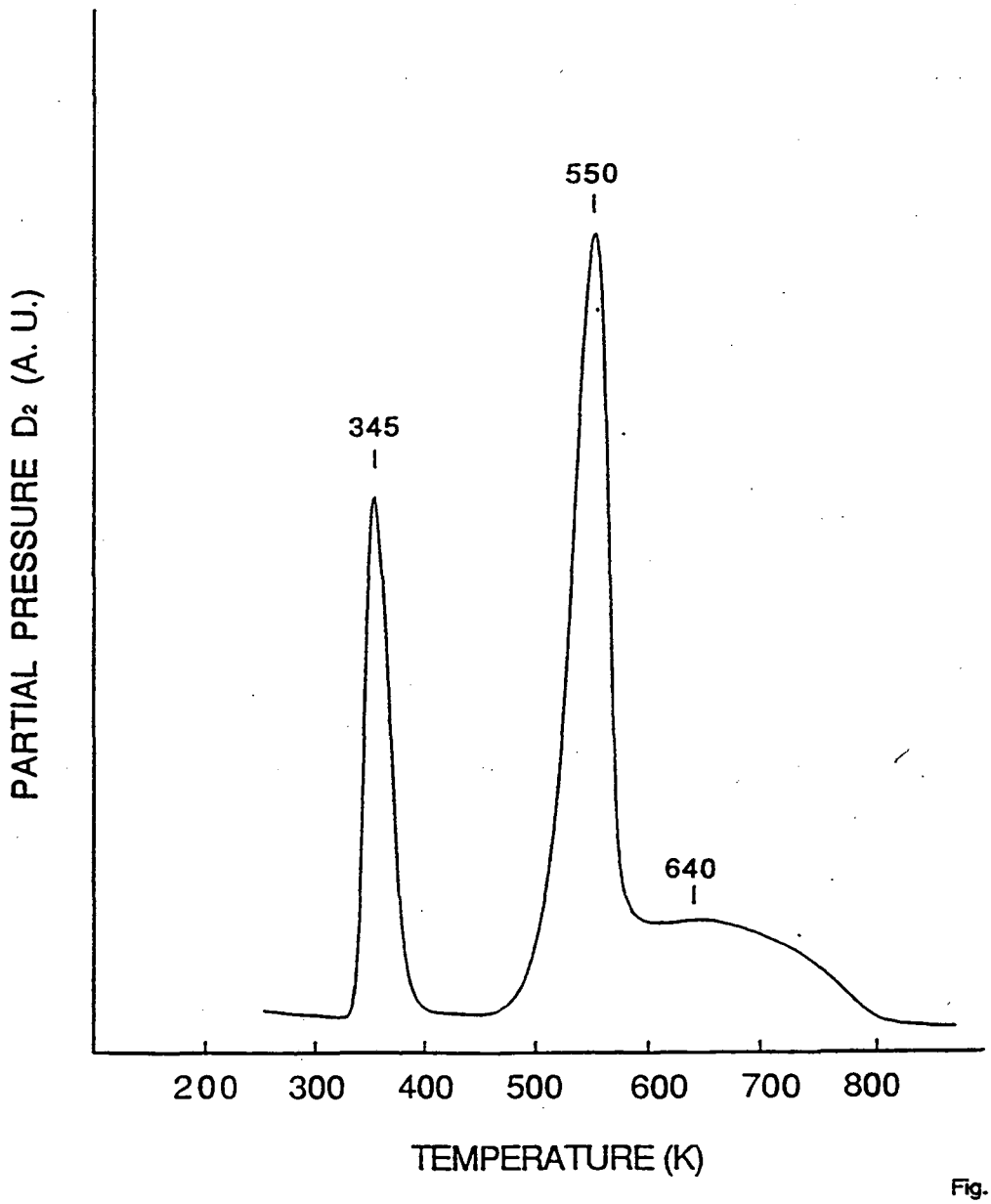
PARTIAL PRESSURE D2 (A. U.)
550
345
640
200
300
400
500
600
700
800
TEMPERATURE (K)

Fig. 2

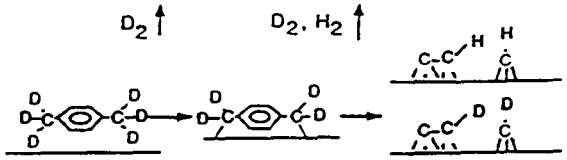
D2
D2, H2

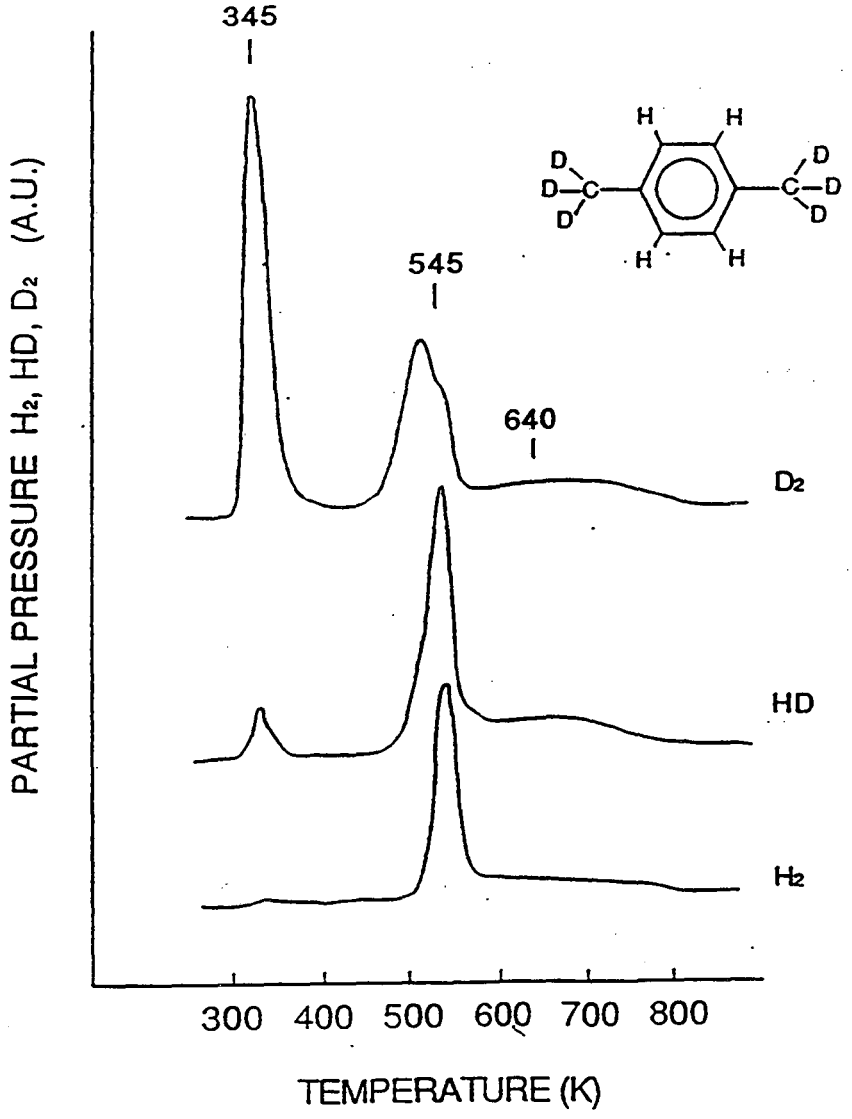
345
545
640
D2
HD
H2
PARTIAL PRESSURE H2, HD, D2 (A.U.)
300 400 500 600 700 800
TEMPERATURE (K)

Fig. 3

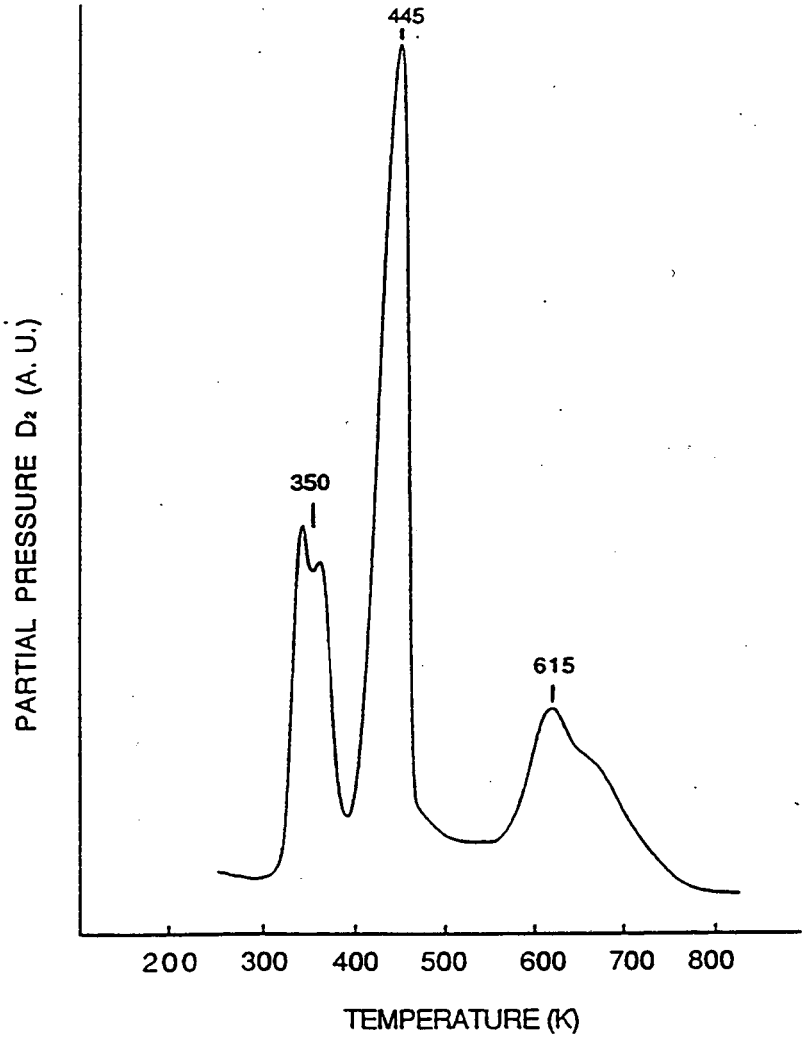
445
350
615
PARTIAL PRESSURE D₂ (A. U.)
200
300
400
500
600
700
800
TEMPERATURE (K)

Fig. 4

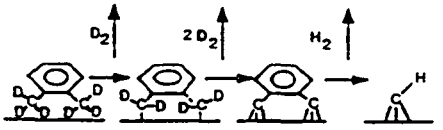
D2
2D2
H2

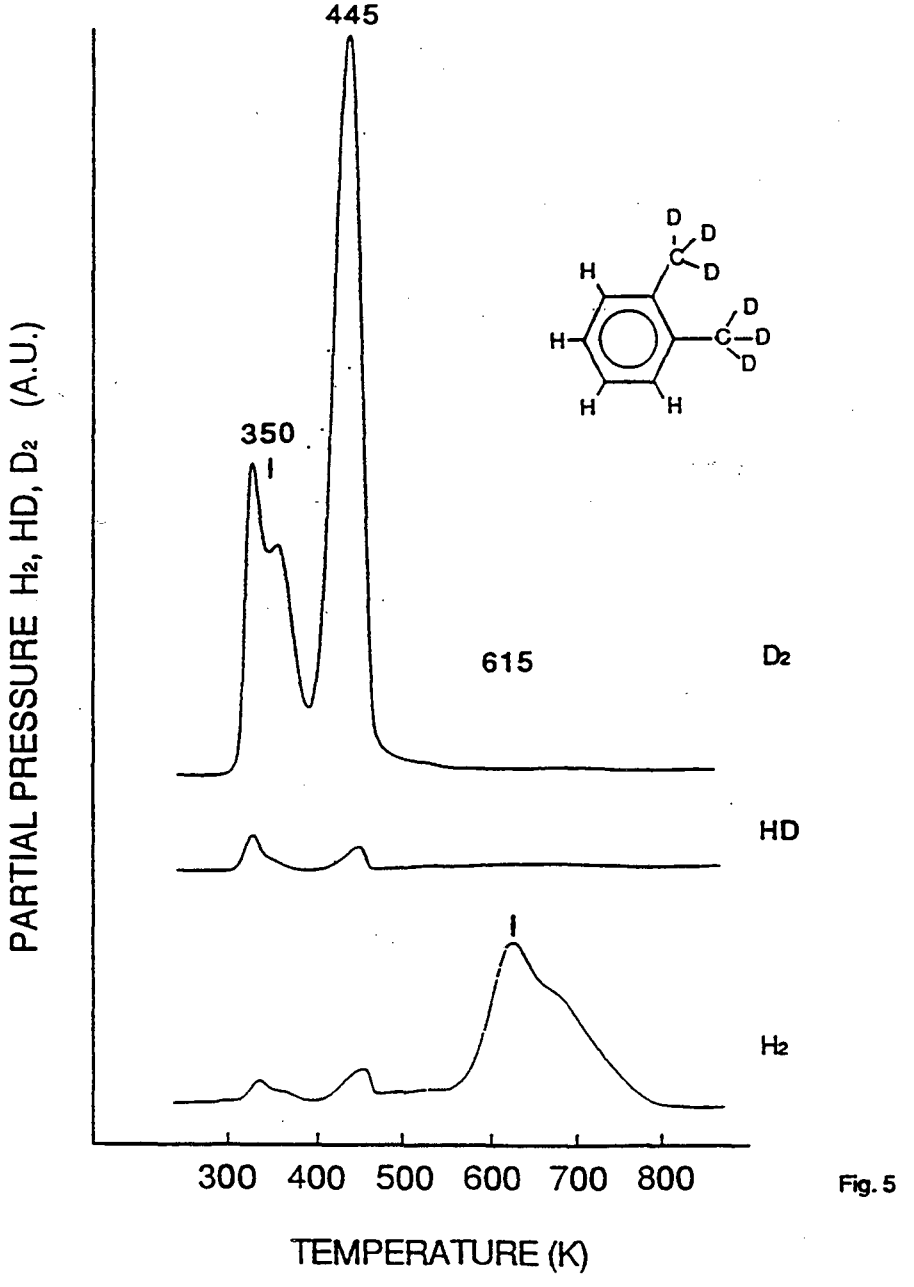
445
350
615
D2
HD
H2
PARTIAL PRESSURE H2, HD, D2 (A.U.)
300 400 500 600 700 800
TEMPERATURE (K)

Fig. 5

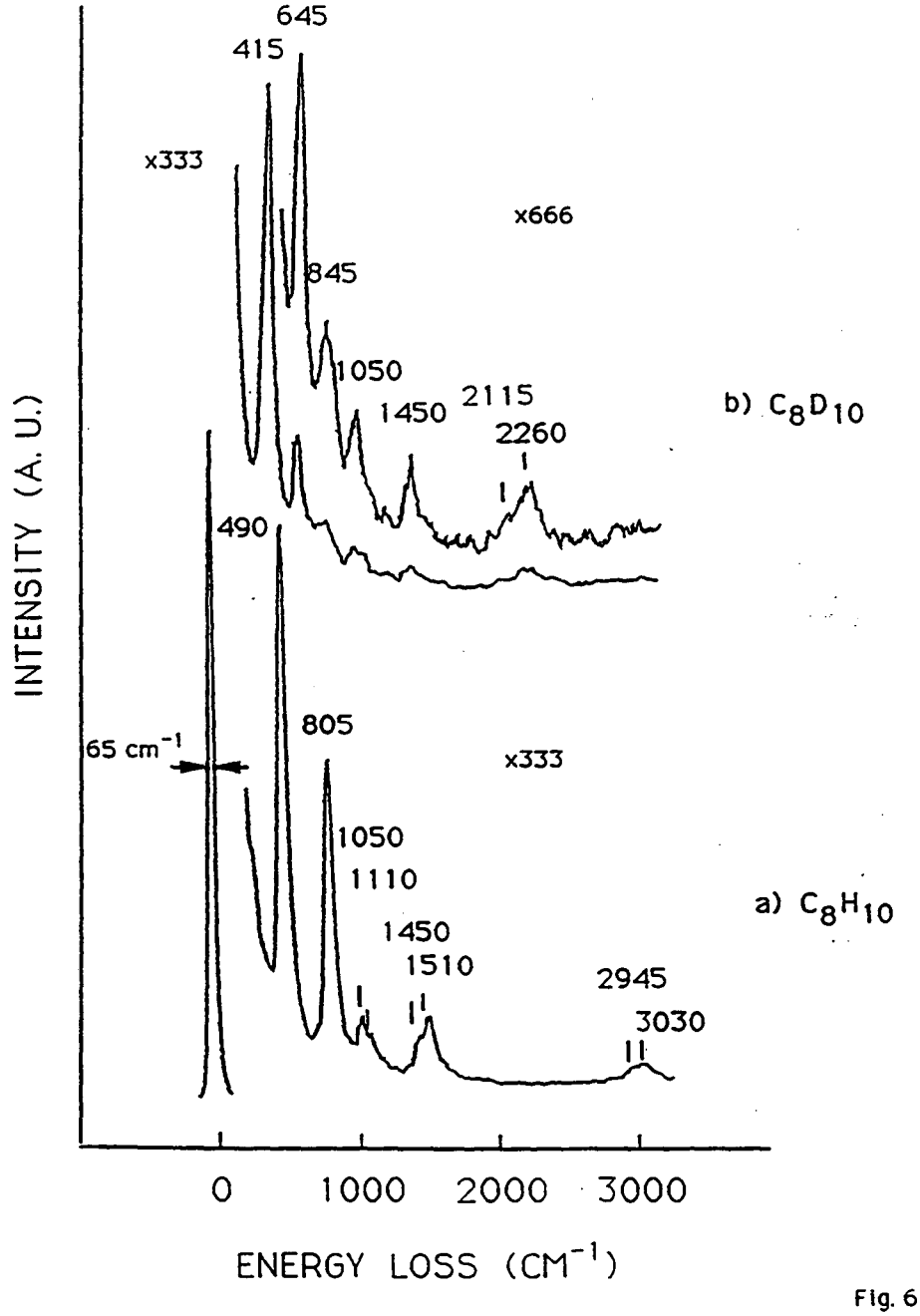
645
415
x333
x666
845
1050
1450
2115
2260
b) C_8D_10
490
805
65 cm^{-1}
x333
1050
1110
1450
1510
2945
3030
a) C_8H_10
INTENSITY (A.U.)
0
1000
2000
3000
ENERGY LOSS (CM^{-1})

Fig. 6

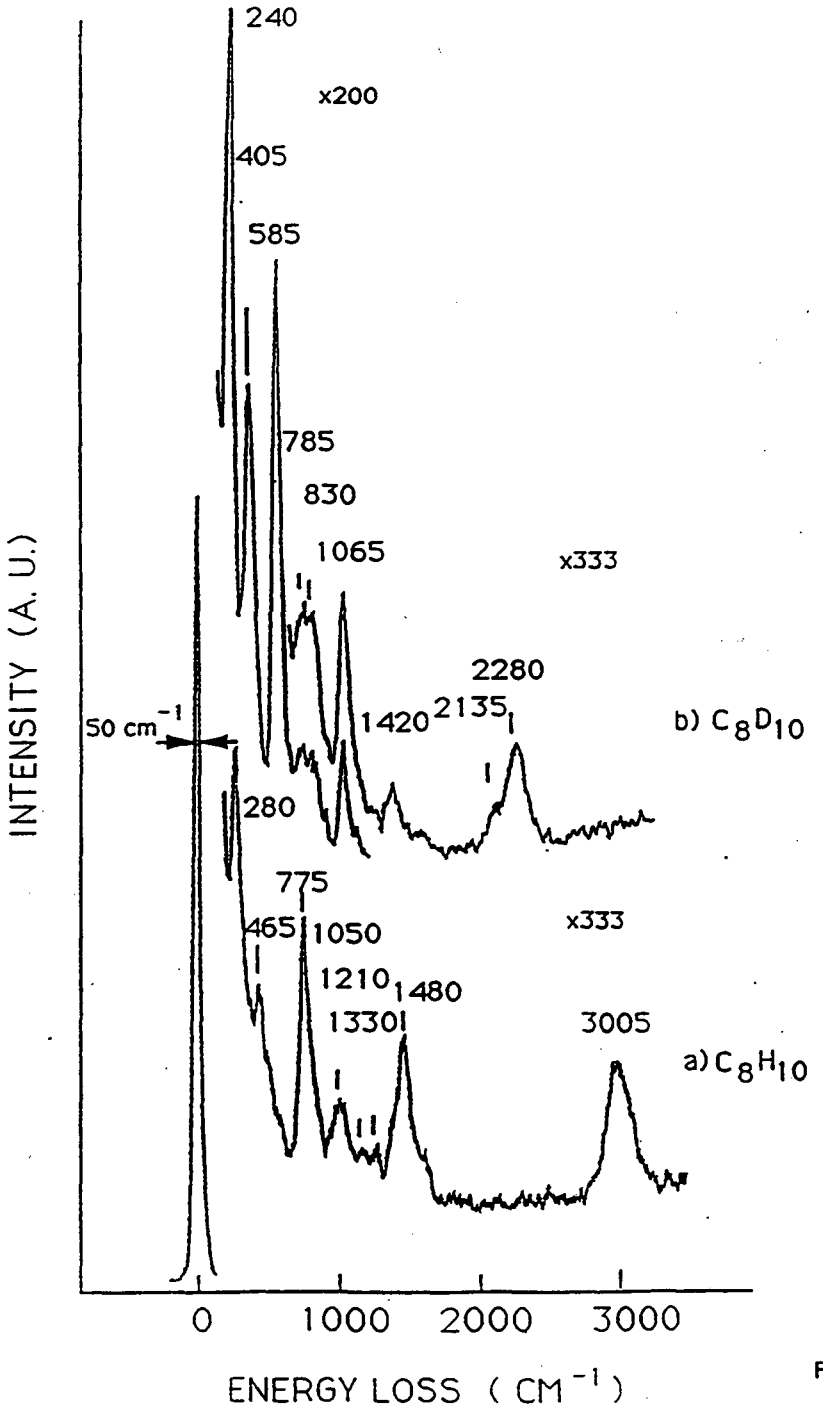
240
x200
405
585
785
830
1065
x333
2280
2135
1420
b) C_8D_{10}
50 cm^{-1}
280
775
465
1050
x333
1210
1480
1330
3005
a) C_8H_{10}
INTENSITY (A. U.)
0
1000
2000
3000
ENERGY LOSS (CM^{-1})

Fig. 7

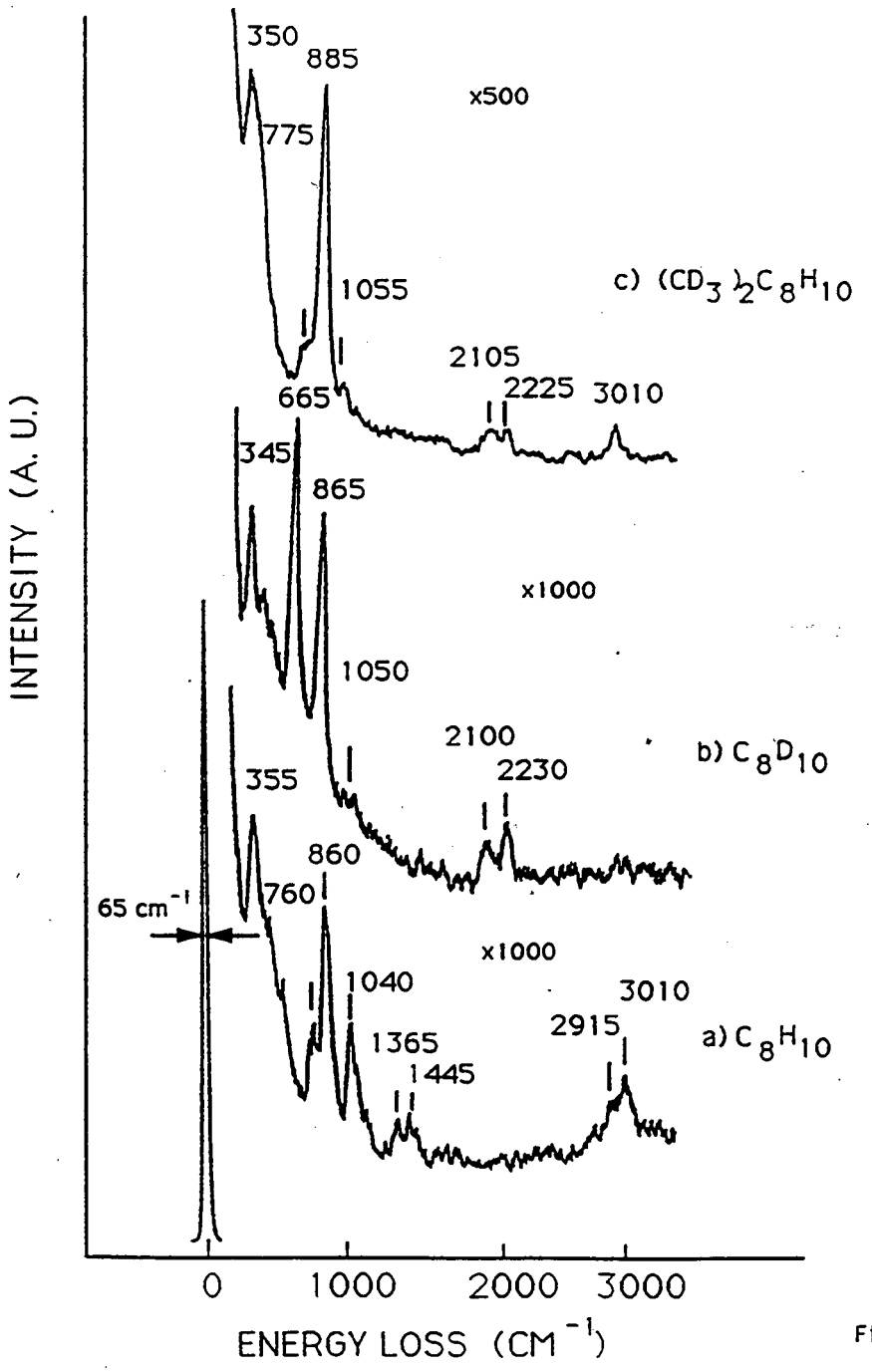
350
885
x500
775
1055
c) $(CD_3)_2C_8H_{10}$
2105
2225
3010
665
345
865
x1000
1050
2100
2230
b) C_8D_{10}
355
860
760
65 cm^{-1}
x1000
1040
3010
2915
a) C_8H_{10}
1365
1445
INTENSITY (A. U.)
0
1000
2000
3000
ENERGY LOSS (CM^{-1})

Fig. 8

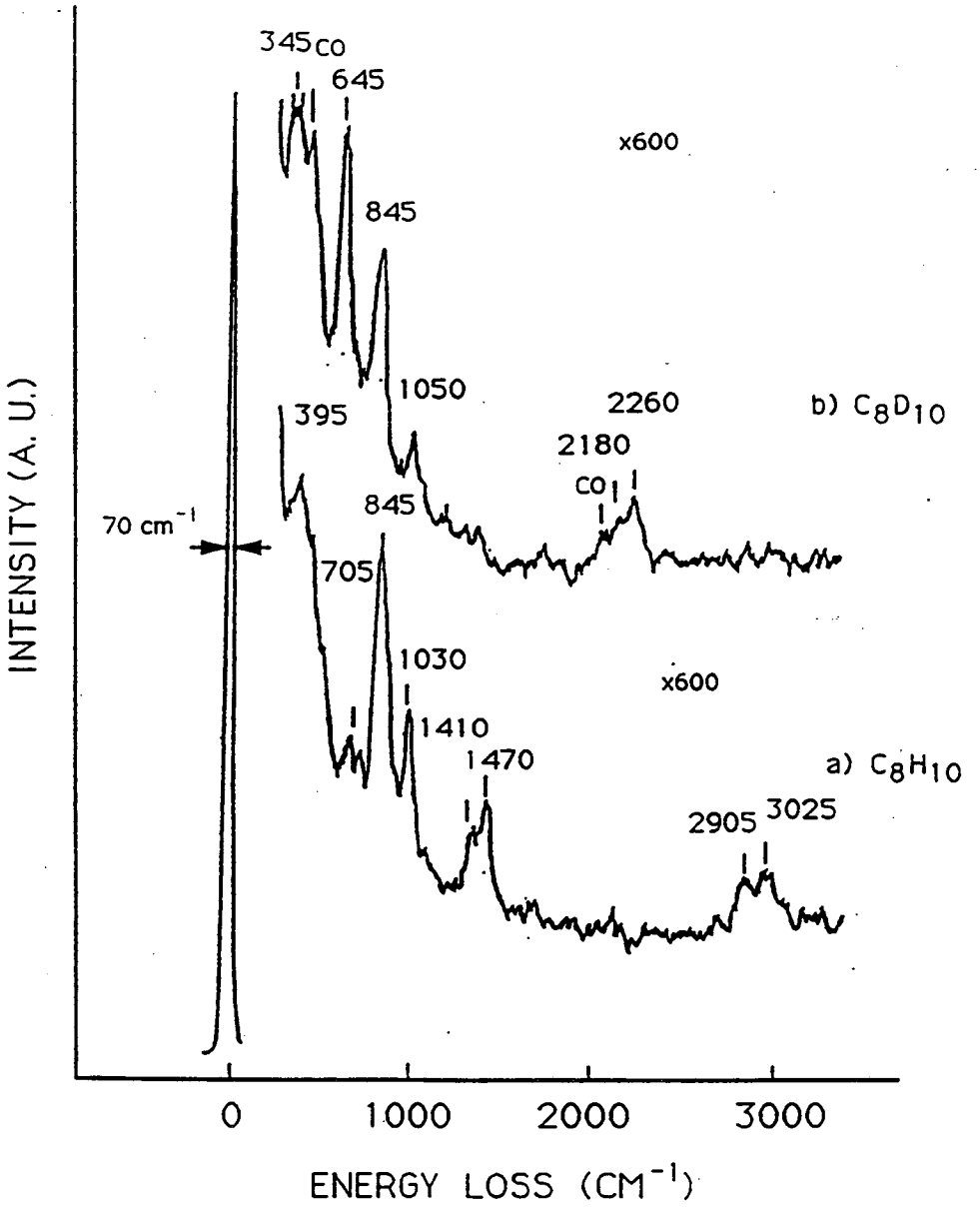
345 CO
645
x600
845
1050
395
2260
b) C_8D_{10}
2180
CO
845
70 cm^{-1}
705
1030
x600
1410
1470
a) C_8H_{10}
2905
3025
INTENSITY (A. U.)
0
1000
2000
3000
ENERGY LOSS (CM^{-1})

Fig. 9

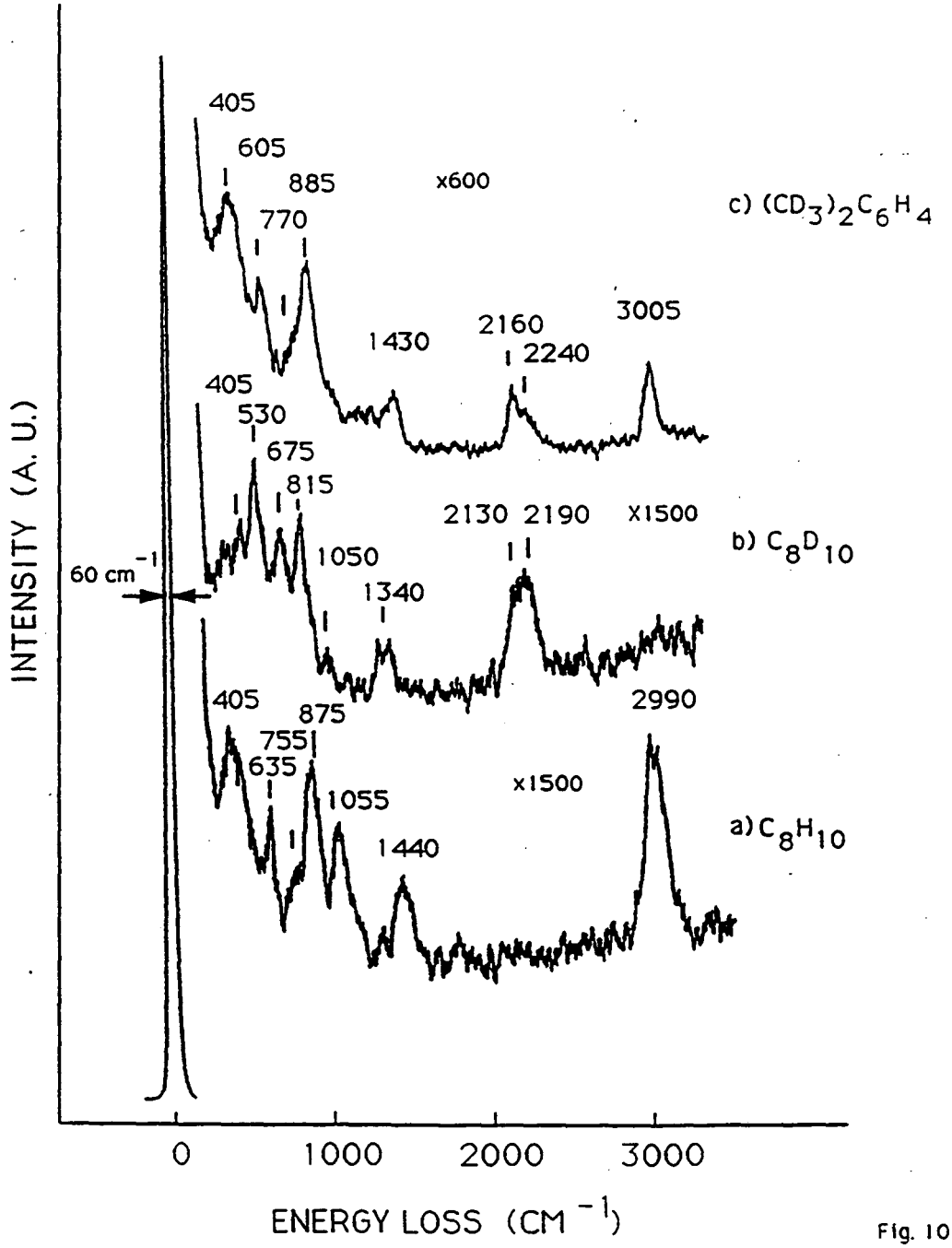
405
605
885
x600
770
c) $(CD_3)_2C_6H_4$
1430
2160
2240
3005
405
530
675
815
2130 2190
x1500
b) C_8D_{10}
60 cm^{-1}
1050
1340
405
875
2990
755
635
x1500
1055
a) C_8H_{10}
1440
INTENSITY (A.U.)
0
1000
2000
3000
ENERGY LOSS (CM^{-1})

Fig. 10

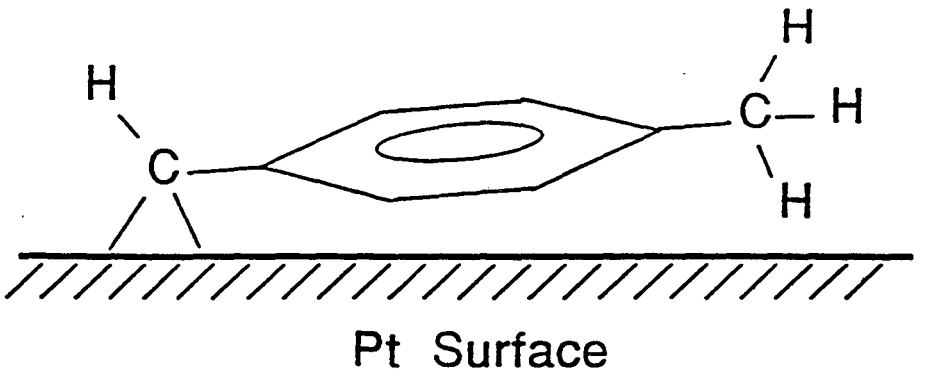

Fig. 11a

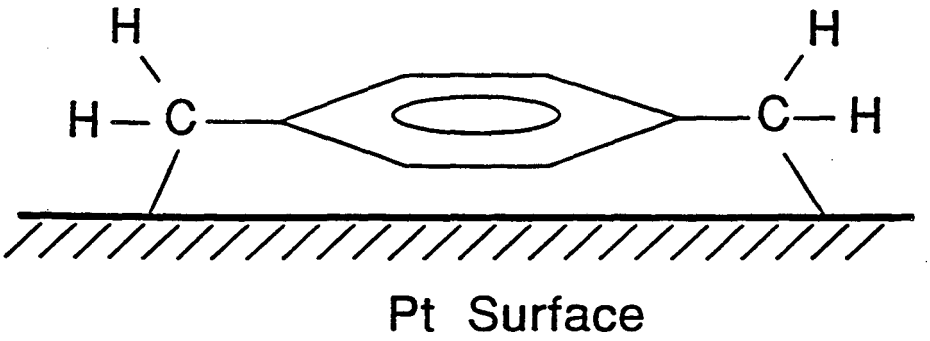

Fig 11b

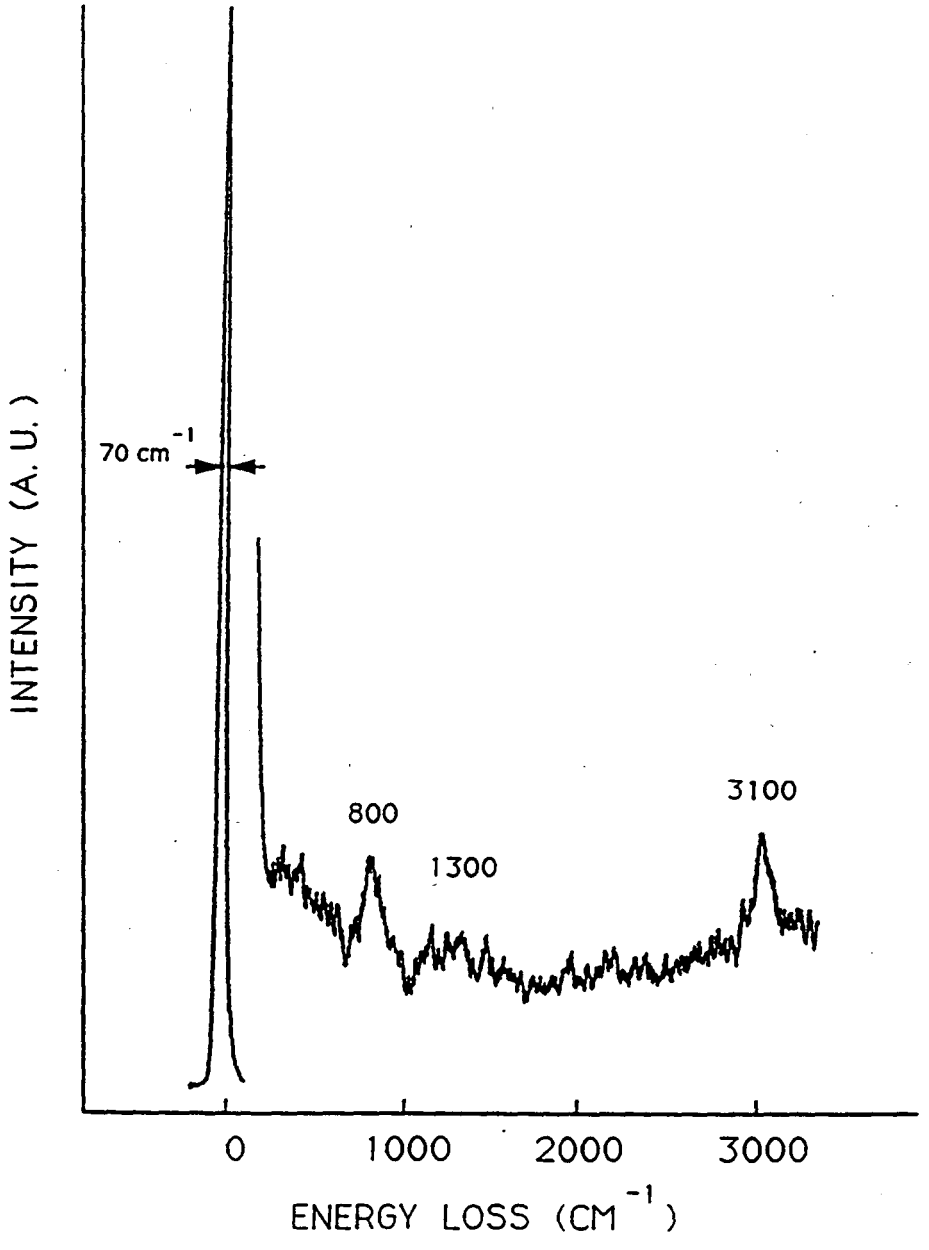
INTENSITY (A. U.)
70 cm^{-1}
800
1300
3100
0
1000
2000
3000
ENERGY LOSS (CM^{-1})

Fig. 12

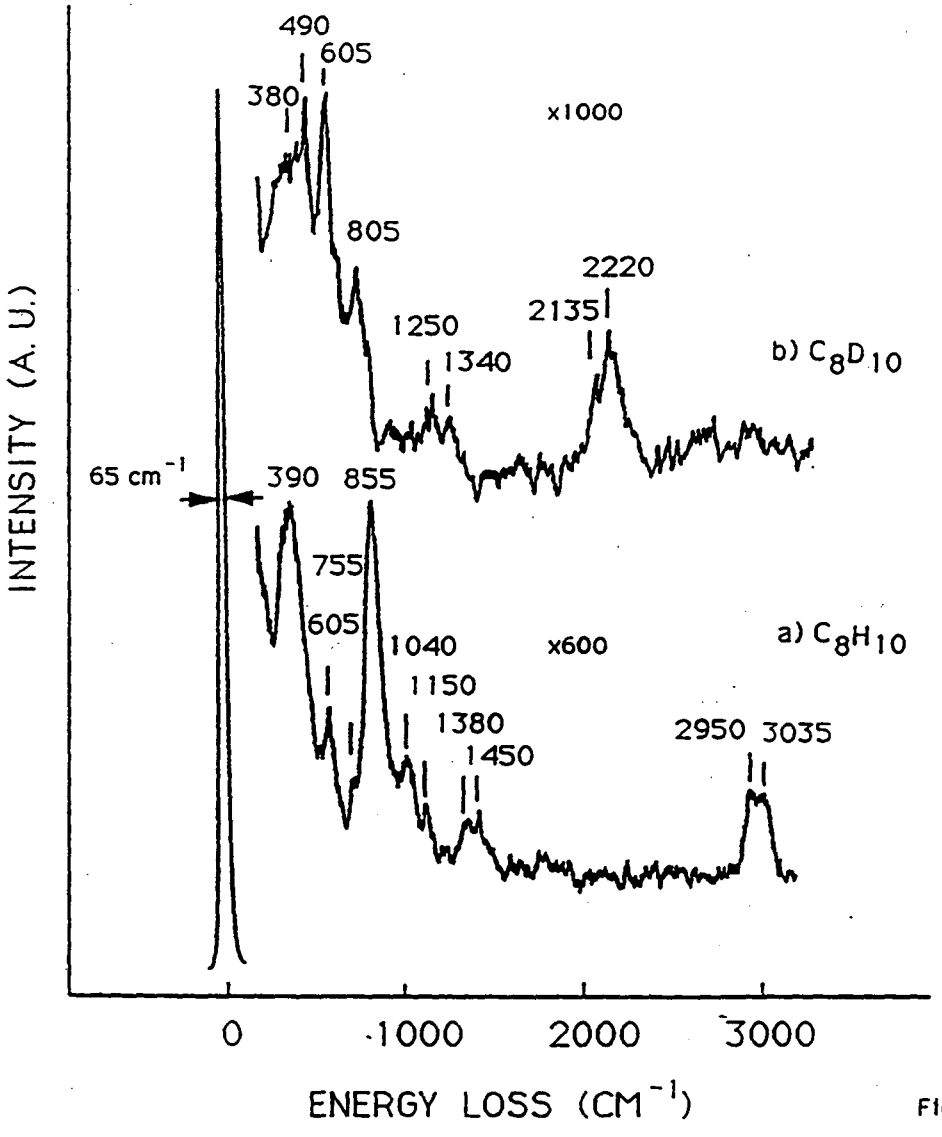
490
605
380
x1000
805
2220
2135
1250
1340
b) C_8D_{10}
65 cm^{-1}
390
855
755
605
1040
x600
a) C_8H_{10}
1150
1380
1450
2950
3035
INTENSITY (A. U.)
0
1000
2000
3000
ENERGY LOSS (CM^{-1})

Fig. 13

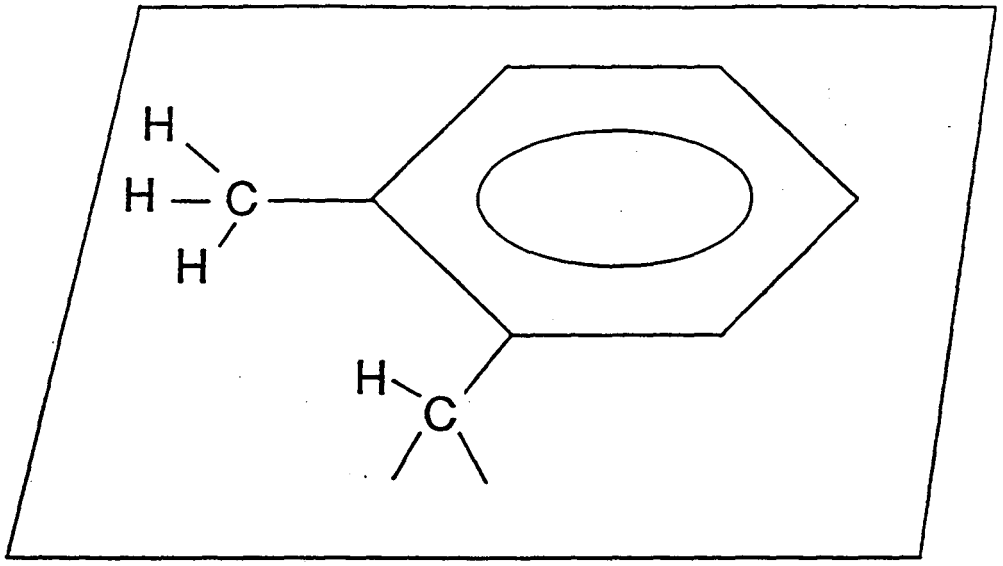

Fig. 14a

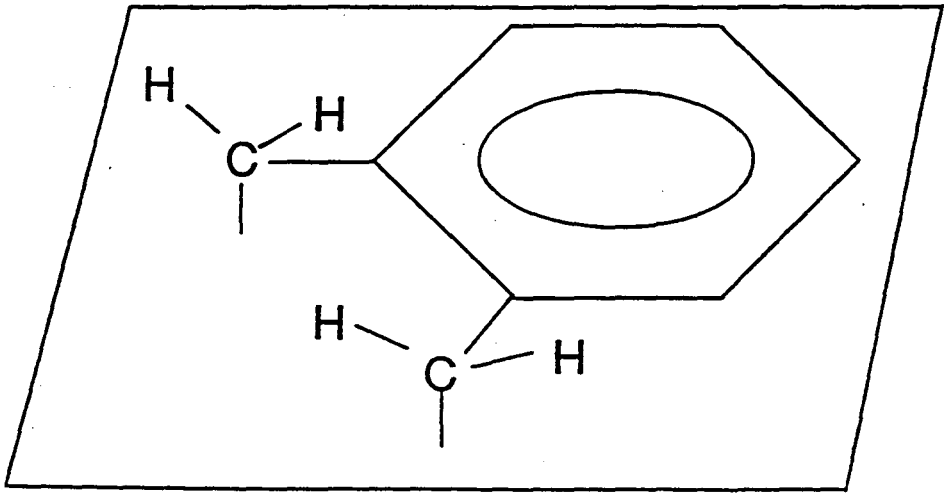

Fig 14b

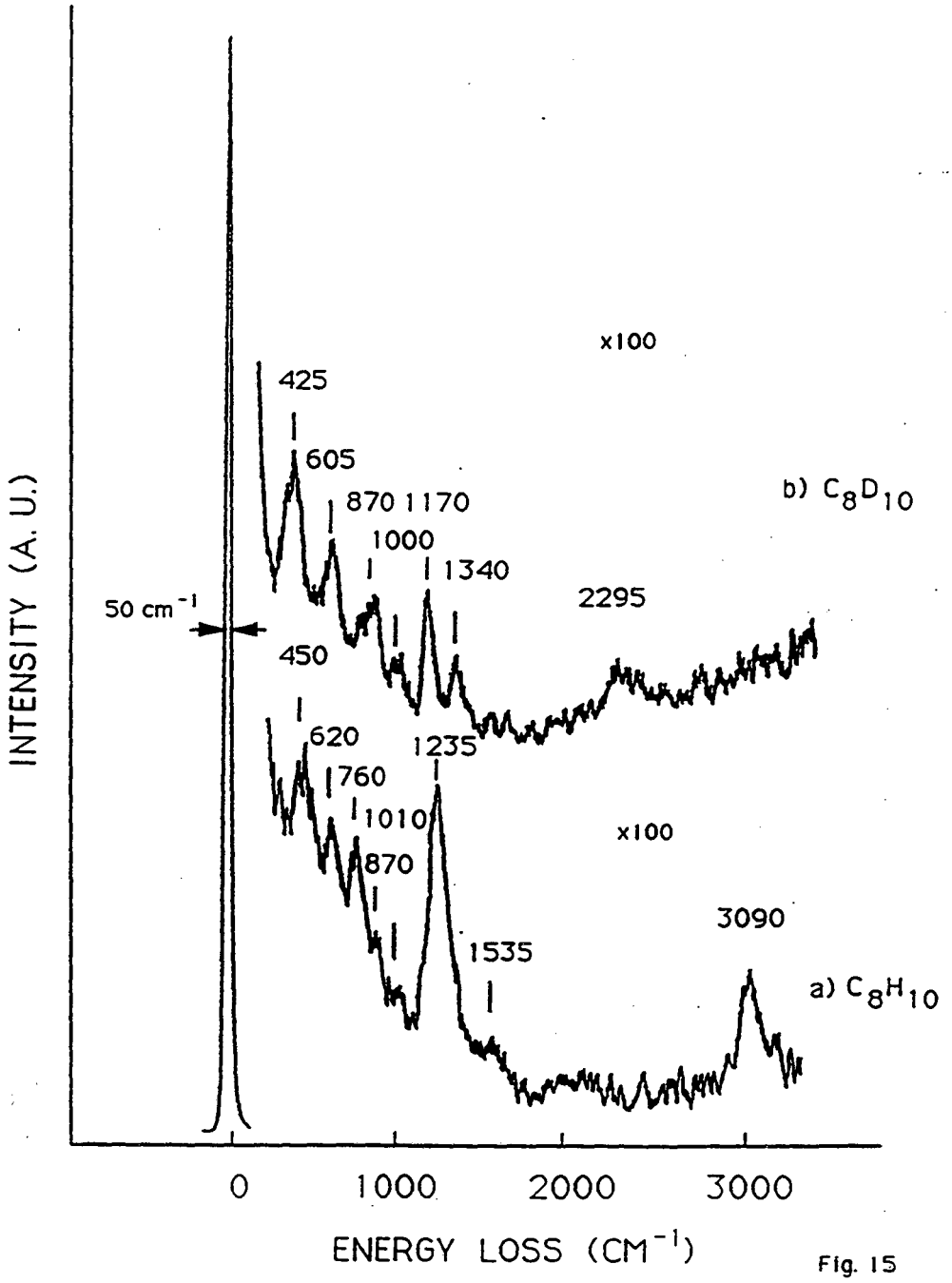
INTENSITY (A.U.)
50 cm⁻¹
x100
425
605
870
1170
1000
1340
2295
b) C8D10
450
620
760
1010
870
1235
x100
3090
1535
a) C8H10
0
1000
2000
3000
ENERGY LOSS (CM⁻¹)

Fig. 15

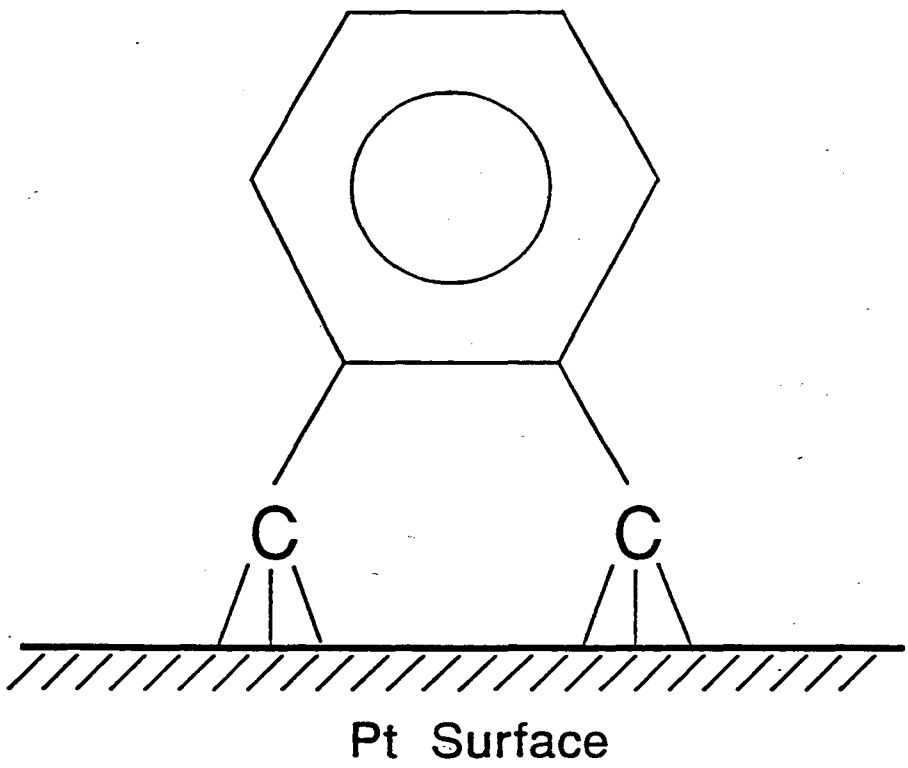

Fig. 16

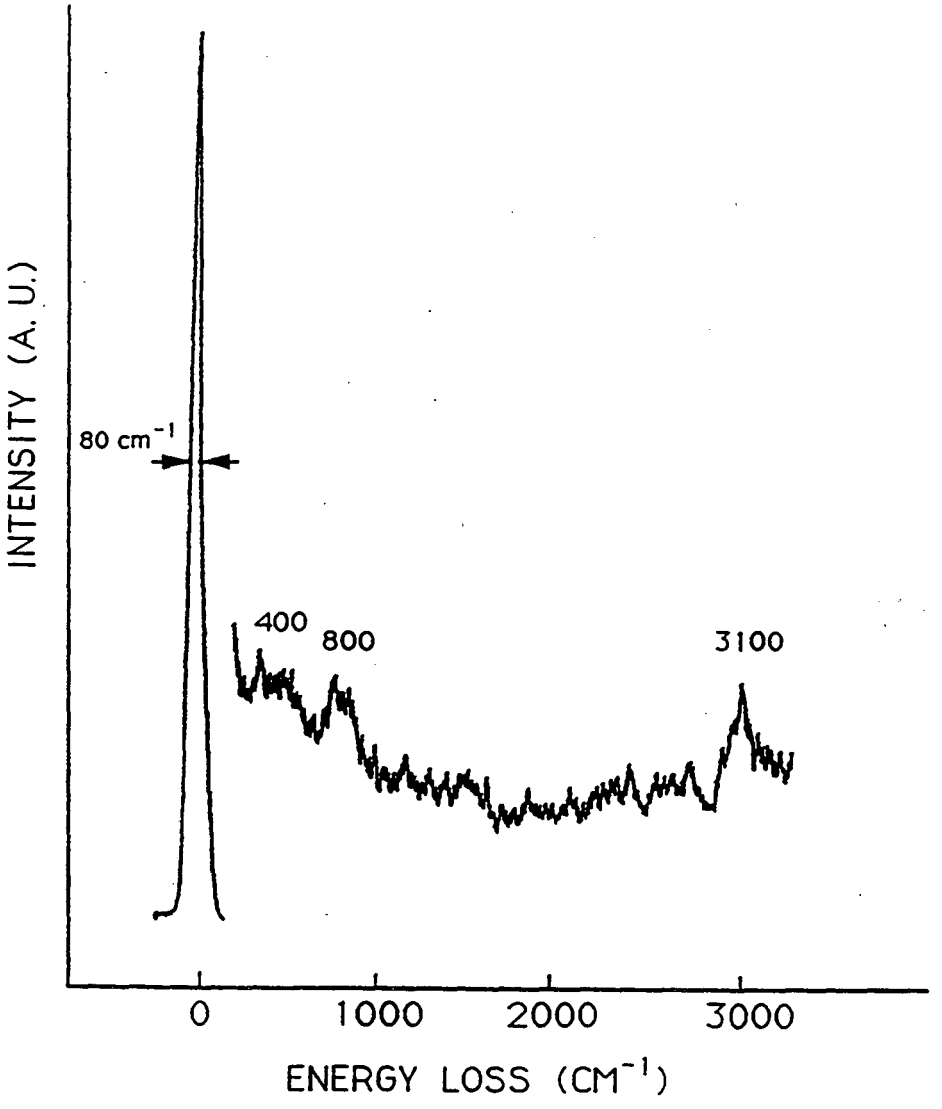
INTENSITY (A. U.)
80 cm⁻¹
400
800
3100
0
1000
2000
3000
ENERGY LOSS (CM⁻¹)

Fig. 17

LAWRENCE BERKELEY LABORATORY
UNIVERSITY OF CALIFORNIA
TECHNICAL INFORMATION DEPARTMENT
BERKELEY, CALIFORNIA 94720